

# Molecular structure of hybrid aligned nematic slit-pores

vorgelegt von

Diplom-Chemiker

**Manuel Greschek**

aus Kassel

Von der Fakultät II - Mathematik und Naturwissenschaften

der Technischen Universität Berlin

zur Erlangung des akademischen Grades

Doktor der Naturwissenschaften

- Dr. rer. nat. -

genehmigte Dissertation

Promotionsausschuss:

Vorsitzender: Prof. Dr. Martin Oestreich

Berichter: Prof. Dr. Martin Schoen

Berichter: Prof. Dr. Keith Gubbins

Tag der wissenschaftlichen Aussprache: 25.01.2012

Berlin 2012

**D 83**



# Zusammenfassung

In dieser Arbeit verwenden wir Monte Carlo Simulationen, um die molekulare Struktur eines Flüssigkristalls in einer Nanopore zu untersuchen. Wir führen die Simulationen in einem erweiterten isobaren Ensemble aus, in dem der thermodynamische Gleichgewichtszustand durch die natürlichen Variablen Temperatur  $T$ , Teilchenzahl  $N$ , Substratabstand  $s_z$  und Lateraldruck  $\tau_{\parallel}$  bestimmt ist. Wir variieren unter isothermen Bedingungen  $\tau_{\parallel}$  und untersuchen den Einfluss von diversen Ankerszenarien auf den isotrop-nematischen (IN) Phasenübergang. Die Wechselwirkung zwischen zwei flüssigkristallinen Teilchen wird durch das Hess-Su Potential beschrieben, welches einem Lennard-Jones (12-6) Potential mit orientierungsabhängigem attraktiven Anteil entspricht. In den Simulationen werden die Festkörpergrenzflächen als planparallele, unstrukturierte Substrate implementiert. Dadurch ist die Fluid-Substrat Wechselwirkung bei fester molekularer Orientierung nur eine Funktion des Abstands zwischen dem Massenschwerpunkt der Teilchen und dem Substrat.

Zur Auflösung der molekularen Struktur verwenden wir Histogramme der lokalen Dichte und des lokalen nematischen Ordnungsparameters. Durch die räumliche Symmetriebrechung bilden sich zu den Wandebenen parallele Schichten. Unter *homogenen* Ankerbedingungen, d.h. an gegenüberliegende Substraten wird die gleiche Ankerfunktion verwendet, kann der IN Phasenübergang erheblich verschoben oder unterdrückt werden. Die Vorzugsrichtung der nematischen Phase entspricht der durch die Substrate bevorzugten Orientierung der Kontaktschicht. Bei planarer Verankerung kann eine der Nematisierung vorausgehende strukturelle Transformation beobachtet werden, die zu der Bildung einer zusätzlichen Schicht führt.

In *heterogenen (hybriden)* Poren sind an den gegenüberliegenden Substraten unterschiedliche Orientierungen bevorzugt. Der IN Phasenübergang ist unter diesen Bedingungen unabhängig von dem konkreten Ankerszenario, da die nematische Vorzugsorientierung als eine Superposition der an den Substraten bevorzugten Orientierungen aufgefasst werden kann. Dem IN Phasenübergang geht eine Sekundärumwandlung voraus, bei der sich die Teilchen nahe der Porenmitte entlang einer Vorzugsorientierung ausrichten, deren Richtung von dem konkreten Ankerszenario abhängig ist.

Durch eine Finite-Size Analyse und Anwendung der Kumulantenschnittpunktmethode können wir zeigen, dass der IN Phasenübergang schwach *erster* Ordnung ist. Zusätzlich untersuchen wir unsere Daten mit Landau's Theorie der Phasentransformation.



# Abstract

In this work we employ Monte Carlo simulations to investigate the molecular structure of a model liquid crystal confined to a nanoscopic slit-pore. The simulations are carried out in a specialised isostress ensemble in which the thermodynamic equilibrium is determined by the set of natural variables, i.e. temperature  $T$ , number of particles  $N$ , wall separation  $s_z$  and the lateral stress  $\tau_{\parallel}$ . Under isothermal conditions we investigate the impact of various anchoring scenarios on the isotropic-nematic (IN) transition driven by  $\tau_{\parallel}$ . The fluid-fluid interaction is described by the Hess-Su potential, a Lennard-Jones(12-6) potential with an orientation-dependent attractive term. The confining surfaces are implemented as plane, parallel and structureless solid substrates such that at fixed molecular orientation the fluid-substrate contribution depends only on the distance between the centre-of-mass of each mesogen and the substrate.

The molecular structure of the confined mesogen is analysed in terms of histograms representing the local density and the local nematic order parameter. Because of the symmetry breaking presence of the substrates the centre-of-mass positions of the mesogen may be organised in layers parallel to the wall plane. Under *homogeneous* anchoring conditions, in which opposing walls favour the same anchoring direction, the IN transition may be shifted considerably or suppressed. The director in the nematic phase coincides with the anchoring direction of the contact layer enforced by the substrates. For planar anchoring a structural transformation prior to the onset of nematisation is observed which results in the formation of an additional layer.

In *heterogeneous (hybrid)* anchoring scenarios, where we impose different anchoring functions at opposing walls, the IN transition is nearly independent of the specific anchoring scenario. This is because the nematic director assumes a direction that is a compromise between the directions enforced by the competing anchoring functions. A secondary transformation occurs at lower compressional stresses preceding that of the IN transition. The particles close to the slit-pore's mid-plane prealign in specific directions that depend on the details of the anchoring scenario.

We perform a finite-size scaling analysis to investigate the nature of the bulk IN transition. We employ the cumulant intersection method to show that it is a weak *first-order* transition. In addition, we analyse our data in terms of Landau's theory of phase transitions.



## List of Publications

### Contributing Publications:

- [1] M. Greschek, M. Melle, M. Schoen *Isotropic-nematic phase transitions in confined mesogenic fluids. The role of substrate anchoring.* Soft Matter **6**: 1898 (2010)
- [2] M. Greschek, M. Schoen *Frustration of nanoconfined liquid crystals due to hybrid substrate anchoring.* Soft Matter **6**: 4931 (2010)
- [3] M. Greschek, M. Schoen *Finite-size scaling analysis of isotropic-nematic phase transitions in an anisometric Lennard-Jones fluid.* Phys. Rev. E **83**: 011704 (2011)

### Non-contributing Publications:

- [4] M. G. Mazza, M. Greschek, R. Valiullin, J. Kärger, M. Schoen *Entropy-driven enhanced self-diffusion in confined reentrant supernematics.* Phys. Rev. Lett. **105**: 227802 (2010)
- [5] M. G. Mazza, M. Greschek, R. Valiullin, M. Schoen *Role of stringlike, supramolecular assemblies in reentrant supernematic liquid crystals.* Phys. Rev. E **83**: 051704 (2011)
- [6] M. Greschek, M. Schoen *Orientational prewetting of planar solid substrates by a model liquid crystal.* J. Chem. Phys. **135**: 204702 (2011)



# Contents

<b>1</b>	<b>Introduction</b>	<b>1</b>
1.1	Mesophases . . . . .	1
1.1.1	Theory of the Nematic State . . . . .	2
1.1.2	Influence of Substrates . . . . .	4
1.1.3	Applications of Confined Liquid Crystals . . . . .	8
<b>2</b>	<b>Theoretical Background</b>	<b>11</b>
2.1	Thermodynamic Potential . . . . .	11
2.2	The Molecular Description . . . . .	14
2.2.1	The Partition Function . . . . .	15
2.2.2	Response Functions . . . . .	18
2.3	Phase Transitions . . . . .	20
2.3.1	Classification of Phase Transitions . . . . .	20
2.3.2	Order Parameters and Phase Transitions . . . . .	21
2.4	Landau Theory . . . . .	26
2.4.1	Basic Concepts . . . . .	26
2.4.2	Macroscopic Nematic Order Parameter . . . . .	30
2.4.3	Landau-De Gennes Theory . . . . .	34
<b>3</b>	<b>Model and Methods</b>	<b>39</b>
3.1	Monte Carlo Simulations . . . . .	39
3.1.1	Metropolis Algorithm . . . . .	39
3.1.2	Isostress-Isostrain Monte Carlo . . . . .	41
3.2	Microscopic Order Parameter . . . . .	44

3.3	Finite-Size Scaling . . . . .	46
3.3.1	Critical Exponents and Scaling Functions . . . . .	47
3.3.2	Cumulants . . . . .	48
<b>4</b>	<b>Results</b>	<b>51</b>
4.1	Finite-Size Scaling . . . . .	51
4.1.1	Finite-size scaling analysis of isotropic-nematic phase transitions in an anisometric Lennard-Jones fluid . . . . .	51
4.2	Homogeneous Slit-Pore . . . . .	64
4.2.1	Isotropic-nematic phase transitions in confined mesogenic fluids. The role of substrate anchoring . . . . .	64
4.3	Hybrid Slit-Pore . . . . .	77
4.3.1	Frustration of nanoconfined liquid crystals due to hybrid sub- strate anchoring . . . . .	77
<b>5</b>	<b>Conclusions &amp; Outlook</b>	<b>89</b>

# Introduction

## 1.1 Mesophases

Matter commonly exists in three states: *solid*, *liquid* and *gas*, but in anisotropic materials intermittent phases can be found. Take a perfectly ordered crystal where the constituent molecules are anisotropic. In this crystal long-range correlations of the centre-of-mass positions and the orientations exist. If the crystal is heated, positional and orientational order can disappear simultaneously to result in an isotropic liquid. If the molecules are mildly anisotropic the orientational order can be lost first the positional order is left intact. This new state is called a *plastic crystal* [1–3]. If, on the other hand, the positional order is lost in at least one spatial direction but the orientational order is maintained the new state is called a *liquid crystal*.

Liquid crystals were discovered by the Viennese chemist Reinitzer [4], who observed an unusual sequence of phase transitions in some organic compounds. The solid material first melted to a turbid liquid before the liquid became clear [3]. Reinitzer also observed unexpected colouring of the intermediate phases. His colleague Lehmann [5] then used a setup of crossed polariser and analyser to observe birefringency of these states. The intermediate phases combine the anisotropic properties of a crystalline structure with liquid behaviour, i.e. they flow. For this reason Lehmann suggested calling these phases liquid crystals. On account of their mesomorphic (intermediate) form these phases are also called *mesomorphic* phases or *mesophases*. If the transition to a mesophase is driven by the concentration of a substance in a solvent these liquid crystals are called *lyotropic*. In this work, I focus on *thermotropic* liquid crystals, where the transition to a mesomorphic state is due to a thermal process over a certain temperature range. For detailed information on mesomorphic structures see [2, 6–9].

Depending on the organic substance, there may be a whole series of transitions to mesomorphic states. After Friedel [10], the liquid-crystalline states of a thermotropic liquid crystal can be classified in three main types: *nematic*, *smectic* and *cholesteric*. Substances forming mesophases are called *mesogen*. If the mesophase is smectic, the substance is denoted as *smectogen* and if it is nematic as *nematogen*.

Nearly all thermotropic liquid crystals have in common that their building blocks are highly anisotropic organic molecules [6]. Thus, the nematic state is distinguished from the isotropic state in Fig. 1.1(a) by a spontaneous orientation of the molecules' long axes in a parallel fashion, as can be seen in Fig. 1.1(b). As a consequence, long-range orientational order exists in the nematic state. This spontaneous transformation from an isotropic to a nematic phase is called the isotropic-nematic (IN) transition. The spatial positions of the molecules in the nematic phase are only correlated over a short-range which gives this phase its liquid character. The particles' long axes are parallel to a common axis which is called the director  $\hat{\mathbf{n}}$  of the phase. The director is the axis of rotational symmetry and this is why the nematic phase is optically uniaxial and shows birefringent properties. In the smectic phase (Fig. 1.1(c)) the particles are not only preferentially oriented but also organised in individual layers. The positions are correlated along a one-dimensional density wave whereas due to weak interactions between the individual layers the smectic phase is liquid in two spatial directions (i.e. within each molecular layer). The in-plane arrangements are variable and lead to a variety of smectic phases [6, 11, 12]. The cholesteric phase consists of chiral molecules that form nematic layers whose in-plane directors are periodically twisted, i.e. a helical axis is superimposed normal to the nematic director, as can be seen in Fig. 1.1(d).

### 1.1.1 Theory of the Nematic State

Approximate theoretical descriptions of the nematic state can be developed and we outline two commonly employed approaches below.

#### *Onsager Theory*

In Onsager's approach, the constituent hard particles are assumed to have the shape of long rods and interact only via repulsive forces [13]. Spherocylinders, i.e. cylinders of length  $L$  that are capped by two hemispheres of diameter  $D$ , are one possible example for the shape of rods. Due to the exclusively repulsive interactions of the rods, the

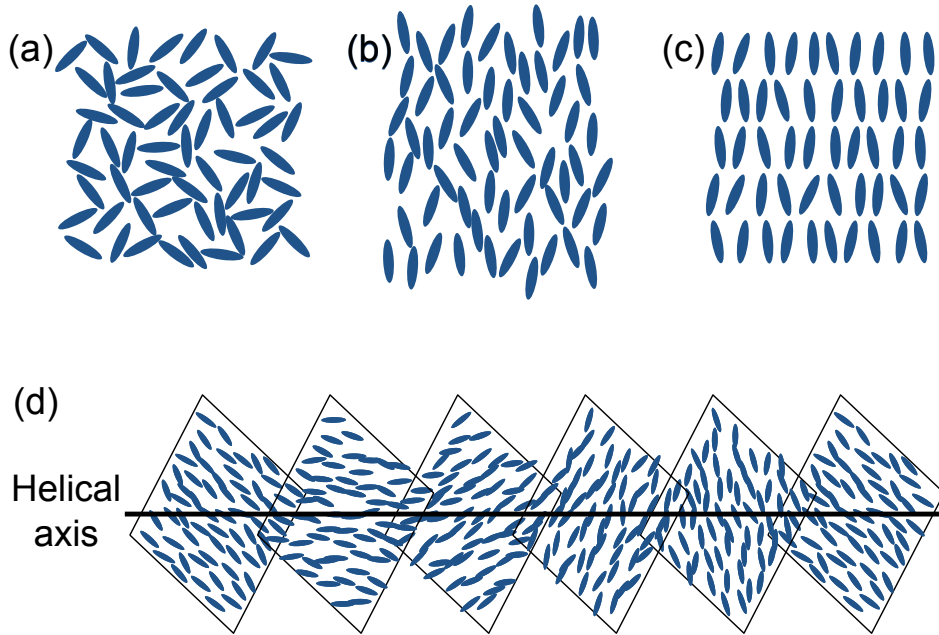


**Figure 1.1:** In part (a) the isotropic state is shown with randomly distributed orientations. After the transition to the nematic phase (b) the molecules' long axes are aligned along a nematic director. In the smectic phase (c) the molecules have additionally formed layers. In the cholesteric phase (d) in-plane directors are periodically twisted.

Onsager approach incorporates neither energetic effects nor temperature. The nematic state forms on account of steric effects while the density of the system increases. Therefore, this theory models a lyotropic liquid crystal. The transition from the isotropic to the nematic state in a lyotropic mesogen is driven by changes in the total entropy, to which translational and orientational entropy contribute. Compared with the isotropic state the orientational entropy of the nematic state is lower because the long axes are preferentially aligned with  $\hat{\mathbf{n}}$ . However, the translational entropy increases simultaneously because of the larger free volume accessible for translational motion. The gain in translational entropy exceeds the loss in orientational entropy such that the nematic state is stable if the density exceeds a certain threshold. Onsager then used a second order virial-expansion of the free energy to show that a *first-order* IN transition exists if the aspect ratio  $L/D$  of the rods exceeds unity considerably. More specifically, an exact solution for this model is solely possible in the limit  $L/D \rightarrow \infty$  but approximate results can be deduced for aspect ratios  $L/D > 40$ . The Onsager theory predicts a

density that is too low and a density jump that is too high at the transition and because of its ‘‘athermal’’ character it cannot describe the IN transition of thermotropic mesogens [6].

### *Maier-Saupe Theory*

In contrast to Onsager, Maier and Saupe assume that the anisotropic shape manifests itself in the attractive interactions. They therefore suggested [14, 15] that competition between the anisotropic attraction of the molecules and the change in orientational entropy affects the thermotropic IN transition. To model the attractive energy contribution they assumed that permanent dipole-dipole interactions can be neglected and only induced dipole-dipole interactions need to be considered [9]. In their model the energy contribution of a pair of rotationally symmetric molecules depends on the relative orientation of particles  $i$  and  $j$  represented by the unit vectors  $\hat{\mathbf{u}}_i$  and  $\hat{\mathbf{u}}_j$ , respectively. Maier and Saupe approximated the electrostatic interaction by the quadrupole moment of the multipole expansion via

$$u_{ij} = -J_{ij}P_2(\hat{\mathbf{u}}_i \cdot \hat{\mathbf{u}}_j) \quad (1.1)$$

where  $J_{ij}$  is the coupling constant and  $P_2$  is the second Legendre polynomial. From Eq. (1.1), a parallel alignment  $\hat{\mathbf{u}}_i \parallel \hat{\mathbf{u}}_j$  of the molecules in the nematic phase results in an energy gain, i.e. the total energy is lowered. This gain in energy exceeds the loss in orientational entropy such that the nematic state becomes stable when the temperature is lowered below the IN transition temperature. Despite the fact that steric effects are not included in the Maier-Saupe theory and the assumptions made are at least questionable, e.g. spherically symmetric distribution of centre-of-mass positions in the nematic state, its predictions of the properties of the nematic state are quite successful for a mean-field approach. Although in most cases approximation methods have to be used to calculate thermodynamic properties in the framework of Maier-Saupe theory the predictions for the thermotropic IN transition in liquid crystals are consistent with experiments, which explains the frequent use of this approach.

### *1.1.2 Influence of Substrates*

If a liquid crystal is confined between solid substrates, the nematogen forms layers due to symmetry breaking induced by the substrates. This stratification does not occur in bulk nematics from which one can anticipate, that confined liquid-crystalline phases

may exhibit molecular structures which have no counterpart in the bulk phase under identical thermodynamic conditions. The bulk is defined as the region of a sample in which the molecular structure depends only on the thermodynamic conditions and is not influenced by any boundaries. So how do substrates control the molecular structure of a confined nematic?

In 1913 Mauguin observed that substrates may dictate the alignment of liquid-crystalline molecules. He discovered that nematogens adjacent to cleaved mica substrates orient themselves parallel to the substrate surface but with a small tilt angle between the molecules' long axes and the optical axis of the substrate [16, 17]. The phenomenon that particles assume a substrate induced specific orientation to minimise the interfacial energy is called *anchoring* and the preferred orientation is termed *anchoring direction*. Different anchoring scenarios can be distinguished. In *degenerate planar* anchoring the molecules' long axes preferentially align parallel to the wall surface but can have any azimuthal orientation, as can be seen in Fig. 1.2(a). If the particles align parallel to the wall surface but in a specific in-plane direction we speak of *uniform planar* anchoring (see Fig. 1.2(b)). The anchoring is *homeotropic* if the molecules' long axes are preferentially orthogonal to the wall surface, as depicted schematically in Fig. 1.2(c).

Untreated glass substrates are a plain method to confine a liquid crystal. The long axes of the liquid-crystalline molecules are preferentially parallel to the wall surface but their in-plane orientation is largely arbitrary, i.e. glass substrates are an experimental realisation of *degenerate planar* anchoring. However, topological defects at the glass surface can introduce orientational disorder in the uniform nematic phase such that the in-plane orientation parallel to the substrate varies slowly [18]. As a consequence the homogeneous director  $\hat{\mathbf{n}}$  has to be replaced by a spatially dependent director field  $\hat{\mathbf{n}}(\mathbf{r})$ . When such a nematic phase is analysed between crossed polariser and analyser, so-called *schlieren* textures can be observed, as can be seen in Fig. 1.3. For further information on textures of liquid crystals see Dierking [18].

Three experimental methods are commonly used to introduce uniform anchoring at a substrate along a specific anchoring direction: treatment by mechanical work, the deposition of a thin layer of surfactant on the substrate, or the application of an external electric or magnetic field. A detailed review of these techniques is discussed in review articles by Cognard [19] and Jérôme [17] and books by Sonin [20] and Dierking [18]. If, for example, a glass substrate coated with a thin polymer layer is rubbed with a piece of cotton, the rubbing produces grooves which align the molecules with

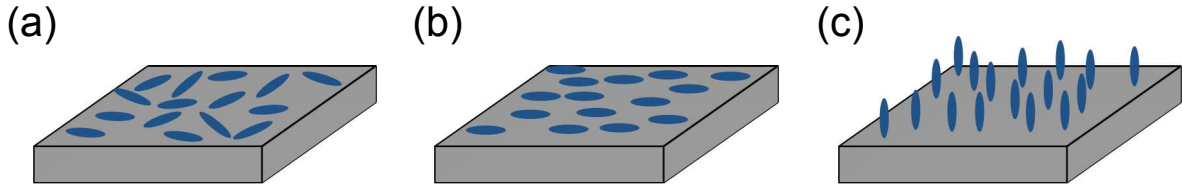


**Figure 1.2:** Schematic drawings of anchoring scenarios introduced by various surface treatments. Particles adjacent to a substrate with *degenerate planar* anchoring (a) are allowed to rotate freely in-plane whereas they are fixed to a specific direction for *uniform planar* anchoring (b). In *homeotropic* anchoring (c) the particles are preferentially oriented orthogonal to the substrate surface.

their long axes parallel to the direction of rubbing [21, 22]. The Chatelain rubbing method is a simple example of a method that produces *uniformly planar* anchoring substrates. *Homeotropic* anchoring is achieved in most cases by deposition of a surfactant, e.g. amphiphilic molecules such as, lecithin, stearic acid, or tensides, which align the liquid-crystalline particles by means of chemical bonds or steric effects [18, 20].

The orienting influence of the substrate is determined by the thickness  $\xi$  such that anchoring only acts on particles in distance  $d \lesssim \xi$  with respect to the substrate plane. In the absence of external orienting fields and under thermodynamic conditions of an isotropic bulk state,  $\xi$  is of the order of the molecular length such that only the contact layer is aligned by anchoring. However, this situation changes when the system is approaching the bulk IN transition. The elastic forces, which tend to orient all particles parallel to each other, impose the anchoring direction of the contact layer onto the bulk liquid crystal once the nematic state has formed. In this case  $\xi$  increases and can assume macroscopic values [17]. That means that in liquid crystals confined by a slit-pore the bulk nematic director is no longer arbitrary but is in fact mainly determined by the surface monolayer alignment [23]. If both substrates favour the same anchoring direction, the alignment in the confining cell and consequently the nematic director is homogeneous. This scenario is the *homogeneously aligned case*.

The homogeneous and uniform alignment may be “perturbed” either by the application of an external, orienting field or by hybrid anchoring scenarios, i.e. opposite substrates of the slit-pore favour different anchoring to which we will refer to as *hybrid aligned nematic* (HAN). The former was first observed by Fréedericksz and Zolina [24] who studied the influence of electric or magnetic fields superimposed onto a homeotropic aligned homogeneous nematic cell such that the direction of the field

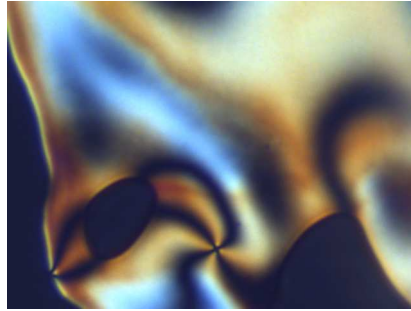


**Figure 1.3:** *Schlieren* texture of the nematic state between crossed polariser and analyser. The black brushes meet in a singular point which is the topological point defect. In the black areas the local director coincides either with the polariser or the analyser.

competes with the director induced by substrate anchoring. If the field exceeds a critical value, there is a realignment in the bulk area of the slit-pore. Fig. 1.4(a) shows the director field in a Fréedericksz cell after the transition. The magnetic field is applied parallel to the wall surfaces and aligns the particles in the bulk region in a planar fashion whereas if the wall separation is sufficient the orientation of the contact layer changes only slightly or is maintained.

The director field in a HAN slit-pore is shown in Fig. 1.4(b). In the nematic state the planar and the homeotropic anchoring substrates each impose their anchoring direction through elastic forces such that the resulting net alignment in the bulk may be perceived as a superposition of both anchoring scenarios. For sufficiently large wall separations, the liquid crystal is in a state in which the director field varies smoothly from homeotropic at the lower substrate to planar at the upper substrate, thereby minimising the interfacial energy at the expense of the elastic energy [25]. On account of the bend and splay deformations of the liquid crystal this state is named the bent state of the HAN slit-pore. However, the orientational order in a HAN slit-pore is highly dependent on the wall separation. Barbero and Barberi [20, 26] showed that if the distance separating the two substrates is smaller than a critical value the elastic energy becomes dominant such that the equilibrium orientation is uniform. The boundary condition of the weaker anchoring is no longer satisfied and the director of the pore is dictated by the stronger anchoring scenario [25].

Close to the IN transition, Chiccoli *et al.* [27] observed a transition from the bent state to a biaxial state which had also been predicted theoretically [28, 29]. In the

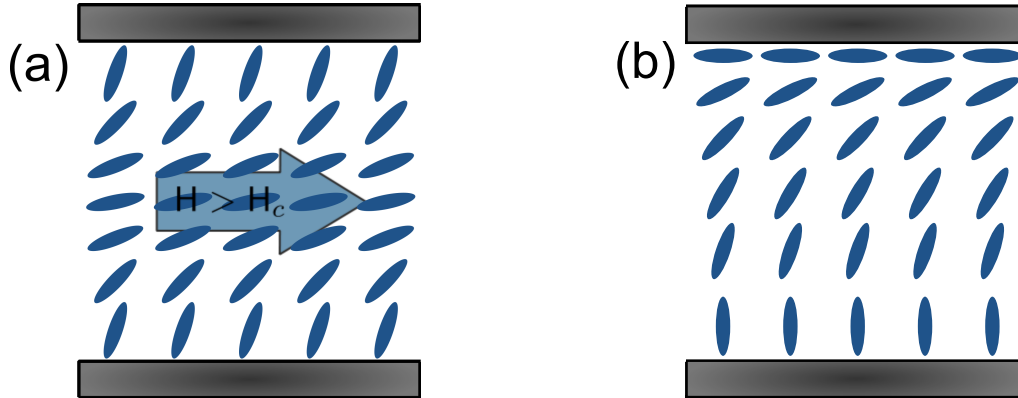


**Figure 1.4:** Local orientation in a slit-pore. (a) the director field in a Fréedericksz cell with homeotropic anchoring. The magnetic field  $H$  parallel to the substrate plane (blue arrow) exceeds the critical value  $H_c$  giving parallel bulk alignment. (b) the director field for a hybrid anchoring slit-pore in which the director field  $\hat{n}$  varies smoothly from homeotropic at the lower substrate to planar at the upper substrate.

biaxial state two uniformly oriented layers are separated by a sharp interface. The local orientation of each of the layers is dictated by the respective wall, i.e. the average orientations of the individual layers are perpendicular to one another. However, this state has not been verified experimentally because its existence is limited to a narrow temperature interval [27].

Cleaver and Teixeira [30] and Teixeira [31] investigated the local molecular structure of the hard Gaussian overlap model under hybrid anchoring conditions. The fluid substrate is modelled by the hard-needle wall potential [32]. In this model the anchoring direction and the anchoring strength are determined by the ratio  $\kappa_s/\kappa$  of the needle length to the length of the particles' long axes. However, these authors studied a model lyotropic liquid crystal and focused, in particular, on the influence of anchoring strength on the equilibrium state. Thus, a systematic study of the phase behaviour of a thermotropic liquid crystal under several hybrid anchoring conditions is still lacking.

### 1.1.3 Applications of Confined Liquid Crystals

The unique properties of confined liquid-crystalline materials have prompted a number of technical applications. In tribology, liquid crystals can be employed as lubricants

to reduce friction coefficients, wear rates, and contact temperature of sliding surfaces [33]. Thus they can be used to increase energy efficiency and extend the lifetime of machine parts. The liquid-crystalline molecules are adsorbed at the substrate as a close-packed ordered molecular layer which prevents direct contact of the machine parts and therefore produces lower friction than conventional lubricants particularly under high loads. It has even been reported that liquid crystals can act as “smart lubricants” under certain anchoring conditions. If surfaces start to come into contact due to increasing loads, a homeotropically anchored liquid crystal increases its viscosity without any applied external field [34]. In a way the liquid crystal responds to the changing conditions to avoid an increase in friction coefficient thereby minimising the wear rate.

The most prominent example of applications of liquid crystals is display technology [35, 36]. In liquid crystal displays (LCD) the molecules are reoriented by the application of an external field but when the field is switched off, thin polymer layers revert to the original surface induced alignment. Depending on whether these fields are switched off or on the liquid crystal may be transparent to visible light or not.

Despite the variety of technical applications of the optical activity of liquid-crystal materials, the focus here is on the growing field of clinical diagnosis tools, the “lab-on-a-chip”. In particular, we want to present some examples of biosensors which are devices sensitive for a biological process or structure [37]. Distortions of the uniform director or reorientations can be analysed by crossed polariser and analyser which eliminates the need for markers or tags to report orientational changes. Additionally, their relatively low price is another advantage of using liquid-crystal devices as diagnostic tools.

One possible realisation of a biosensor that can detect specific microbes in real-time consists of a solution of a non-toxic lyotropic liquid crystal (LLC) [38] with dissolved antigens (ligands). The LLC’s are uniformly aligned between polymer coated glass substrates such that the solution is opaque to polarised light. If microbes are added to the solution they bind to the antigens to form immune complexes that can distort the uniform nematic director by means of mechanical interaction [39]. The mechanical stress exerted by the immune complex on its surroundings is of the same magnitude as the elastic coefficients ( $\approx 1\text{pN}$ ) of the liquid crystal. If the diameter of the immune complex exceeds a critical value its existence is reported by a significant increase in transmitted light.

A similar biosensor setup with the living cells in their natural physiological environment, i.e. dissolved in water in a liquid-crystal matrix, is not applicable for thermotropic

liquid crystals (TLC). TLCs are insoluble in water [40] and most of them are toxic for biological cells [38, 41]. However, the alignment of TLCs at interfaces can be utilised to probe biological systems. For instance, a TLC can be coated by a thin film of extracellular matrix to which, say, human embryonic stem cells can bind [42]. If stem cells are bound the reorganisation of the matrix is coupled to a reorientation of the TLC which can be monitored by polarisation microscopy. The extracellular matrix prevents contact of the TLC with the stem cells such that a culture survives several weeks at the interface. For more examples of biosensors produced with liquid crystals and the variety of their applications see Woltman [37].

# Theoretical Background

This chapter introduces the general aspects of the system introducing phenomenological thermodynamics, followed by the statistical picture. We will derive statistical expressions for the thermodynamic potential and for response functions. To classify the IN transition we will recall the basic properties of phase transitions and introduce the concept to identify the order of a phase transition. The chapter will be closed by Landau's theory and its application to the IN transition.

## 2.1 Thermodynamic Potential

Consider a system that can interact through a boundary with its surroundings. Furthermore consider that this boundary can conduct heat, and that it is flexible but impermeable to particles. Under these conditions the set of natural variables  $\{N, T, P\}$  minimises an energy function, namely the Gibbs energy  $\mathcal{G}$ , in thermodynamic equilibrium. To every set of natural variables there is a unique energy function. By analogy to mechanical potentials, which assume a minimum in equilibrium, these energy functions are called thermodynamic potentials.

To identify the thermodynamic potential for a certain set of natural variables we recall Gibbs' fundamental equation

$$d\mathcal{U} = Td\mathcal{S} + dW \quad (2.1)$$

with  $dW$  the total, infinitesimal work exchanged between the system and its surroundings,  $\mathcal{S}$  is the entropy and  $\mathcal{U}$  the internal energy. Considering only chemical and mechanical work

$$dW = dW_{\text{chem}} + dW_{\text{mech}} \quad (2.2)$$

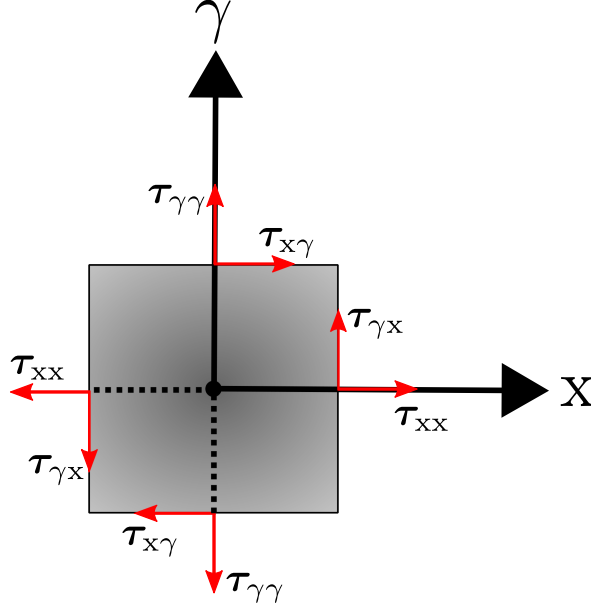


**Figure 2.1:** Side view of a parallelepiped and acting stress tensor components  $\tau_{\alpha\beta}$  drawn in red. The symbol  $\gamma$  can be either the  $y$  or  $z$  coordinate axis.

where

$$dW_{\text{chem}} = \mu dN \quad (2.3)$$

with  $\mu$  the chemical potential. Before we are able to write down an expression for the mechanical work contribution we recall that nanoconfined liquid crystals are anisotropic in at least one spatial direction and therefore the pressure along these directions is expected to differ from the bulk value. To take this anisotropy into account the mechanical work contribution may be expressed in terms of the pressure tensor  $\mathbf{P}$ . However, it is more convenient to base this derivation on the stress  $\boldsymbol{\tau}$  and the conjugate strain tensor  $\boldsymbol{\sigma}$ . Stress and pressure tensors are related via  $\boldsymbol{\tau} = -\mathbf{P}$  [43].

The stress  $\{\tau_{\alpha\beta}\}$  and the strain tensor  $\{\sigma_{\alpha\beta}\}$  can be represented mathematically by symmetric  $3 \times 3$  matrices [43, 44]. Next, turning to the physical interpretation of the components of  $\boldsymbol{\tau}$  one can imagine a fluid lamella with the shape of a parallelepiped (Fig. 2.1). It becomes obvious that the components  $\tau_{\alpha\beta}$  and  $\sigma_{\alpha\beta}$  can be interpreted as the  $\alpha$ -directed force acting on a  $\beta$ -directed face where  $\alpha$  and  $\beta$  are the axes of a Cartesian coordinate system. Moreover, it is apparent that all off-diagonal components with  $\alpha \neq \beta$  lead to shear deformations of the lamella, whereas diagonal elements result in dilation or compression. By convention  $\sigma_{\alpha\alpha} < 0$  for compression of the fluid lamella

and  $\tau_{\alpha\alpha} < 0$  if the force acting on the area points outwards. Due to the fact that this study addresses bulk and confined systems with unstructured surfaces, only diagonal elements of the tensors  $\boldsymbol{\tau}$  and  $\boldsymbol{\sigma}$  will be non-zero. Hence,  $\boldsymbol{\tau}$  and  $\boldsymbol{\sigma}$  are diagonal matrices of the form

$$\boldsymbol{\tau} = \begin{pmatrix} \tau_{xx} & 0 & 0 \\ 0 & \tau_{yy} & 0 \\ 0 & 0 & \tau_{zz} \end{pmatrix} \quad (2.4a)$$

$$\boldsymbol{\sigma} = \begin{pmatrix} \sigma_{xx} & 0 & 0 \\ 0 & \sigma_{yy} & 0 \\ 0 & 0 & \sigma_{zz} \end{pmatrix} \quad (2.4b)$$

This very brief introduction of stresses and strains permits us to express the mechanical work in terms of  $\boldsymbol{\tau}$  and  $\boldsymbol{\sigma}$  as

$$dW_{\text{mech}} = V_0 \text{Tr}(\boldsymbol{\tau} d\boldsymbol{\sigma}) \quad (2.5)$$

with  $V_0 = s_{x0}s_{y0}s_{z0} \equiv A_0s_{z0}$  the volume and  $\{s_{\alpha 0}\}$  the side lengths of the fluid lamella in an unstrained reference state. Here the symbol "Tr" denotes the trace of the tensor. Eqs. (2.3) and (2.5) can be used to obtain a new expression for Gibbs' fundamental equation

$$d\mathcal{U} = Td\mathcal{S} + \mu dN + V_0 \text{Tr}(\boldsymbol{\tau} d\boldsymbol{\sigma}) \quad (2.6)$$

By implementing two parallel, unstructured and atomistically flat surfaces separated by the distance  $s_{z0}$  the system becomes anisotropic in one spatial dimension, i.e. the symmetry of the phase is lowered. Assuming the substrate normal to be parallel to the  $z$  axis, the fluid will form layers in this direction whereas it is still homogeneous parallel to the wall surface. To take notice of this symmetry the diagonal components of the stress tensor given in Eq. (2.4a) can be rewritten as

$$\tau_{\parallel} \equiv \tau_{xx} = \tau_{yy} \quad (2.7a)$$

$$\tau_{\perp} \equiv \tau_{zz} \quad (2.7b)$$

Employing Eq. (2.7) it can be shown [43] that the mechanical work expression (Eq. (2.5)) can be recast in terms of  $\tau_{\parallel}$  and  $\tau_{\perp}$  as

$$dW_{\text{mech}} = \tau_{\parallel} s_{z0} dA + \tau_{\perp} A_0 ds_z \quad (2.8)$$

with  $A$  the area of the  $z$ -directed face and  $s_z$  the wall separation in some strained state. Inserting Eq. (2.8) into Eq. (2.6) leads to

$$d\mathcal{U} = Td\mathcal{S} + \mu dN + \tau_{\parallel} s_{z0} dA + \tau_{\perp} A_0 ds_z \quad (2.9)$$

which is a specialised form of Gibbs' fundamental equation. Note that in the limit  $s_z \rightarrow \infty$  the components of the stress tensor  $\tau_{\parallel} = \tau_{\perp} = -P_{\text{bulk}}$  reduce to the scalar bulk pressure and Eq. (2.9) converts to the standard textbook form valid for a bulk system.

At the beginning of this section we introduced a system in which the natural variables  $\{N, T, P\}$  determine the equilibrium state. Based on the realisation that in our system of ultimate interest the fluid is confined to a slit-pore with fixed side length  $s_{z0}$  we are interested in a specialised thermodynamic potential in which the side length is included in the set of natural variables. Moreover, to account for the anisotropy, the parallel component  $\tau_{\parallel}$  should be the driving force of the phase transition rather than the pressure  $P$ . Taking notice that we have already derived a specialised form of the exact differential of the internal energy  $d\mathcal{U}$ , we apply a double Legendre transform to Eq. (2.9)

$$\begin{aligned} d\mathcal{G}(T, N, \tau_{\parallel}, s_{z0}) &= d(\mathcal{U} - T\mathcal{S} - \tau_{\parallel} A s_{z0}) \\ &= -\mathcal{S}dT + \mu dN - A s_{z0} d\tau_{\parallel} + \tau_{\perp} A_0 ds_z \end{aligned} \quad (2.10)$$

to end up with the exact differential of a specialised form of the Gibbs free energy. Eq. (2.10) indicates that  $\{N, T, \tau_{\parallel}, s_z\}$  is the set of natural variables for the specialised form of  $\mathcal{G}$ .

## 2.2 The Molecular Description

Employing the concepts of statistical mechanics we are able to build the bridge to the molecular level. The concept of thermodynamic potentials presented in the preceding section has been introduced in the macroscopic framework. In order to derive a molecular expression analogous to Eq. (2.10) we have to introduce the so-called *partition function*. The partition function is a unique function within a statistical ensemble which incorporate the microscopic properties of the molecules as well as the set of natural variables. However, it is easy to verify that partition functions of different ensembles are linked and moreover are equivalent in infinite systems [43], i.e. the results of the

statistical formalism are independent of the choice of the ensemble. This equivalence is utilised in cases which are treated most conveniently in certain ensembles. Take as an example the ideal quantum gases. The canonical partition function

$$\mathcal{Q}(N, V, T) = \sum_j e^{-\beta E_j} = \sum_{\{n_k\}}^* e^{-\beta \sum_i \epsilon_i n_i} \quad (2.11)$$

can be calculated as the sum over all quantum states. The far right side of Eq. (2.11) follows, because

$$E_j = \sum_k \epsilon_k n_k \quad (2.12)$$

where  $n_k$  is the number of molecules in the molecular quantum state  $\epsilon_k$  while the system is in the quantum state with energy  $E_j$ . The asterisk in Eq. (2.11) indicates that the summation is restricted by  $\sum_k n_k = N$ . The constraint of a constant number of particles  $N$ , makes the evaluation of  $\mathcal{Q}$  rather cumbersome. However, in the grand canonical ensemble  $N$  is variable which leads to a double sum

$$\Xi(\mu, V, T) = \sum_{N=0}^{\infty} \sum_{\{n_k\}}^* \prod_k (\lambda e^{-\beta \epsilon_k})^{n_k} \quad (2.13)$$

with  $\lambda = e^{\beta \mu}$  the absolute activity. To evaluate the grand canonical partition function  $\Xi$  we still have to sum over  $n_k$ , constrained by a fixed value of  $N$ . But since we additionally sum over all possible values of  $N$ , Eq. (2.13) is equivalent to

$$\Xi(\mu, V, T) = \prod_k \sum_{n_k=0}^{n_k^{max}} (\lambda e^{-\beta \epsilon_k})^{n_k} \quad (2.14)$$

with  $n_k^{max}$  the maximum occupation number of the molecular quantum state  $k$ . That means the double sum in Eq. (2.13) can be reduced to a summation over all possible values of  $n_k$  independently of one another. This example shows that some problems are solved in certain ensembles with less effort [45].

### 2.2.1 The Partition Function

The connection between the thermodynamic treatment of the Gibbsian Potential introduced in Sec. 2.1 and the molecular level is then made through the expression [45]

$$\mathcal{G} = -k_B T \ln \chi \quad (2.15)$$

Here is  $\chi = \chi(T, N, \tau_{\parallel}, s_{z0})$  the isostress-isostrain partition function and  $k_B$  is Boltzmann's constant. A detailed derivation in Ref. 43 shows that

$$\chi = \sum_A \exp(\beta \tau_{\parallel} A s_{z0}) \mathcal{Q}_N \quad (2.16)$$

where  $\beta = 1/k_B T$  and  $\mathcal{Q}_N$  is the canonical partition function in the classical limit. For a molecular fluid consisting of uniaxial particles,  $\mathcal{Q}_N$  can be cast as

$$\mathcal{Q}_N = \frac{1}{N! h^{5N}} \int \exp[-\beta H(\mathbf{R}, \boldsymbol{\Omega}, \mathbf{P}_R, \mathbf{P}_\Omega)] d\mathbf{R} d\boldsymbol{\Omega} d\mathbf{P}_R d\mathbf{P}_\Omega \quad (2.17)$$

Uniaxial particles possess a main axis of rotational symmetry and can be either prolate or oblate. Common examples for prolate particles are ellipsoids of revolution [46–48] or spherocylinders [49–51] and discs or platelets are oblate particles [52]. In Eq. (2.17) it is assumed that the centre-of-mass positions and their conjugated momenta can be represented by the sets  $\mathbf{R} \equiv \{\mathbf{r}_1, \mathbf{r}_2, \dots, \mathbf{r}_N\}$  and  $\mathbf{P}_R \equiv \{\mathbf{p}_1, \mathbf{p}_2, \dots, \mathbf{p}_N\}$ , respectively. For particles with uniaxial symmetry, the orientation of individual molecules can be described by two Euler angles  $\omega_i = (\theta_i, \phi_i)$  such that the set of Euler angles  $\boldsymbol{\Omega} \equiv \{\omega_1, \omega_2, \dots, \omega_N\}$  represents the orientational degrees of freedom. The momenta conjugate to the orientations are given by the set  $\mathbf{P}_\Omega \equiv \{\mathbf{p}_{\omega_1}, \mathbf{p}_{\omega_2}, \dots, \mathbf{p}_{\omega_N}\}$ . In Eq. (2.17) Planck's constant  $h$  accounts for *Heisenberg's uncertainty principle*. In quantum mechanics the positions and momenta cannot be specified simultaneously with arbitrary precision. That means that in the classical limit the  $n$ -dimensional phase space is coarse-grained to volumes  $\propto h^n$  [53]. Additionally,  $h$  ensures  $\mathcal{Q}_N$  to be dimensionless. Due to the five degrees of freedom for axially symmetric particles (three translational and two rotational) the power of  $h$  is  $5N$ .

In the Hamiltonian [54]

$$H = K_t + K_r + U(\mathbf{R}, \boldsymbol{\Omega}) \quad (2.18)$$

the configurational part is determined by the intermolecular potential energy  $U(\mathbf{R}, \boldsymbol{\Omega})$ , whereas the translational and rotational kinetic energy contributions are given through

$$K_t = \sum_{i=1}^N \frac{\mathbf{p}_i^2}{2m} \quad (2.19a)$$

$$K_r = \sum_{i=1}^N \sum_{\alpha=x,y} \frac{J_{i,\alpha}^2}{2I} \quad (2.19b)$$

In Eq. (2.19)  $J_{i,\alpha}$  is the angular momentum component referred to the body-fixed principal axis  $\alpha$  of particle  $i$ ,  $I$  is the moment of inertia, and  $m$  the molecular mass. Eq. (2.17) together with Eqs. (2.18) and (2.19) suggests that the partition function  $\mathcal{Q}_N$  can be factorised into translational  $\mathcal{Q}_t$ , rotational  $\mathcal{Q}_r$ , and configurational  $\mathcal{Z}_N$  parts

$$\mathcal{Q}_N = \mathcal{Q}_t \mathcal{Q}_r \mathcal{Z}_N \quad (2.20)$$

However, it turns out that this is not possible immediately. The centre-of-mass positions  $\mathbf{R}$  and their conjugate momenta  $\mathbf{P}_R$  are independent and their contributions to Eq. (2.17) can be factorised. The integrals over translational momenta  $\mathbf{P}_R$  are Gaussian functions of the form

$$\mathcal{Q}_t = \int \exp\left(-\beta \sum_{i=1}^N \frac{\mathbf{p}_i^2}{2m}\right) d\mathbf{P}_R \quad (2.21)$$

This simple factorisation into kinetic and configurational parts cannot be applied to the rotational degrees of freedom. In Eq. (2.19b)  $K_r$  is expressed in terms of the angular momenta. However, as shown by Gray and Gubbins [54], the angular momenta  $\mathbf{J}^N = \mathbf{J}^N(\boldsymbol{\Omega}, \mathbf{P}_\Omega)$  are related to the Euler angles and their conjugate momenta. That means that  $K_r$  is not only a function of the angular momenta but it also depends on  $\mathbf{P}_\Omega$  through  $\mathbf{J}^N$  and  $\boldsymbol{\Omega}$  such that an integration over  $\mathbf{P}_\Omega$  similar to Eq. (2.21) cannot be carried out immediately.

One possible route to factorise the canonical partition function is to introduce the transformation  $\mathbf{P}_\Omega \rightarrow \mathbf{J}^N$  and integrate over  $\mathbf{J}^N$  instead [54, 55]. The Jacobian  $\mathfrak{J}^{(N)}$  for this transformation factorises into a product of single molecule terms [54]  $\mathfrak{J}^{(N)} = \mathfrak{J}_1 \mathfrak{J}_2 \mathfrak{J}_3 \dots \mathfrak{J}_N$ , because

$$|\mathfrak{J}_i| := \left| \frac{\partial(p_{\phi_i}, p_{\theta_i})}{\partial(J_{x_i}, J_{y_i})} \right| = \sin \theta_i \quad (2.22)$$

is independent of the  $\mathbf{p}_{\omega_j}$  for  $j \neq i$ . This permits us to rewrite Eq. (2.17) as

$$\mathcal{Q}_N = \frac{1}{N! h^{5N} 2^N} \int \exp\left(-\beta \mathcal{H}(\mathbf{R}, \hat{\mathbf{U}}, \mathbf{P}_R, \mathbf{J}^N)\right) d\mathbf{R} d\hat{\mathbf{U}} d\mathbf{P}_R d\mathbf{J}^N \quad (2.23)$$

where the set  $\hat{\mathbf{U}} \equiv \{\hat{\mathbf{u}}_1, \hat{\mathbf{u}}_2, \dots, \hat{\mathbf{u}}_N\}$  represents the orientations of the mesogens. The microscopic director  $\hat{\mathbf{u}}_i$  is a unit vector parallel to the long axis of particle  $i$  and is connected to the Euler angles  $\omega_i$  via

$$\hat{\mathbf{u}}_i = \begin{pmatrix} \cos \phi_i \sin \theta_i \\ \sin \phi_i \sin \theta_i \\ \cos \theta_i \end{pmatrix} \quad (2.24)$$

Additionally, in Eq. (2.23)

$$d\hat{\mathbf{u}}_i = \sin \theta_i d\theta_i d\phi_i \quad (i = 1, \dots, N) \quad (2.25)$$

The prefactor  $2^{-N}$  is included to account for the head-to-tail symmetry of the mesogen and to avoid double-counting of equivalent configurations characterised by  $\hat{\mathbf{u}}_i$  and  $-\hat{\mathbf{u}}_i$ .

Taking the transformation  $\mathbf{P}_\Omega \rightarrow \mathbf{J}^N$  into account the canonical partition function  $\mathcal{Q}_N$  can be factorised as indicated in Eq. (2.20) where the rotational contribution are Gaussians of the form

$$\mathcal{Q}_r = \int \exp \left( -\beta \sum_{i=1}^N \sum_{\alpha=x,y} \frac{J_{i,\alpha}^2}{2I} \right) d\mathbf{J}^N \quad (2.26)$$

The specific forms of  $\mathcal{Q}_t$  and  $\mathcal{Q}_r$  result from an analytic integration over translational and angular momentum subspaces

$$\mathcal{Q}_t = \left( \frac{2\pi m k_B T}{h^2} \right)^{3N/2} \equiv \frac{1}{\Lambda^{3N}} \quad (2.27a)$$

$$\mathcal{Q}_r = \frac{1}{\Lambda^{2N}} \left( \frac{I}{m} \right)^N \quad (2.27b)$$

with  $\Lambda$  the thermal De Broglie wavelength.

The configurational integral  $\mathcal{Z}_N$  in Eq. (2.20) is given by

$$\mathcal{Z}_N = \frac{1}{2^N N!} \int \int d\mathbf{R} d\hat{\mathbf{U}} \exp \left[ -\beta U(\mathbf{R}, \hat{\mathbf{U}}) \right] \quad (2.28)$$

Combining Eqs. (2.20), (2.27) and (2.28), the partition function of the isostress-isostrain ensemble in Eq. (2.16) can be expressed as

$$\chi = \frac{1}{\Lambda^{5N}} \left( \frac{I}{m} \right)^N \sum_A \exp(\beta \tau_{\parallel} A s_{z0}) \mathcal{Z}_N \quad (2.29)$$

### 2.2.2 Response Functions

Many measurable thermodynamic observables, such as susceptibility and heat capacity, measure the response of a system to an external stimulus and are defined as ratios of variations of extensive or intensive variables [56]. Therefore, to compare theory and experiment it is worthwhile to have statistical analogues of these response coefficients.

Mathematically, response functions are defined as mixed second derivatives of the corresponding thermodynamic potential. From the symmetry of the second derivatives non-trivial Maxwell relations between response coefficients can be deduced [56]. These can be used to determine response coefficients which may not be measured directly in experiments. A prominent example is the identity

$$c_P - c_V = \frac{TV\alpha^2}{\kappa_T} \quad (2.30)$$

between the specific heats at constant pressure  $c_P$  and constant volume  $c_V$ , the expansion coefficient  $\alpha$  and the isothermal compressibility  $\kappa_T$ .

For our system the isostress-isostrain partition function (2.29) is a crucial quantity. It is linked to a molecular expression of the Gibbs potential (2.15) and therefore provides access to response functions based on molecular properties. In the context of this study two response coefficients are of particular interest, the isothermal compressibility  $\kappa_T$  and the isostress heat capacity  $c'_\tau$  (using the prime for later convenience). They are defined as

$$\left(\frac{\partial^2 \mathcal{G}}{\partial T^2}\right)_{\{\cdot\} \setminus T} = - \left(\frac{\partial \mathcal{S}}{\partial T}\right)_{\{\cdot\} \setminus T} \equiv -\frac{c'_\tau}{T} \quad (2.31a)$$

$$\left(\frac{\partial^2 \mathcal{G}}{\partial \tau_{\parallel}^2}\right)_{\{\cdot\} \setminus \tau_{\parallel}} = -s_{z0} \left(\frac{\partial A}{\partial \tau_{\parallel}}\right)_{\{\cdot\} \setminus \tau_{\parallel}} \equiv -As_{z0}\kappa_T \quad (2.31b)$$

In Eq. (2.31) we use the shorthand notation " $\{\cdot\} \setminus x$ " to indicate that upon differentiation the set of natural variables of  $\mathcal{G}$  is to be held constant except for variable " $x$ ".

Within the framework of fluctuation theory the fluctuations of an ensemble average can be associated with the corresponding susceptibility [45]. This makes it possible to evaluate molecular expressions for the response functions as thermal fluctuations of mean values. In other words, response coefficients can be calculated in terms of the variance of certain ensemble averages.

A detailed derivation of the susceptibilities used in this work will be given in chapter 4 so that at this point it seems sufficient to present the final equations

$$\frac{c'_\tau}{N} = c_\tau = \frac{5}{2}k_B + \frac{\langle \mathcal{H}^2 \rangle - \langle \mathcal{H} \rangle^2}{Nk_B T^2} \quad (2.32a)$$

$$\kappa_T = \frac{s_{z0}}{k_B T} \frac{\langle A^2 \rangle - \langle A \rangle^2}{\langle A \rangle} \quad (2.32b)$$

where we have introduced

$$\mathcal{H}(\mathbf{R}, \hat{\mathbf{U}}) \equiv U(\mathbf{R}, \hat{\mathbf{U}}) - \tau_{\parallel} A s_{z0} \quad (2.33)$$

as a specialised molecular enthalpy for later convenience. In Eq. (2.32) the symbol  $\langle \dots \rangle$  denotes an average of an observable  $\mathcal{O}$  in the isostress-isostrain ensemble, that is given by

$$\langle \mathcal{O} \rangle = \sum_A \iint d\mathbf{R} d\hat{\mathbf{U}} \mathcal{O}(\mathbf{R}, \hat{\mathbf{U}}) p(\mathbf{R}, \hat{\mathbf{U}}; A) \quad (2.34)$$

with

$$p(\mathbf{R}, \hat{\mathbf{U}}; A) = \frac{1}{2^N N! \Lambda^{5N} \chi} \exp\left(-\beta \mathcal{H}(\mathbf{R}, \hat{\mathbf{U}})\right) \quad (2.35)$$

the probability density which depends on  $A$  implicitly. It is defined such that

$$p(\mathbf{R}, \hat{\mathbf{U}}; A) d\mathbf{R} d\hat{\mathbf{U}}$$

is the probability of finding the positions and orientations in the element  $d\mathbf{R} d\hat{\mathbf{U}}$  about the configuration  $(\mathbf{R}, \hat{\mathbf{U}})$  of the mesogens. Note that

$$\int p(\mathbf{R}, \hat{\mathbf{U}}; A) d\mathbf{R} d\hat{\mathbf{U}} = 1$$

## 2.3 Phase Transitions

The purpose of this section is to review the basics of phase transition theory. Although the IN transition in liquid crystals is at the focus of this work, Sec. 2.3.1 provides the universal rules to classify the order of a phase transition in general. Later we will present the phenomenological Landau theory of phase transitions which can be extended to the IN transition by minor changes. However, we first have to define a macroscopic nematic order parameter before we present the Landau-De Gennes theory of the IN transition.

### 2.3.1 Classification of Phase Transitions

In general, a phase transition is defined as a change in a macroscopic property of a substance dictated by a shift in the thermodynamic field  $\Upsilon$  (e.g. temperature  $T$ , pressure  $P$  or chemical potential  $\mu$ ). According to the classification of Ehrenfest, a phase transition of the  $n$ -th order exhibits a discontinuity in the  $n$ -th derivative of an appropriate

thermodynamic potential with respect to  $\Upsilon$ , whereas all  $n - 1$  preceding derivatives are continuous. Nowadays it is convenient to follow the more general classification introduced by Fisher [57]: if the first derivative is discontinuous the transition is defined as a *first-order* phase transition. If, on the other hand, the first derivative is continuous but the second or higher derivatives are either discontinuous or infinite it is a *continuous* transition [58].

Some of these phase transitions involve symmetry-breaking. The symmetry of a system is defined by a set of geometrical transformations under which the equilibrium configurations of the constituting particles in the considered phase are invariant. Then a high symmetry is given by a set containing a large number of geometrical transformations under which the system is preserved. Take as an example a gas. It is immediately apparent that this state is isotropic and homogeneous and serves therefore as an example for a high symmetry state. Isotropic systems are invariant under all rotations and reflexions of the system, whereas homogeneous systems are invariant under translations. In this state it is obvious that also after a large number of translations and rotations the equilibrium positions of the particles will be preserved.

In a crystal the particles are restricted to specific lattice sites and therefore the assumptions of isotropy and homogeneity are no longer valid. Hence, only a finite number of transformations will preserve the symmetry of the unit cell and therefore the equilibrium positions of the particles. Thus the crystal is an example of a state with low symmetry.

Within this picture it is apparent that in the low symmetry state there are long-range correlations of the centres-of-mass between the particles because the particles are fixed to certain positions. In contrast, in the high symmetry state the particles are free to move and therefore entirely local correlations exist. Due to these long-range correlations we will denote the low symmetry case as the high-order state and a system with high symmetry as the low-order state.

### 2.3.2 Order Parameters and Phase Transitions

The symmetry of the system can be measured by choosing a proper order parameter  $\Phi$  which quantifies the difference between the configuration in the low-order and in the high-order state when the transition point  $\Upsilon_c$  is crossed. On account of this symmetry-breaking a general definition of the order parameter should fulfil two requirements [59]:

- (i)  $\Phi = 0$  in the low-order (high symmetry) state
- (ii)  $\Phi \neq 0$  in the high-order (low symmetry) state

Notice that these requirements do not define the order parameter in a unique way and that the order parameter has to be chosen depending on the nature of the phase transition. Take as a simple example the gas-liquid transition, where both states can be clearly distinguished by their density. For this transition a proper order parameter should be defined in terms of the density of the system. The IN transition, on the other hand, involves symmetry-breaking from a state with orientational short-range correlations (isotropic) to a state with orientational long-range correlations (nematic). To account for these orientational long-range correlations we will present in Sec. 2.4.2 the definition of a so-called nematic order parameter.

Assuming that the symmetry changes when  $\Upsilon_c$  is passed, the concept of order parameters can be used to describe phase transitions. As Landau showed in his seminal paper [60] close to the order-disorder transition the thermodynamic potential in the high-order state can be expressed as an expansion in terms of the order parameter  $\Phi$ . Providing that the extensive parameter  $\Phi$  can be treated as a natural variable of the thermodynamic potential, a thermodynamic conjugate intensive “field”  $h_\Phi$  can be associated, which couples directly to  $\Phi$  [61]. Therefore, the term  $-h_\Phi\Phi$  has to be included in the thermodynamic potential. As a consequence, the first derivative of the thermodynamic potential with respect to the “field”

$$\Phi = - \left( \frac{\partial \mathcal{G}}{\partial h_\Phi} \right) \quad (2.36)$$

is defined as the order parameter, assuming that the Gibbs potential  $\mathcal{G}$  can serve as the thermodynamic potential.

Applying to Eq. (2.36) the classification of phase transitions given by Fisher, a *first-order* phase transition is then indicated through a discontinuity in the order parameter, whereas a *continuous* transition can be identified by a continuous change of  $\Phi$ . This is illustrated schematically in Fig. 2.2. In case of a *first-order* transition the slope of the relevant thermodynamic potential changes discontinuously whereas the potential itself remains a continuous function of the field driving the transition. If, on the other hand, the profile of  $\mathcal{G}$  is smooth everywhere then  $\Phi$  shows no jump and the system undergoes a *continuous* transition. In Fig. 2.2 the behaviour of a finite system is shown. The cartoons have to be modified slightly if the thermodynamic limit is approached. In the case of an infinite system there are no metastable branches for

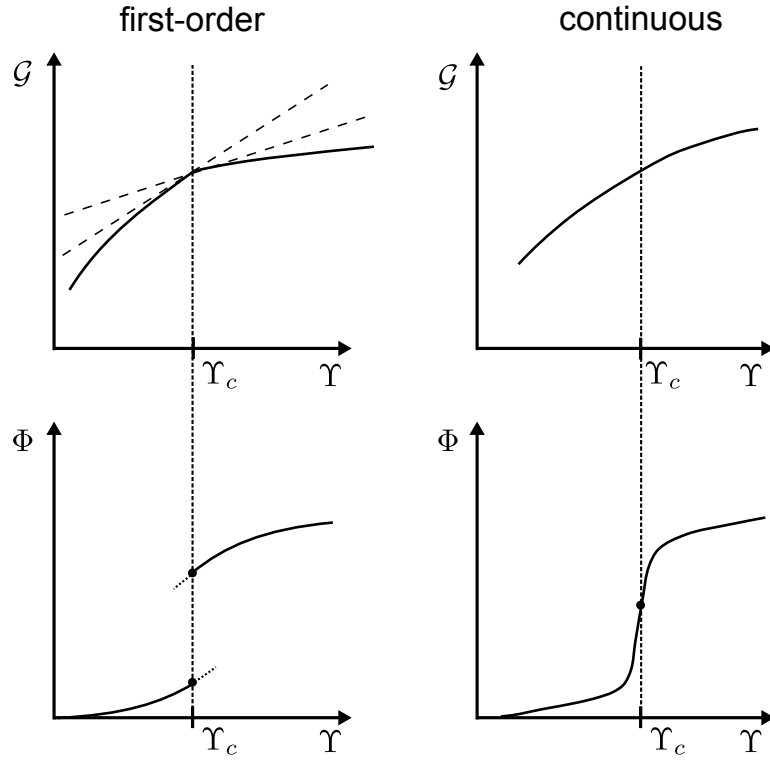


**Figure 2.2:** Gibbs free energy  $\mathcal{G}$  and the order parameter  $\Phi$  as a function of the applied driving field  $\Upsilon$  displayed on an arbitrary ordinate scale. The vertical dotted lines are drawn at the transition point  $\Upsilon_c$ . The left and right panel show a transition of the *first-order* and *continuous* class, respectively. Dashed lines show the tangents at the discontinuity in slope and the metastable branches (dotted) occurring at a *first-order* transition due to hysteresis.

a *first-order* transition and the slope of  $\Phi$  at the transition point is infinity for a *continuous* transition. Moreover, the order parameter is exactly zero for an infinite system in the low-order state.

The distribution function  $\mathcal{P}(\Phi)$  of the order parameter is another useful tool to determine the nature of phase transitions. The quantity  $\mathcal{P}(\Phi)d\Phi$  is then defined as the probability of finding  $\Phi$  in the interval  $[\Phi, \Phi + \Delta\Phi]$ . In computer simulations,  $\mathcal{P}(\Phi)$  can be obtained as a histogram with bin width  $\Delta\Phi$ . As shown by Eppenga and Frenkel [52], the order parameter distribution  $\mathcal{P}(\Phi)$  is connected to a Gibbs energy functional

$$\mathcal{G}'(\Phi) = -k_B T \ln \mathcal{P}(\Phi) \quad (2.37)$$

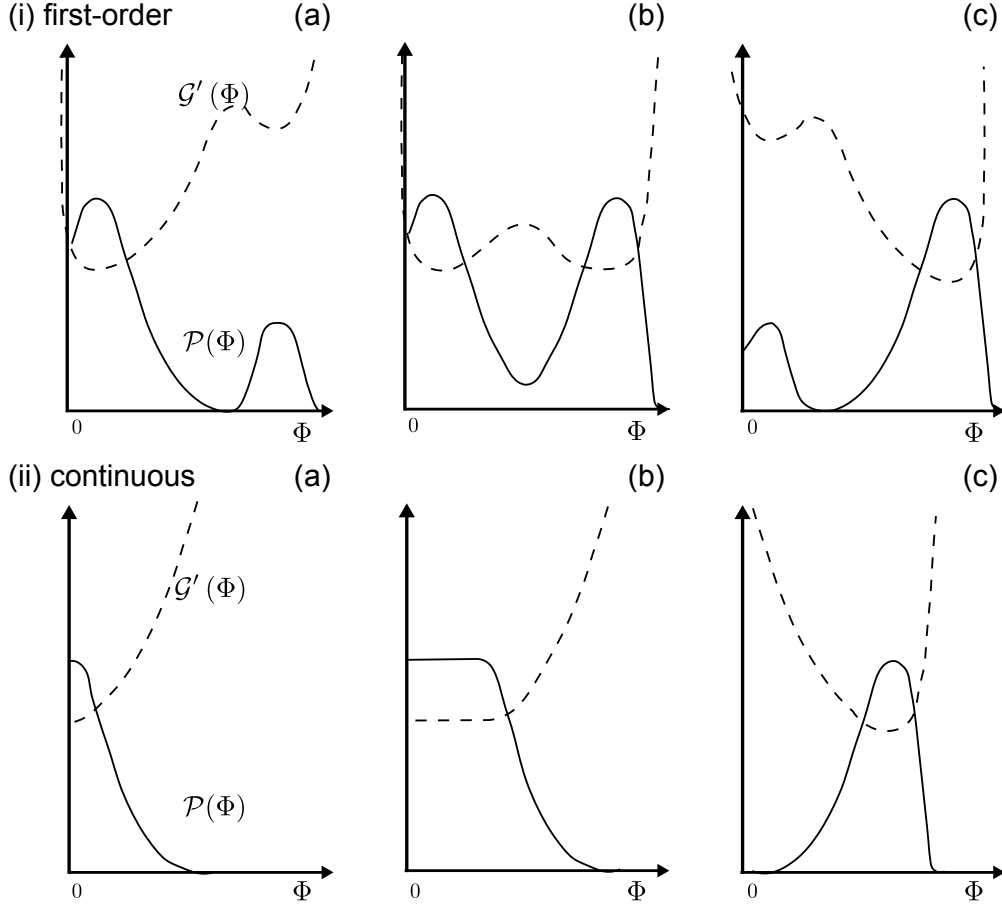


**Figure 2.3:** The order parameter distribution  $\mathcal{P}(\Phi)$  (solid) and the corresponding Gibbs energy functional  $\mathcal{G}'(\Phi)$  (dashed) for a finite system undergoing a *first-order* transition (upper panel) or *continuous* transition (lower panel). From left to right: the distributions for values of the thermodynamic field  $\Upsilon$  (a) immediately before (low-order state), (b) at, and (c) immediately after (high-order state) the transition are shown. The ordinate and abscissa scales are arbitrary. (cf. Mouritsen [61])

That means that calculating a histogram of the order parameter distribution  $\mathcal{P}(\Phi)$  also provides a possible route to “measure” the Gibbs energy functional  $\mathcal{G}'(\Phi)$  (see Fig. 2.3).

Let us consider the case of a *first-order* transition and assume that the system is in the low-order state. While approaching  $\Upsilon_c$ , a second maximum at a non-zero value of  $\Phi$  appears in the distribution function in the vicinity of the phase transition

(Fig. 2.3(ia)). In this bimodal structure the side maximum at  $\Phi \neq 0$  in  $\mathcal{G}'$  is clearly smaller than the peak at  $\Phi = 0$ , i.e. the side maximum corresponds to a metastable high-order state. In Fig. 2.3(ib)  $\Upsilon \approx \Upsilon_c$ , i.e. at the phase transition, the bimodal distribution becomes symmetrical and the two states are equally probable. To be more precise, this is the only point where the two states are stable and coexist. While further shifting  $\Upsilon$ , immediately after the transition the peak at finite  $\Phi$  increases whereas the peak at  $\Phi \approx 0$  decreases (see Fig. 2.3(ic)). The dominant peak at  $\Phi \neq 0$  reflects that the stable state is now the high-order state. Nevertheless, a finite system may be trapped in the low-order state when the transition point  $\Upsilon_c$  is crossed. This effect gives rise to the metastable branches in Fig. 2.2.

In Fig. 2.3(ii) the distribution  $\mathcal{P}(\Phi)$  of a *continuous* transition is single-peaked. The corresponding Gibbs potential  $\mathcal{G}'$  in Fig. 2.3(ia) immediately before the transition is therefore characterised by a single minimum, and no metastable higher order state exists. At the transition point  $\Upsilon_c$  the distribution  $\mathcal{P}(\Phi)$  is widened and the maximum is shifted smoothly to the high-order state (Fig. 2.3(iib)). After the transition point is passed the distribution in Fig. 2.3(iic) about a finite value  $\Phi$  becomes sharper again. As a consequence of this continuous shift of the maximum value of  $\mathcal{P}(\Phi)$  the profile of the order parameter plotted against the thermodynamic field is continuous (cf. Fig. 2.2).

### *“Ideal” first-order in computer simulations?*

The “ideal” behaviour of a *first-order* phase transition, i.e. the discontinuity at  $\Upsilon_c$ , is only observed in the thermodynamic limit. It is defined by taking the limit of an infinitely large system ( $V \rightarrow \infty$ ) containing an infinite number of particles ( $N \rightarrow \infty$ ) such that the number density  $\rho = N/V$  remains constant. Of course, the thermodynamic limit cannot be realised in a computer simulation, although at the time of writing simulations with up to a million particles are feasible. Thus, in a computer simulation one is confronted with effects caused by the finite size of the system under study. For example, the locations of the two peaks in the bimodal distribution are system-size dependent, i.e. the peaks will merge if the system is not sufficiently large. Nevertheless, in a computer simulation of sufficient size the individual peaks and the corresponding minimum in  $\mathcal{G}'$  can be resolved at the transition point. The shape of the distribution  $\mathcal{P}(\Phi)$  in a finite system is not Gaussian but shows an asymmetrical tail as Mouritsen [61] points out. This asymmetry becomes more pronounced the closer the driving field  $\Upsilon$  gets to  $\Upsilon_c$  and leads to less accurate mean values of the order parameter.

The stable and metastable states are separated by a free energy barrier which

is of finite height in a finite-size system. Therefore, transitions between both states are possible with finite probability. This has the consequence that the profile of the order parameter  $\Phi$  for a *first-order* transition in Fig. 2.2 appears to be “smeared” out in a computer simulation and the expected discontinuity in  $\Phi$  at  $\Upsilon_c$  may appear as a continuous change in order. This “smearing” of the order parameter profiles for finite systems conceals the nature of the phase transition in computer simulations and additional methods to determine the order of the phase transition have to be considered. Although, the bimodal structure of  $\mathcal{P}(\Phi)$  close to the transition point is a strong indication of a *first-order* transition it should not be seen as a unique fingerprint of that kind of a transition class. This is due to the fact that in a series of simulations, while varying  $\Upsilon$ , one may miss the transition point, because  $\Upsilon_c$  is *a priori* unknown and the interval of bimodal structure might be quite narrow. A powerful tool to determine the nature of phase transitions in computer simulations is provided by the cumulant method introduced by Binder [62]. The cumulant method and its application to the IN transition will be presented in Sec. 3.3.

## 2.4 Landau Theory

The purpose of this section is to provide the reader with the basics of Landau’s theory. Landau originally applied the theory to *continuous* phase transitions, such as unit cell transformations of a crystalline structure [60]. Employing these basic concepts we will show that this theory can be extended to describe the IN phase transition. De Gennes [63] was the first one to show that this is possible.

### 2.4.1 Basic Concepts

Landau’s theory has the charm of being rather simple and easy to apply to phase transitions which involve symmetry breaking. In this phenomenological theory the symmetry of the system is quantified by a spatially invariant, scalar order parameter  $\Phi$ . The order parameter is constructed in such a way that  $\Phi = 0$  in the low-order state and  $\Phi \neq 0$  in the high-order state. To understand the generality of Landau’s theory, it is useful to compare it with the molecular Maier-Saupe theory. Maier-Saupe theory deals directly with the molecular details of the interaction. However, as was shown in the introduction, Maier and Saupe consider a simplifying approximation of the intermolecular potential. Landau’s theory, being built on general symmetry arguments,

does not run the risk of oversimplifying molecular interactions, because it focuses on the macroscopic order parameters [6].

Let us consider the equilibrium state of a macroscopic system at constant pressure  $P$  and temperature  $T$  such that thermodynamic equilibrium states correspond to minima of the Gibbsian potential. In the direct vicinity of a *continuous* phase transition the order parameter is expected to assume relatively small values. Based upon these assumptions Landau postulated that close to the phase transition thermodynamic quantities can be obtained by expanding the thermodynamic potential as a power series in terms of  $\Phi$ . The Landau potential can be expressed by

$$\mathcal{G}(P, T, \Phi) = \mathcal{G}_0(P, T) + h\Phi + A\Phi^2 + B\Phi^3 + C\Phi^4 + \dots \quad (2.38)$$

Here the coefficients  $h, A, B, C, \dots$  are functions of  $P$  and  $T$ , and  $\mathcal{G}_0$  is the Landau potential for  $\Phi = 0$ . Although Eq. (2.38) suggests  $\mathcal{G}(P, T, \Phi)$  is a function of  $\Phi$  as well, it has to be noted that  $\Phi$  is not on equal footing with  $P$  and  $T$  [64]. The value of  $\Phi$  is defined through the equilibrium state of the thermodynamic potential for given values of pressure and temperature, whereas  $P$  and  $T$  can be chosen arbitrarily.

If the system is in equilibrium, the Landau potential  $\mathcal{G}(P, T, \Phi)$  assumes a minimum. Following the argumentation of Vertogen [9], this means that  $\mathcal{G}(P, T, \Phi)$  has to preserve the stability conditions

$$\frac{\partial \mathcal{G}}{\partial \Phi} = 0 \quad ; \quad \frac{\partial^2 \mathcal{G}}{\partial \Phi^2} > 0 \quad (2.39)$$

for arbitrary values of  $P$  and  $T$ . At the transition point the two states with different symmetry  $\Phi = 0$  and  $\Phi \neq 0$  coexist and the stability conditions modify to

$$\frac{\partial \mathcal{G}}{\partial \Phi} = 0 = h \quad (2.40a)$$

$$\frac{\partial^2 \mathcal{G}}{\partial \Phi^2} = 0 = A \quad (2.40b)$$

In Eq. (2.40a),  $h = 0$  because of  $\mathcal{G}(P, T, \Phi)$  being minimal for  $\Phi = 0$ . Assuming isothermal conditions  $A = a(P_c - P)$  with  $a = (\partial A / \partial P)_{P_c} > 0$  which follows directly from (2.40b), if  $P$  is driving the transition and  $P_c$  is the transition pressure. It is evident that  $A > 0$  is necessary if  $P < P_c$  such that the equilibrium state corresponds to a minimum in  $\mathcal{G}(P, T, 0)$ . On the other hand, if the transition point  $P_c$  is passed, the minimum in  $\mathcal{G}(P, T, \Phi)$  is shifted to non-zero values of  $\Phi$  whereas at  $\Phi = 0$  a local maximum exists. This is realised by negative values of  $A$ . In other words, to account for the stability condition (2.40b)  $A$  has to change sign at the transition point. Fig. 2.4

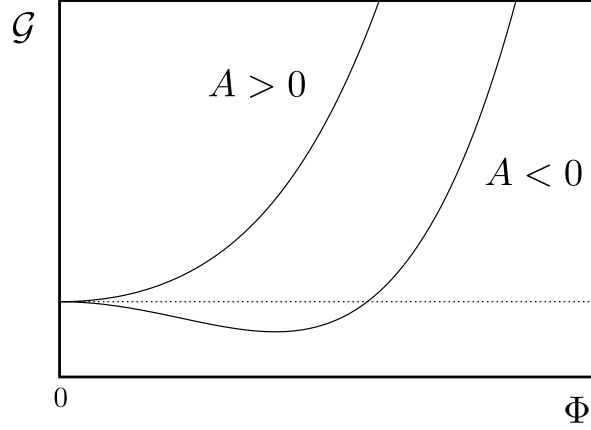


**Figure 2.4:** Plots of the Landau potential  $\mathcal{G}$  given in Eq. (2.38) as a function of  $\Phi$  for the two cases  $A < 0$  and  $A > 0$ . Terms up to the fourth power are included where the coefficient  $C$  has been assumed to be positive and small.

shows the Landau potential  $\mathcal{G}(P, T, \Phi)$  as a function of  $\Phi$  in arbitrary units and its dependence on the sign of the second coefficient  $A$ . More specifically, the Eqs. (2.40a) and (2.40b) indicate that the thermodynamic function  $\mathcal{G}(P, T, \Phi)$  at the transition pressure  $P_c$  is characterised by a saddle point.

Let us now turn to the coefficients linked to the cubic and higher order terms in Eq. (2.38). They are determined by the thermodynamic behaviour of the system which follows directly from writing down the stability condition (2.39) explicitly

$$\frac{\partial \mathcal{G}}{\partial \Phi} = 0 = a(P_c - P)\Phi + B\Phi^2 + C\Phi^3 + \dots \quad (2.41)$$

It is a simple matter to prove that Eq. (2.41) has the following solutions [9]

$$\Phi = 0 \quad (2.42a)$$

$$\Phi = \frac{B \pm \sqrt{B^2 - 4aC(P_c - P)}}{2C} \quad (2.42b)$$

The solution in Eq. (2.42a) corresponds to the low-order state. If the order parameter is symmetric, the solution in Eq. (2.42b) now requires that the coefficient  $B = 0$  vanishes for a *continuous* transition as we will explain soon. This permits us to rewrite Eq. (2.42b) for the high-order state as

$$\Phi = \pm \left( \frac{a(P - P_c)}{C} \right)^{1/2} \quad (2.43)$$

The existence of an equilibrium state is ensured if the coefficient  $C > 0$  is positive. In general, to account for the existence of an equilibrium state, the last term in the expansion of  $\mathcal{G}(P, T, \Phi)$  should be of even order and the related coefficient be positive.

Concerning the symmetry, let us now consider the coefficients linked to terms of odd order in  $\Phi$  for *continuous* transitions. If no external field is applied to the system the invariance of the Landau potential  $\mathcal{G}(P, T, \Phi)$  has to be preserved while replacing the scalar order parameter  $\Phi$  by  $-\Phi$ . Take, for example, a binary alloy AB with a simple cubic unit cell [9]. In the high-order state, atom  $A$  is at the vertices and atom  $B$  at the centre of the unit cell. In this system the order parameter determines if the lattice site is occupied by atom  $A$  or  $B$ , where the first case corresponds to  $\Phi$  and the latter to  $-\Phi$ . For this simple example it becomes immediately clear that the Landau potential  $\mathcal{G}(P, T, \Phi) = \mathcal{G}(P, T, -\Phi)$  has to be equal for both values of  $\Phi$ . From similar symmetry considerations one can draw the conclusion that in the expansion (2.38) all odd-terms have to vanish for *continuous* phase transitions. In a system with an applied external field, however, there is no reason why the Landau potential  $\mathcal{G}(P, T, \Phi)$  should be invariant under exchange of  $\Phi$  and  $-\Phi$ . Thus, for systems with an applied external field the linear term is included in the expansion.

Landau already addressed [60] the nature of the transition point and the related value of the coefficient  $B$  of the cubic term. More specifically, he analysed the vicinity of *continuous* phase transition points for the two cases  $B = 0$  and  $B \neq 0$ . If  $B = 0$  the only condition for a *continuous* phase transition is the vanishing second coefficient  $A = 0$  discussed above. Such a transition point is called a Curie point and is part of a certain line in the  $(PT)$ -plane which is determined by  $A = 0$ . This line of *continuous* phase transitions is named the Curie line. On the other hand, for a non-zero third-order coefficient  $B \neq 0$ , a *continuous* transition occurs only at certain points, i.e. there is no Curie line. This means that at a *continuous* transition point the conditions  $A = B = 0$  have to be fulfilled. These points are isolated in the  $(PT)$ -diagram and may appear at the intersections of lines of *first-order* transitions [60, 65]. In particular, these considerations imply that non-zero cubic terms  $B \neq 0$  are one possible realisation of *first-order* transitions in the Landau theory [66]. If the symmetry of the scalar order parameter does not allow cubic terms, a second route to *first-order* transitions is provided by a vanishing cubic term and an extension to terms up to the sixth power in  $\Phi$ .

To illustrate the influence of the coefficient  $B$  on the Landau potential, plots of  $\mathcal{G}(P, T, \Phi)$  for vanishing and non-vanishing  $B$  are shown in Fig. 2.5. In Fig. 2.5(a) the

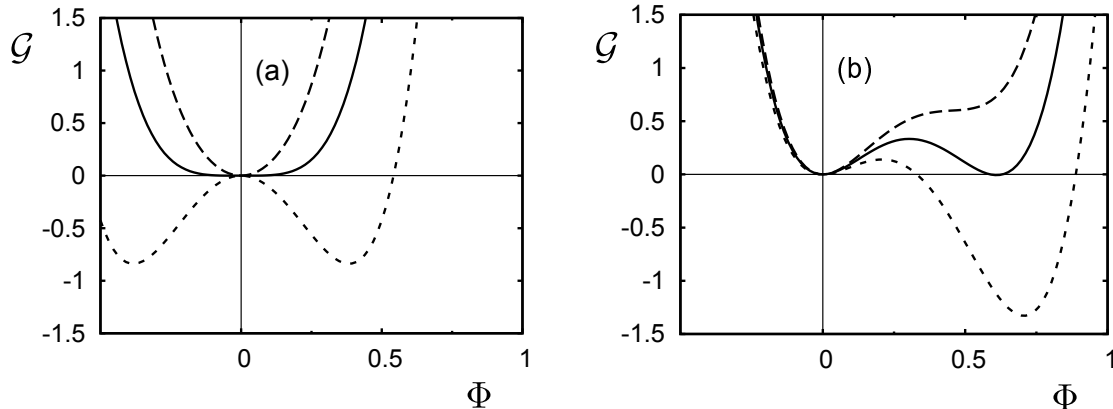


**Figure 2.5:** Plots of the Landau potential  $\mathcal{G}$  (Eq. 2.38) in arbitrary units just before (-----), at (——) and soon after (— · —) the transition, for (a)  $B = 0$  and (b)  $B \neq 0$ . Arbitrarily  $\mathcal{G}_0 = 0$  and  $\Phi \in [-1, 1]$ .

Landau potential with a vanishing coefficient  $B = 0$  is plotted in arbitrary units as a function of the scalar order parameter  $\Phi$ . The Landau potential exhibits a widened but single minimum at the transition point which is characteristic of a *continuous* transition (cf. Fig. 2.3). If, on the other hand, a non-zero  $B$  is included in the expansion,  $\mathcal{G}(P, T, \Phi)$  exhibits two minima at the transition point which are separated by an intermittent maximum. We have seen that this is the double-minimum structure characteristic of a *first-order* transition. This bimodal structure is illustrated in Fig. 2.5(b).

### 2.4.2 Macroscopic Nematic Order Parameter

In Landau's phenomenological theory the thermodynamic potential is expressed as an expansion in terms of a macroscopic order parameter  $\Phi$ . A macroscopic order parameter is a global physical quantity which depends on neither the actual shape nor on the interaction of the constituting molecules. In order to introduce the macroscopic order parameter we will adopt the argumentation of Gramsbergen *et al.* [59].

Order parameters measure the symmetry of a system and can in general be represented by tensors of rank zero, one or two. The physics of the system dictate which tensor can be used. Let us recall the simple example of the liquid-gas transition given in Sec. 2.3.2. Here, the density distinguishes the two states and can be used as an order parameter. Clearly, in this case the order parameter is a scalar. In a simple

ferromagnet the order and disorder states differ in their magnetisation. In this system the order parameter is a vector and is given as the thermal average of the molecular magnetic moment. With regard to liquid crystals, which rank can be used to construct the nematic order parameter?

In the nematic state the molecules' long axes are aligned, which results in a lower cylindrical symmetry. To account for this orientational long-range order we assume the orientation of the long axes of the molecules is given through the three-dimensional unit vector  $\hat{\mathbf{u}}$  defined in Sec. 2.2.1. We now have to check how the various tensor types can be expressed in terms of the molecular orientation  $\hat{\mathbf{u}}$ . If the nematic order parameter were a scalar, the averaging would contain scalar products of the form  $\langle \hat{\mathbf{u}} \cdot \hat{\mathbf{u}} \rangle$  which are unity by definition. It is apparent that the nematic order parameter cannot be represented by a scalar. For the next higher rank one we find that thermal averages  $\langle \hat{\mathbf{u}} \rangle$  which are different from zero would violate the requirement that there is no macroscopic polarity in nematics, i.e. the nematic directors  $\hat{\mathbf{n}}$  and  $-\hat{\mathbf{n}}$  are equivalent. That means that to describe orientational order in nematics the next higher, namely second rank tensors have to be considered.

In general, the response  $\mathbf{Y}$  of a system is connected to a field stimulus  $\mathbf{X}$  by

$$Y_\alpha = T_{\alpha\beta} X_\beta \quad (2.44)$$

with  $T_{\alpha\beta} = T_{\beta\alpha}$  being a symmetric tensor [9]. Here  $Y_\alpha$  and  $X_\beta$  are the components of  $\mathbf{X}$  and  $\mathbf{Y}$  parallel with the basis vectors  $\hat{\mathbf{e}}_\alpha$  of a Cartesian coordinate system ( $\alpha, \beta = x, y, z$ ). In this three-dimensional Euclidean space  $T_{\alpha\beta}$  is a Cartesian tensor. For the sake of concreteness we assume that the field  $\mathbf{X}$  is given by a magnetic field  $\mathbf{H}$ . Due to molecular diamagnetism of the liquid-crystal molecules, the response  $\mathbf{Y}$  can be associated with the magnetisation  $\mathbf{M}$ . We can rewrite Eq. (2.44) as

$$M_\alpha = \chi_{\alpha\beta} H_\beta \quad (2.45)$$

where the components of the susceptibility tensor are given by  $\chi_{\alpha\beta}$ . For a static field  $\mathbf{H}$  the tensor  $\chi$  is symmetrical. If the system is isotropic

$$\chi_{\alpha\beta} = \chi \delta_{\alpha\beta} \quad (2.46)$$

where  $\delta_{\alpha\beta}$  is the delta tensor. The components of the delta tensor are defined in all coordinate systems via

$$\delta_{\alpha\beta} = \begin{cases} 0, & \text{if } \alpha \neq \beta \\ 1, & \text{if } \alpha = \beta \end{cases} \quad (2.47)$$

For all symmetric tensors, there is a frame of reference in which the tensor is diagonal. In the diagonal form the non-zero elements are the eigenvalues of the tensor [59]. Thus, a reference frame exists in which the susceptibility tensor is diagonal

$$\boldsymbol{\chi} = \begin{pmatrix} \chi_{\perp} & 0 & 0 \\ 0 & \chi_{\perp} & 0 \\ 0 & 0 & \chi_{\parallel} \end{pmatrix} \quad (2.48)$$

for a uniaxial nematic fluid. Here  $\chi_{\perp} < \chi_{\parallel}$  refer to the perpendicular and parallel component of the magnetic susceptibility, respectively, where arbitrarily the nematic director  $\hat{\mathbf{n}}$  is parallel with  $\hat{\mathbf{e}}_z$ . The nematic director is the axis of rotational symmetry of the phase and is defined mathematically as the eigenvector of  $\boldsymbol{\chi}$  corresponding to the dominant eigenvalue  $\chi_{\parallel}$  (i.e. the eigenvalue with the greatest absolute value). The anisotropy of the system is then given by the difference  $\Delta\chi = \chi_{\parallel} - \chi_{\perp}$  of the susceptibility tensor components. By comparing Eqs. (2.46) and (2.48) one readily concludes that a possible definition of an order parameter is provided by the anisotropic part of the magnetic susceptibility

$$\Delta\chi_{\alpha\beta} = \chi_{\alpha\beta} - \frac{1}{3}\delta_{\alpha\beta} \sum_{\gamma} \chi_{\gamma\gamma} \quad (2.49)$$

with  $\sum_{\gamma} \chi_{\gamma\gamma} = \chi_{\parallel} + 2\chi_{\perp}$  in a uniaxial nematic. Now Eq. (2.49) defines an order parameter tensor which accounts for the isotropic to nematic symmetry change, but order parameters that vanish in the isotropic state and are unity in case of a perfectly aligned system are of particular interest. This prompts us to normalise Eq. (2.49) by the maximum anisotropy  $\Delta\chi_{max}$  which yields the real, symmetric and traceless order tensor

$$Q_{\alpha\beta} = \Delta\chi_{\alpha\beta} / \Delta\chi_{max} \quad (2.50)$$

The choice of the magnetic susceptibility as an example of an order parameter for liquid-crystalline systems was rather arbitrary. The only constraint on the macroscopic observable to serve as a nematic order parameter is that it must reflect the change in symmetry when the transition point is passed. Another suitable description of nematic order is provided by the electric susceptibility tensor  $\varepsilon_{\alpha\beta}$ . The tensor  $\varepsilon_{\alpha\beta}$  relates the electric field  $\mathbf{E}$  to the dielectric polarisation density  $\mathbf{P}$  in a fashion similar to Eq. (2.44). When the electric susceptibility is used as the nematic order parameter it turns out that the bridge from the macroscopic quantity  $\varepsilon_{\alpha\beta}$  to the molecular properties is based on some arbitrary assumptions about the correlation function  $g$  for the dipoles of two

molecules [6]. The correlation function depends on the relative distance as well as on the molecular orientation of the two molecules and has to be taken into account because of the long-range character of the dipolar interaction. On the contrary, the connection of the magnetic susceptibility with molecular properties is well understood [67, 68] since magnetic interactions between individual molecules are negligible [59]. This prompted us to use the magnetic instead of the dielectric susceptibility as a nematic order parameter in the macroscopic picture.

The above defined order tensor  $\mathbf{Q}$  assumes a uniaxial nematic with cylindrical symmetry. A more general form of Eq. (2.50) is given by

$$\mathbf{Q} = \begin{pmatrix} -\frac{1}{2}(Q_1 + Q_2) & 0 & 0 \\ 0 & -\frac{1}{2}(Q_1 - Q_2) & 0 \\ 0 & 0 & Q_1 \end{pmatrix} \quad (2.51)$$

where all eigenvalues  $Q_{xx} \neq Q_{yy} \neq Q_{zz}$  are non-degenerate. In this phase the rotational symmetry about the uniaxial director  $\hat{\mathbf{n}}$  is broken and consequently it is less symmetric. To account for this broken symmetry there is need for a second director  $\hat{\mathbf{m}}$  orthogonal to the uniaxial director  $\hat{\mathbf{n}}$ . For this biaxial state a second order parameter  $Q_2$  has to be considered which measures the amount of order in direction of  $\hat{\mathbf{m}}$ . Note that the general parametrisation in Eq. (2.51) preserves  $\text{Tr}(\mathbf{Q}) = 0$  and reduces to the ideal uniaxial tensor in case of a degenerate eigenvalue  $Q_{xx} = Q_{yy}$ , from which  $Q_2 = 0$  follows directly. The isotropic state is realised by  $Q_1 = Q_2 = 0$ . The reader should be reminded that under certain thermodynamic conditions the biaxial order parameter can be non-zero but small in a uniaxial phase as well. In particular, in the immediate vicinity of a phase transition, where thermal fluctuations become dominant, the ideal uniaxial state is “contaminated” by a small degree of biaxiality as will be shown in Chapter 4.

For the sake of simplicity we have assumed so far that the director  $\hat{\mathbf{n}}$  of the uniaxial nematic is parallel to the unit vector  $\hat{\mathbf{e}}_z$  of a Cartesian coordinate system, i.e.  $\hat{\mathbf{n}} = \hat{\mathbf{e}}_z$ . But this assumption is somewhat artificial because the orientation in space of the director  $\hat{\mathbf{n}}$  is arbitrary in bulk systems with no external fields. This problem can be overcome by expressing the order tensor in a set of basis vectors that coincide with the orthogonal eigenvectors  $\hat{\mathbf{n}}$ ,  $\hat{\mathbf{m}}$  and  $\hat{\mathbf{o}} = \hat{\mathbf{n}} \times \hat{\mathbf{m}}$ . These eigenvectors correspond to the eigenvalues  $Q_1$ ,  $-1/2(Q_1 + Q_2)$  and  $-1/2(Q_1 - Q_2)$ , respectively. This transformation requires, of course, that these eigenvectors are known. After this threefold rotation of the coordinate axes a more general representation of the components of  $\mathbf{Q}$  is given

through [59]

$$Q_{\alpha\beta} = \frac{3}{2}Q_1 \left( n_\alpha \otimes n_\beta - \frac{1}{3}\delta_{\alpha\beta} \right) - \frac{1}{2}Q_2 (m_\alpha \otimes m_\beta - o_\alpha \otimes o_\beta) \quad (2.52)$$

Here, the symbol " $\otimes$ " denotes the dyadic product. Note that the component  $n_\alpha$  is the projection of  $\hat{\mathbf{n}}$  onto the basis vector  $\hat{\mathbf{e}}_\alpha$  of a Cartesian coordinate system. The components  $m_\alpha$  and  $o_\alpha$  are defined by analogy. For later convenience and comparison with the microscopic approach we introduce  $S = \frac{3}{2}Q_1$  as the scalar nematic order parameter such that in case of a uniaxial nematic Eq. (2.52) reduces to

$$Q_{\alpha\beta} = S \left( n_\alpha \otimes n_\beta - \frac{1}{3}\delta_{\alpha\beta} \right) \quad (2.53)$$

At this point it seems worth noticing that from Eq. (2.53) it is only a small step to a definition of a nematic order parameter at the molecular level. The global uniaxial nematic director  $\hat{\mathbf{n}}$  can be interpreted as an average value of the molecular orientations  $\hat{\mathbf{u}}$  and suggests that a microscopic analogue of  $\mathbf{Q}$  may be obtained as an ensemble average in terms of  $\hat{\mathbf{u}}$ . We have postponed this discussion to Section 3.2 because Landau's theory includes only the macroscopic version of an order parameter completely disregarding molecular properties. Therefore it seems worthwhile to first continue with the extension of Landau's theory to the IN transition.

### 2.4.3 Landau-De Gennes Theory

The IN transition is of *first order*, although weak in nature. In a weak *first-order* transition the change in number density  $\Delta\rho/\rho$  as well as the proportional change in entropy  $\Delta\mathcal{S}/\mathcal{S}$  is expected to be small, whereas in a regular *first-order* transition these values exhibit rather pronounced jumps. When the IN transition is passed the molecules arrange their long axes in parallel, i.e. the increase in order is only orientational and not spatial. While the entropy of a system cannot be measured directly, the latent heat linked to  $\Delta\mathcal{S}$  is accessible through the temperature dependence of the heat capacity  $c_P \propto \frac{\partial\mathcal{S}}{\partial T}$ . It can be shown experimentally that the latent heat is small at the IN transition [69].

In the preceding section we showed that nematic order is best described in terms of a second rank tensor  $\mathbf{Q}$ . However, the associated thermodynamic potential  $\mathcal{G}$  in Eq. (2.38) is a scalar and supposed to be invariant under rotations of the system. Then we have to find combinations of the elements  $Q_{\alpha\beta}$  that are invariant under rotation.

These invariants are called “absolute rotational invariants” (ARI) and do not change under rotation of the reference frame of the order tensor [59]. This invariance under rotation indicates that the thermodynamic potential is independent of the reference frame of the order tensor. The ARI can be obtained by multiplication, addition and contraction of all indices of a set of tensors. For a symmetric tensor of second rank it can be shown [59] that these basic invariants can be obtained by contraction. In the unique case of second rank tensors the contraction coincides with the trace  $\text{Tr}(\mathbf{Q}^n)$  of the tensor. In addition,  $\text{Tr}(\mathbf{Q}^n)$  is given by polynomials of  $\text{Tr}(\mathbf{Q})$ ,  $\text{Tr}(\mathbf{Q}^2)$  and  $\text{Tr}(\mathbf{Q}^3)$ . Having identified the ARI, De Gennes suggested an equivalent expression for the Landau potential in the nematic state

$$\mathcal{G} = \mathcal{G}_0 + \frac{1}{2}A\mathbf{Q} : \mathbf{Q} + \frac{1}{3}B\mathbf{Q} : (\mathbf{Q} \cdot \mathbf{Q}) + \frac{1}{4}C(\mathbf{Q} : \mathbf{Q})^2 + \dots \quad (2.54)$$

where we have used the notation of Gray and Gubbins [54]

$$\mathbf{Q} : \mathbf{Q} = Q_{\alpha\beta}Q_{\beta\alpha} = \text{Tr}(\mathbf{Q}^2) \quad (2.55a)$$

$$\mathbf{Q} : (\mathbf{Q} \cdot \mathbf{Q}) = Q_{\alpha\beta}Q_{\beta\gamma}Q_{\gamma\alpha} = \text{Tr}(\mathbf{Q}^3) \quad (2.55b)$$

for single and double contraction of second-rank tensors. In Eq. (2.54)  $\mathcal{G}_0$  is the Landau potential of the isotropic state and we have already excluded the linear term because of  $\text{Tr}(\mathbf{Q}) = 0$ . This permits a stable isotropic state in the absence of any external orienting field. The coefficients  $A(P, T)$ ,  $B(P, T)$  and  $C(P, T)$  in Eq. (2.54) are again functions of  $P$  and  $T$ . We have introduced the prefactors for later convenience.

For the explicit form of the general nematic order tensor given in Eq. (2.51) it is a simple matter to verify that the second- and third-order invariants given in the Eqs. (2.55) reduce to

$$\mathbf{Q} : \mathbf{Q} = \frac{3S^2 + Q_2^2}{2} \quad (2.56a)$$

$$\mathbf{Q} : (\mathbf{Q} \cdot \mathbf{Q}) = \frac{3S(S^2 - Q_2^2)}{4} \quad (2.56b)$$

Employing Eqs. (2.56) in case of a uniaxial phase ( $Q_2 = 0$ ) permits one to rewrite the Landau potential as

$$\mathcal{G} = \mathcal{G}_0 + \frac{3}{4}AS^2 + \frac{1}{4}BS^3 + \frac{9}{16}CS^4 + \dots \quad (2.57)$$

which is now an expansion in the scalar nematic order parameter  $S$  defined on the interval  $[0, 1]$ .

In thermodynamic equilibrium, the IN transition is close to  $A = 0$ . Again assuming isothermal conditions and that the pressure  $P$  is the field driving the transition, the first coefficient is defined by  $A = a(P_{IN} - P)$  with  $a = (\partial A / \partial P)_{P_{IN}} > 0$  and  $P_{IN}$  the IN transition pressure. From the constraint that  $\mathcal{G}$  exhibits a minimum around a finite  $S$  again  $C > 0$  follows. The coefficient  $B$  is expected to be small and negative.

Experimentally the coefficients  $A(P)$ ,  $B(P)$  and  $C(P)$  can be determined by measuring the nematic order parameter, the temperature and the latent heat at the IN transition point. For detailed line of arguments see Vertogen [9]. Here we restrict ourselves to the determination of the coefficients in computer simulations. In principle,  $A(P)$ ,  $B(P)$ , and  $C(P)$  may be obtained from the order parameter distribution  $\mathcal{P}(S)$  because Eq. (2.37) can be rewritten as [52]

$$\mathcal{P}(S) = \mathcal{P}_0 \exp[-\beta \mathcal{G}'(S)] \quad (2.58)$$

where the normalisation constant  $\mathcal{P}_0$  is determined such that

$$\int_0^1 dS \mathcal{P}(S) = 1 \quad (2.59)$$

according to the discussion in Chapter 1, Section 5.6.3 in Ref. 70. Having calculated  $\mathcal{P}(S)$  as a histogram, we obtain the coefficients by fitting a polynomial in  $S$  to  $\ln \mathcal{P}(S)$ . However, in computer simulations we deal with systems of finite size in which the nematic order parameter is non-vanishing in the isotropic state, i.e.  $S$  exhibits a residual value  $S_{res}$ . On that account, to achieve a reasonable fit we have to replace  $S \rightarrow S - S_{res}$  in Eq. (2.57) and treat the residual nematic order parameter  $S_{res}$  as an additional fit parameter. In practise it turns out that histogram data can be fitted very well by the expansion of  $\mathcal{G}$  even to the symmetric bimodal structure at the transition point. Although the fit works quite well, the accuracy of numerical values of the coefficients depends strongly on the statistical accuracy with which the histogram  $\mathcal{P}(s)$  has been obtained. The statistics on  $A(P)$  are quite good and it is supposed to change sign at  $P_{IN}$ . However, as was noted by Eppenga and Frenkel [52],  $B(P)$  and  $C(P)$  are determined mostly by the ‘‘wings’’ of the distribution  $\mathcal{P}(S)$  which can only be determined with limited accuracy. That means that the interpretation of the numerical values of  $B(P)$  and  $C(P)$  is not easy.

### *Validity of Landau-De Gennes Theory*

Let us close this section with some remarks on the validity of the Landau-De Gennes theory which is doubtlessly a mean-field approach. In the Landau-De Gennes theory the order of the state is described by a macroscopic order parameter which assumes the system to be homogeneous. However, due to thermal fluctuations spatial variations of the order parameter occur and the local value oscillates about its mean value. The characteristic length of these correlations is the correlation length  $\ell$  which is a measure of the range of the correlation function. Far from the transition point,  $\ell$  is of the order of the molecular length.

As suggested by Ginzburg [71], the validity of the mean-field approach is then estimated by determining the fluctuations around the extreme values  $S_{IN} = 0$  and  $S_{IN} \neq 0$  of Eq. (2.57). The Ginzburg criterion for the IN transition is given by [72]

$$b\ell^3 \gg k_B T \quad (2.60)$$

Here  $b$  is the height of the barrier separating the low-order state and high-order state at the transition point (see Fig. 2.5). As long as Eq. (2.60) is fulfilled, thermally activated fluctuations between the low-order and high-order state are very unlikely and Landau's theory is expected to be valid. If, on the other hand,  $b\ell^3 \approx k_B T$  the thermal fluctuations can no longer be neglected and the assumption of homogeneity is no longer true. As a consequence, fluctuations of the order parameter have to be taken into account. This is done by including an additional term in Eq. (2.57) that incorporates the spatial correlations of the order parameter. However, this approach is not used in this work. For further discussion, see the review of Gramsbergen *et al.* [59] and references therein.



# Model and Methods

## 3.1 Monte Carlo Simulations

Fast computers have become increasingly important in the field of statistical physics because of their ever-expanding computational power (e.g. see Wood in [73]). Over the years, methods have been developed to solve problems in statistical physics numerically which are applicable over a wide range of time and length scales. However, to describe systems on a nano- or even mesoscale simplified models have to be considered because of the restrictions on computer time. In atomistic simulations, particles are assumed to consist of molecules and obey the laws of classical statistical mechanics, disregarding any quantum corrections. For a summary of computer simulation methods and their range of application see the perspective paper of Gubbins and Moore [74] and references therein.

### *3.1.1 Metropolis Algorithm*

The two most commonly atomistic simulation methods used to solve numerically high-dimensional integrals of the form given in Eq. (2.17) are molecular dynamics and Monte Carlo simulations. In a molecular dynamics simulation the system evolves in a Newtonian phase space for a given force field. Because this approach introduces a physically meaningful time scale it is possible to study dynamic phenomena such as diffusion. In contrast, in the Monte Carlo method particles are moved by means of random numbers stochastically to perform a random walk in configuration space. We will follow Schoen and Klapp [43] to explain the Monte Carlo method in more detail.

The ensemble average of an observable  $\langle \mathcal{O} \rangle$  is defined in any ensemble by integrals

of the form

$$\langle \mathcal{O} \rangle = \int \mathcal{O}(\mathbf{X}) p(\mathbf{X}; \mathbf{Y}) d\mathbf{X} \quad (3.1)$$

where the probability density is a function of the configuration  $\mathbf{X}$  and of the implicitly fixed variables  $\mathbf{Y}$  of the ensemble (compare the expressions given in Eqs. (2.34) and (2.35) for the isostress-isostrain ensemble). In the Monte Carlo method we assume that configuration space can be discretised and  $M$  is the finite number of state points. This permits to rewrite the ensemble average in Eq. (3.1) as

$$\langle \mathcal{O} \rangle = \sum_{i=1}^M \mathcal{O}_i(\mathbf{X}) p_i(\mathbf{X}; \mathbf{Y}) \quad (3.2)$$

where  $\mathcal{O}_i(\mathbf{X})$  denotes the instantaneous value of the observable and  $p_i(\mathbf{X}; \mathbf{Y})$  the probability density of state  $i$ . However, if the states are generated by a random walk one is confronted with two problems. This approach would require  $M \rightarrow \infty$ , but in view of finite simulation time the number of sampled states has to be limited to a maximum value  $M = M_{max}$ . The second problem is that according to Eq. (3.2)  $\mathcal{O}_i(\mathbf{X})$  has to be multiplied by the statistical weight  $p_i(\mathbf{X}; \mathbf{Y})$  which is *a priori* unknown (because of the unknown partition function, see Eq. (2.35)).

One can modify the random walk so that the states are generated according to their statistical weight, i.e. their *importance*  $p_i(\mathbf{X}; \mathbf{Y})$ . Then the ensemble average is given as the arithmetic mean

$$\langle \mathcal{O} \rangle = \frac{1}{M_{max}} \sum_{i=1}^{M_{max}} \mathcal{O}'_i(\mathbf{X}) \quad (3.3)$$

where the prime is added to indicate that the configuration is created according to its *importance*. The advantage of this method is that a series of “weighted” configurations can be interpreted as a numerical realisation of a Markov chain [75–77]. The Markov process is completely determined by the *relative* transition probability  $\pi_{mn}(m \rightarrow n)$  which is the probability of going from state  $m$  to  $n$ . This also implies that the Markov process is independent of the  $m - 1$  preceding steps. If the system is ergodic a sufficient condition for statistical convergence is that the system does obey *detailed balance* [75, 76, 78]

$$\frac{\pi_{mn}(m \rightarrow n)}{\pi_{nm}(n \rightarrow m)} = \frac{p_n}{p_m} \quad (3.4)$$

i.e. microscopic reversibility is satisfied. The appearance of contributions in the Markov chain depends only on the relative probability that the neighbouring states  $m$  and  $n$  occur in the sequence. An inspection of the Eqs. (3.4) and (2.35) additionally reveals that

obeying *detailed balance* the selection of a neighbouring contribution is independent of the partition function.

In computer simulations the algorithm most commonly used to generate numerically a Markov chain is the Metropolis algorithm [79, 80]. Metropolis originally used the Monte Carlo method in the canonical ensemble, but the algorithm can easily be extended to other ensembles. For this reason an adapted version of the Metropolis algorithm is presented where we additionally assume that the considered particles are elongated to serve as a model of liquid crystals.

### 3.1.2 *Isostress-Isostrain Monte Carlo*

In the Metropolis algorithm for elongated particles the configuration  $(\mathbf{R}_m, \hat{\mathbf{U}}_m)$  of the  $m$ -th contribution to a Markov chain is generated in the isostress-isostrain ensemble according to the probability density defined in Eq. (2.35). One of these particles is chosen at random and its position or orientation is changed by a random amount to give a new configuration  $(\mathbf{R}_n, \hat{\mathbf{U}}_n)$ . According to Eq. (3.4) the new configuration is accepted with the relative probability

$$\frac{p_n}{p_m} = \exp(-\beta\Delta U) \quad (3.5)$$

with  $\Delta U = U_n - U_m$  the difference in total configurational energy of the two configurations  $n$  and  $m$ . In the isostress-isostrain ensemble the volume  $V$  of the system may fluctuate to respond to a thermodynamic stimulus such that additional attempts to change the volume have to be incorporated properly [81, 82]. As a result we refer in this ensemble to a Monte Carlo cycle as a sequence of  $N$  attempted displacements and rotations of randomly selected fluid particles plus one attempted change of volume. We carry out the displacement/rotation and the volume change with a frequency  $N : 1$  because of the need to recalculate all  $N$  pair contributions to the total energy in order to test if a volume change is accepted.

The particle displacements are implemented in such a way that the centre-of-mass position  $\mathbf{r}_{i,m}$  of a random particle  $i$  is displaced in direction of the vector  $\delta\mathbf{r}$  to the new position  $\mathbf{r}_{i,n} = \mathbf{r}_{i,m} + \delta\mathbf{r}$ . The only constraint on this displacement vector is that its endpoint lies in a cube of side length  $2\delta r_{max}$  centred at  $\mathbf{r}_{i,m}$ , i.e. the components of the displacement vector are uniformly distributed on  $\delta r_\alpha \in [-\delta r_{max}, \delta r_{max}]$  with  $\alpha = x, y, z$  the Cartesian coordinate axes of the laboratory fixed coordinate system. The rotation of the particles can be implemented on the basis of various algorithms.

We have decided to use an algorithm proposed by Barker and Watts [75, 83] which chooses one of the laboratory fixed Cartesian coordinate axes  $\hat{\mathbf{e}}_\alpha$  at random and rotates the particle by an angle  $\delta\phi \in [-\delta\phi_{max}, \delta\phi_{max}]$  about  $\hat{\mathbf{e}}_\alpha$  on the surface of a cone. The symmetry axis of the cone coincides with  $\hat{\mathbf{e}}_\alpha$  and the apex is at  $\mathbf{r}_{i,m}$ . Here,  $\delta\phi_{max}$  is the maximum rotation angle. The vector of the new orientation is generated by the equation

$$\hat{\mathbf{u}}_{i,n} = \mathbf{A}_\alpha \hat{\mathbf{u}}_{i,m} \quad (3.6)$$

where explicit expressions for the rotation matrices  $\mathbf{A}_\alpha$  can be found, for example, in Allen [75].

The volume of the displacement cube, i.e. the maximum side length  $\delta r_{max}$ , and the maximum rotation angle  $\delta\phi_{max}$  control the convergence of the Markov chain towards the equilibrium distribution in configuration space. If these parameters are too small the energy difference between the new and old configuration is minimal and therefore nearly all moves are accepted. Moreover, configuration space is sampled slowly and insufficiently. If, on the other hand,  $\delta r_{max}$  and  $\delta\phi_{max}$  are too large nearly all new configurations are rejected, which again results in slow and insufficient sampling of configuration space. On the basis of these considerations the maximum values  $\delta r_{max}$  and  $\delta\phi_{max}$  during the Monte Carlo run were adjusted such that 40 – 60% of all trial displacements and rotations are accepted.

After a particle has been moved or rotated, the new configuration  $n$  is accepted in the Metropolis scheme when  $\Delta U < 0$  from which it follows  $p_n/p_m > 1$ . That means, if the total potential energy of the new state  $n$  is lower the simulation continues in any case from state  $n$ . If  $\Delta U > 0$ , i.e.  $p_n/p_m < 1$ , the configuration  $n$  is accepted with the probability  $p_n/p_m = \exp(-\beta\Delta U)$ . In practise, to decide if a new configuration with higher energy is accepted the Boltzmann factor is compared with a random number  $\xi$  uniformly distributed on  $[0, 1]$ . If  $\xi < \exp(-\beta\Delta U)$  the configuration is accepted and otherwise rejected. This means that a new configuration is accepted according to the probability

$$p_{acc} = \min [1, \exp(-\beta\Delta U)] \quad (3.7)$$

where we have defined  $p_{acc} = \pi_{mn}(m \rightarrow n)$ . If the new configuration  $n$  is rejected, the simulation continues with the old configuration  $m$  such that detailed balance is satisfied.

In order to change the volume of the simulation cell, one would intentionally add the same small amount  $\delta_s \in [-\delta_{s,max}, \delta_{s,max}]$  to all side lengths simultaneously. However, we are interested in liquid crystals confined by plane, parallel walls with constant wall

separation. Therefore we chose to perform the Monte Carlo simulation in an isostress-isostrain ensemble where we fix the wall separation  $s_{z0}$  and change the substrate-fluid interfacial area  $A = s_x s_y$  parallel to the walls. We implement this by adding the same  $\delta_s$  to both side lengths

$$\begin{aligned} s_{x,n} &= s_{x,m} + \delta_s \\ s_{y,n} &= s_{y,m} + \delta_s \end{aligned}$$

such that the new centre-of-mass positions are rescaled according to [43]

$$\tilde{\mathbf{r}}_n = \begin{pmatrix} \tilde{x}_n \\ \tilde{y}_n \\ \tilde{z}_n \end{pmatrix} = \begin{pmatrix} \tilde{x}_m \\ \tilde{y}_m \\ \tilde{z}_m \end{pmatrix} \cdot \begin{pmatrix} s_{x,n}/s_{x,m} \\ s_{y,n}/s_{y,m} \\ 1 \end{pmatrix} \quad (3.9)$$

where we have introduced unit cube coordinates

$$\tilde{\mathbf{r}}_n = \begin{pmatrix} \tilde{x}_n \\ \tilde{y}_n \\ \tilde{z}_n \end{pmatrix} = \begin{pmatrix} x_n/s_{x0} \\ y_n/s_{y0} \\ z_n/s_{z0} \end{pmatrix} \quad (3.10)$$

Vorontsov-Vel'yaminov *et al.* [82] have shown that this coordinate transformation introduces an explicit dependence on the interfacial area  $A$  in the isostress-isostrain ensemble average defined in Eq. (2.34)

$$\begin{aligned} \langle \mathcal{O} \rangle &= \sum_A \iint d\mathbf{R} d\hat{\mathbf{U}} \mathcal{O}(\mathbf{R}, \hat{\mathbf{U}}) p(\mathbf{R}, \hat{\mathbf{U}}; A) \\ &= s_{z0}^N \sum_A A^N \iint d\tilde{\mathbf{R}} d\hat{\mathbf{U}} \mathcal{O}(\tilde{\mathbf{R}}, \hat{\mathbf{U}}) p(\tilde{\mathbf{R}}, \hat{\mathbf{U}}; A) \\ &= s_{z0}^N \sum_A \iint d\tilde{\mathbf{R}} d\hat{\mathbf{U}} \mathcal{O}(\tilde{\mathbf{R}}, \hat{\mathbf{U}}) p'(\tilde{\mathbf{R}}, \hat{\mathbf{U}}; A) \end{aligned} \quad (3.11)$$

In unit cube coordinates new configurations are generated according to the scaled statistical weight  $p'(\tilde{\mathbf{R}}, \hat{\mathbf{U}}; A) = A^N p(\tilde{\mathbf{R}}, \hat{\mathbf{U}}; A)$  rather than  $p(\mathbf{R}, \hat{\mathbf{U}}; A)$  in unscaled coordinates.

By analogy to Eq. (3.7), the area change is then accepted with the probability

$$p_{acc,V} = \min \left[ 1, \exp \left\{ -\beta(\Delta U - \tau_{\parallel} \Delta A s_{z0}) + N \ln \left( \frac{A_n}{A_m} \right) \right\} \right] \quad (3.12)$$

where  $\tau_{\parallel}$  is the parallel component of the stress tensor. The explicit dependence of Eq. (3.11) on  $A$  leads to an additional logarithmic term in the acceptance probability

in Eq. (3.12) [82]. The difference in energy and interfacial area is  $\Delta U = U(\tilde{\mathbf{R}}_n; A_n) - U(\tilde{\mathbf{R}}_m; A_m)$  and  $\Delta A = A_n - A_m$ , respectively. The area changes are accepted according to a criterion similar to the one already introduced for particle displacements. For reasons given above we adjust  $\delta_s$  such that 40 – 60% of all attempted volume changes are accepted. A detailed description of this algorithm is given in the paper of Schoen [84] to which we refer the interested reader for further discussion.

## 3.2 Microscopic Order Parameter

We have shown in Sec. 3.1.1 that the ensemble averages of an observable  $\mathcal{O}$  can be approximated during a Monte Carlo run via Eq. (3.3). An observable of interest in liquid-crystalline systems is the nematic order parameter which is introduced here.

The preferred parallel alignment in the nematic phase gives rise to orientational long-range correlations which can be measured in experiments as a macroscopic order parameter. This global quantity does not include any information about the constituting particles. On the contrary, in atomistic simulations all information such as positions and orientations of the individual particles are known. This allows us to define a *microscopic* analogue of the nematic order parameter on the basis of molecular orientations which is expected to be a quantitative measure of the degree of parallel alignment of the molecules. A simple model exhibiting a nematic phase consists of rigid rods. An example of such a rod is a spherocylinder, which is a cylinder capped by two hemispheres of the same diameter.

Let us assume that the long axis of the rod is parallel to the unit vector  $\hat{\mathbf{u}}$ . This vector is given in terms of the Euler angles  $\omega = (\phi, \theta)$  in a laboratory fixed frame by Eq. (2.24). Then the probability of finding rods in an element of solid angle  $d\omega = \sin\theta d\theta d\phi$  is given by  $f(\phi, \theta)d\omega$  [6, 9]. For non-polar, uniaxial particles the orientational distribution function  $f(\phi, \theta)$  can be further specialised. Because of the uniaxial symmetry it is independent of the angle  $\phi$ , i.e.  $f = f(\theta)$ . Nematic phases are non-polar in general such that the nematic directors  $\hat{\mathbf{n}} = -\hat{\mathbf{n}}$  are equal. This non-polar symmetry is also reflected in the distribution function where  $f(\theta) = f(\pi - \theta)$ .

The task of finding the full function  $f(\theta)$  can be simplified by calculating instead the individual moments of its multipole expansion [6, 9, 52]. The individual moments are represented by the coefficients of a series expansion in Legendre polynomials

$$f(\theta) = \sum_{n=0}^{\infty} \frac{2n+1}{2} a_n P_n(\cos\theta) \quad (3.13)$$

Using the orthogonality relations of the Legendre polynomials, the coefficients are given by

$$a_n \equiv \langle P_n(\cos \theta) \rangle \quad (3.14)$$

Because of its trivial form, the moment  $P_0$  is not considered to serve as an order parameter. The dipole moment

$$a_1 \equiv \langle P_1(\cos \theta) \rangle = \int f(\theta) \cos \theta d\theta = \langle \hat{\mathbf{u}} \cdot \hat{\mathbf{n}} \rangle \quad (3.15)$$

is the lowest non-trivial moment in this expansion but it has to vanish due to the non-polarity of the nematic phase. The next higher moment, the quadrupole,

$$a_2 \equiv \langle P_2(\cos \theta) \rangle = \int f(\theta) \frac{1}{2} (3 \cos^2 \theta - 1) d\theta = \frac{1}{2} \langle 3(\hat{\mathbf{u}} \cdot \hat{\mathbf{n}})^2 - 1 \rangle \quad (3.16)$$

is the first to give non-trivial results. The nematic order parameter is then defined as  $\tilde{S} = \langle P_2(\cos \theta) \rangle$  and can, in principle, be calculated in a computer simulation via

$$\tilde{S} = \frac{1}{N} \left\langle \sum_{i=1}^N \left( \frac{3}{2} (\hat{\mathbf{u}}_i \cdot \hat{\mathbf{n}})^2 - \frac{1}{2} \right) \right\rangle \quad (3.17)$$

Here  $\hat{\mathbf{u}}_i$  is the orientation of particle  $i$ ,  $N$  the total number of particles in the system, and angular brackets denote ensemble averages. In a perfectly ordered system ( $\hat{\mathbf{u}}_i \parallel \hat{\mathbf{n}}$ ) the nematic order parameter  $\tilde{S}$  is unity by definition whereas  $\tilde{S}$  vanishes in the isotropic phase. If all molecular orientations are orthogonal to the director ( $\hat{\mathbf{u}}_i \perp \hat{\mathbf{n}}$ ) the nematic order parameter exhibits the value  $\tilde{S} = -\frac{1}{2}$ . If no external field is applied the nematic director  $\hat{\mathbf{n}}$  is *a priori* unknown such that  $\tilde{S}$  cannot be calculated via Eq. (3.17) immediately. However, Eppenga and Frenkel suggest [8, 52] that Eq. (3.17) can be rewritten

$$\begin{aligned} \tilde{S} &= \frac{1}{N} \left\langle \sum_{i=1}^N \left( \frac{3}{2} (\hat{\mathbf{u}}_i \cdot \hat{\mathbf{n}})^2 - \frac{1}{2} \right) \right\rangle \\ &= \frac{1}{N} \sum_{i=1}^N \left\langle \hat{\mathbf{n}} \cdot \left( \frac{3}{2} \hat{\mathbf{u}}_i \otimes \hat{\mathbf{u}}_i - \frac{1}{2} \mathbb{1} \right) \cdot \hat{\mathbf{n}} \right\rangle \\ &= \frac{1}{N} \sum_{i=1}^N \langle \hat{\mathbf{n}} \cdot \mathbf{Q}_i \cdot \hat{\mathbf{n}} \rangle \end{aligned} \quad (3.18)$$

with respect to an arbitrary nematic director. The symbol " $\otimes$ " denotes the dyadic product and  $\mathbb{1}$  the unit tensor. Eq. (3.18) defines the traceless, symmetric second rank

tensor

$$\mathbf{Q} = \frac{1}{N} \sum_{i=1}^N \mathbf{Q}_i = \frac{1}{N} \sum_{i=1}^N \left( \frac{3}{2} \hat{\mathbf{u}}_i \otimes \hat{\mathbf{u}}_i - \frac{1}{2} \mathbf{1} \right) \quad (3.19)$$

which can be diagonalised numerically. If  $\mathbf{Q}$  is in its diagonal form, the only non-zero entries are the three eigenvalues  $\lambda_+ > \lambda_0 > \lambda_-$ . The nematic order parameter may then be obtained as an ensemble average of the largest eigenvalue  $S = \langle \lambda_+ \rangle$  and the corresponding eigenvector is the nematic director  $\hat{\mathbf{n}}$ . By definition,  $S$  is always positive.

Because in computer simulations one is confronted with a finite number of particles  $N$  it seems worthwhile studying the scaling behaviour of the individual eigenvalues. This is because the middle eigenvalue  $S = \langle -2\lambda_0 \rangle$  could be used as an alternative definition of the order parameter. This follows because  $\mathbf{Q}$  is a traceless tensor such that for  $N \rightarrow \infty$  the largest and middle eigenvalue of an uniaxial system are connected via  $\lambda_+ = -2\lambda_0$ . Eppenga and Frenkel show [52] that in the isotropic state the residual values of these eigenvalues are of the order  $\lambda_+ = \mathcal{O}(1/N^{1/2})$  and  $\lambda_0 = \mathcal{O}(1/N)$ , i.e.  $\lambda_0$  approaches zero much faster for increasing particle numbers. However, because we are interested in a quantitative measure of the alignment in the nematic phase the scaling behaviour in this state is of primary importance. In the nematic phase, the two eigenvalues scale as

$$\lambda_+ = S + \mathcal{O}\left(\frac{1}{N}\right) \quad (3.20)$$

$$\lambda_0 = -\frac{S}{2} + \mathcal{O}\left(\frac{1}{\sqrt{N}}\right) \quad (3.21)$$

from which it is obvious that  $\lambda_+$  is the better estimate for  $S$ .

### 3.3 Finite-Size Scaling

In systems of finite size the profiles of the order parameter and of response functions, such as susceptibilities, when plotted as a function of the driving field may be smeared or rounded. This smearing may hamper the determination of the location and nature of the transition. In other words, the transition will be distorted by finite size effects which makes a classification difficult. The influence of the smearing scales with the system size and shrinks smoothly as the size of the system increases. However, in atomistic computer simulations, it is not possible to realise the thermodynamic limit in which the transitions appear in their “natural” form. To circumvent the restrictions

imposed by finite system size, methods like finite-size scaling [85–88] can be used to approximate the phase transition in the thermodynamic limit.

### 3.3.1 Critical Exponents and Scaling Functions

#### *Critical Exponents*

For a *continuous* transition the correlation length  $\ell$  is expected to diverge at the transition point. Close to the transition [58, 89]

$$\ell \propto |\epsilon|^{-\nu} \quad (3.22)$$

with  $\nu$  the critical exponent governing the divergence of the correlation length  $\ell$  at the critical point. Here  $\epsilon$  quantifies the “distance” from the transition point. Assuming that the thermodynamic field  $\Upsilon$  is driving the transition,  $\epsilon = (\Upsilon - \Upsilon_c)/\Upsilon_c$  with  $\Upsilon_c$  the critical value. Due to its divergence, the correlation length  $\ell$  is the characteristic length close to the critical point [88]. A second characteristic length is the linear dimension  $L$  which defines the boundaries of a finite system. It therefore seems reasonable that the ratio  $L/\ell$  controls finite size effects which appear when  $\ell \approx L$ . We will assume in the following that hyperscaling [87] is valid.

#### *Scaling Functions*

Based on these assumptions, so-called scaling functions (which are in fact functions of the ratio  $L/\ell$ ) are defined to account for the finiteness of the system. Close to the critical point the free energy of an infinite system can be separated into a “regular” and a “singular” contribution [90]. In finite-size scaling theory, the “singular” part of the free energy for a finite system scales with the linear dimension  $L$  as [88, 91, 92]

$$F(\Upsilon, L) = L^{-(2-\alpha)/\nu} \mathcal{F}(\Upsilon, L/\ell) \quad (3.23)$$

with  $\mathcal{F}(\Upsilon, L/\ell)$  the scaling function of the free energy. Here, the critical exponents  $\alpha$  and  $\nu$  assume their values at the thermodynamic limit.

According to Eq. (3.22) close to the transition point an observable of an infinite system scales as

$$\mathcal{O} \propto |\epsilon|^y \quad (3.24)$$

with  $y$  the critical exponent of the observable. Since we are interested in the scaling of an order parameter, in Eq. (3.24)  $y = \beta$  with  $\beta$  the critical exponent of the order

parameter. In systems of finite size, however, the order parameter can be described by finite-size scaling through

$$\mathcal{O}(\Upsilon, L) = L^{\beta/\nu} \mathcal{X}(\Upsilon, L/\ell) \quad (3.25)$$

The scaling function  $\mathcal{X}$  associated to the order parameter  $\mathcal{O}$  is a unique function and by analogy with Eq. (3.23) depends on the thermodynamic field  $\Upsilon$  driving the phase transition and on the ratio  $L/\ell$ . In fact, the finite-size scaling of the free energy suggests that appropriate differentiation of Eq. (3.23) yields scaled expressions of the form of Eq. (3.25) for bulk properties of additional response functions. For large systems  $L/\ell \rightarrow \infty$  and  $|\epsilon| \ll 1$  the scaling function  $\mathcal{X}(\Upsilon, L/\ell \rightarrow \infty) \rightarrow (L/\ell)^{-\beta/\nu}$ . Consequently the dependence on  $L$  cancels out such that it is straightforward to show [92] that Eq. (3.25) asymptotically reproduces the critical behaviour of the infinite system

$$\mathcal{O}(\Upsilon, L) \propto \ell^{\beta/\nu} \quad (3.26)$$

It is then plausible that in computer simulation  $L \gg \ell$ . In contrast, directly at the critical point, the correlation length diverges  $L/\ell = 0$  such that the scaling function  $\mathcal{X}(\Upsilon, L/\ell)$  reduces to a proportionality constant [77, 88] and the bulk properties exhibit power law behaviour in  $L$

$$\mathcal{O}(\Upsilon, L) \propto L^{\beta/\nu} \quad (3.27)$$

Assuming that the location of the transition is known, Eq. (3.27) can be used to estimate the ratio of the critical exponents  $\beta/\nu$  from which the universality class of the transition can be concluded. Eq. (3.27) reduces to a constant for vanishing critical exponent, i.e.  $\mathcal{O}$  is in this case independent of the system size  $L$ . That means that for different  $L$  the profiles of  $\mathcal{O}$  intersect at  $\Upsilon_c$  in a single point which is by definition the transition point in the thermodynamic limit. Due to their definition as appropriate ratios of moments of order parameter or energy the cumulants  $g_n$  introduced by Binder [62] are examples of observables with vanishing critical coefficients. Hence, computing  $g_n$  directly at the critical point causes curves for different  $L$  to intersect in a single, non-universal (i.e. model-dependent) point [77, 93].

### 3.3.2 Cumulants

Focusing on cumulants of the order-parameter, the  $n$ -th order cumulant is defined as the ratio of the moments of a general order parameter  $\mathcal{O}$  (e.g.  $\mathcal{O} = S$  for the isotropic-

nematic transition)

$$g_n \equiv \frac{\langle \mathcal{O}^n \rangle}{\langle \mathcal{O} \rangle^n} \quad (3.28)$$

where the moments are defined by

$$\langle \mathcal{O}^n \rangle = \int_0^1 d\mathcal{O} \mathcal{O}^n \mathcal{P}(\mathcal{O}) \quad (3.29)$$

and  $\mathcal{P}(\mathcal{O})$  is the order-parameter distribution. In many applications,  $g_4$  has been considered (e.g. see Refs. 77, 94). However, from the definition of  $g_n$  in Eq. (3.28) and the expression in Eq. (3.29) it is apparent that the ‘‘wings’’ of  $\mathcal{P}(\mathcal{O})$  have stronger weight as  $n$  becomes larger. Unfortunately, the numerical accuracy of the histogram of  $\mathcal{P}(\mathcal{O})$  decreases rapidly as one moves into these wings where  $\mathcal{P}(\mathcal{O}) \rightarrow 0$ . To circumvent this problem, Deutsch [95] proposed employing lower-order cumulants such as  $g_2$  which have better statistics than  $g_4$ . Due to the increased statistics the quantitative values of  $g_2$  seem to be more accurate compared to  $g_4$ . For order parameters which are symmetric around  $\mathcal{O} = 0$  the average of the absolute value  $\langle |\mathcal{O}| \rangle$  has to be used in the denominator, because of  $\langle \mathcal{O} \rangle = 0$ . A comparison of  $g_4$  and  $g_2$  is given by Weber *et al.* [89], who show that both cumulants lead to consistent results as far as the isotropic-nematic phase transition in lyotropic liquid crystals is concerned.

### *Order of Transition through Cumulant Analysis*

The order of a transition can be identified by the different properties of the cumulants for *first-order* and *continuous* transitions. A first conclusion on the nature of the transition can be drawn from the intersection of the cumulants for different  $L$ . Assuming that the system size can be varied over a sufficiently large range, the curves  $g_n(L)$  have to intersect at a single point in the case of a *continuous* transition irrespective of  $L$ . If, on the other hand, the transition is of *first-order* but rounded on account of the finite size,  $g_n(L)$  for different  $L$  do not have to intersect at a unique point. Moreover, the intersection point  $\Upsilon_{cr}$  of curves for neighbouring  $L$  converges to the critical value as [93, 96]

$$\|\Upsilon_{cr} - \Upsilon_c\| \propto L^{-2d} \quad (3.30)$$

where  $d$  is the dimensionality of the system. More specifically, a pair of curves for different  $L$  may intersect such that the relative magnitude of  $g_n$  for any two system sizes reverses at the location of the phase transition. The intersection value  $g_n(\Upsilon_{cr})$

may then scale as  $L^{-d}$  as shown by Vollmayr *et al.* for the  $q$ -state Potts model [93]. Additionally, the cumulants  $g_n$  for a *first-order* transition are monotonically increasing functions for small  $L$  [93, 96] but for large values of  $L$  the profiles may exhibit an extremum in the disordered phase. The height of this extremum scales as the volume  $L^d$  and the distance to the critical value as the inverse volume  $L^{-d}$  [89].

Response functions scale in a different way for a *first-order* and a *continuous* transition. Take, for example, the heat capacity. The  $\delta$ -function singularity of an infinite system is rounded in a finite system and scales with the dimensionality  $d$  at a *first-order* phase transition point, i.e. width decreases as  $L^{-d}$  and the maximum value scales as  $L^d$  [97]. This can clearly be distinguished from the scaling behaviour for a *continuous* transition. For this transition the power law singularity in the heat capacity is rounded and shifted proportional to  $\propto L^{1/\nu}$ . The different scaling of the response functions can be understood within the framework of renormalisation group theory. However, since this is beyond the scope of this work see Binder [66] for further discussion of this topic.

# Results

## 4.1 Finite-Size Scaling

### 4.1.1 *Finite-size scaling analysis of isotropic-nematic phase transitions in an anisometric Lennard-Jones fluid*

Manuel Greschek<sup>a</sup> and Martin Schoen<sup>a,b</sup>

<sup>a</sup>Stranski-Laboratorium für Physikalische und Theoretische Chemie, Fakultät für Mathematik und Naturwissenschaften, Technische Universität Berlin, Straße des 17. Juni 135, D-10623 Berlin, Germany

<sup>b</sup>Department of Chemical and Biomolecular Engineering, Engineering Building I, Box 7905, North Carolina State University, 911 Partners Way, Raleigh, North Carolina 27695, USA

published in *Physical Review E* **83**, 011704 (2011)

PHYSICAL REVIEW E **83**, 011704 (2011)

## Finite-size scaling analysis of isotropic-nematic phase transitions in an anisometric Lennard-Jones fluid

Manuel Greschek<sup>1</sup> and Martin Schoen<sup>1,2,\*</sup><sup>1</sup>*Stranski-Laboratorium für Physikalische und Theoretische Chemie, Fakultät für Mathematik und Naturwissenschaften, Technische Universität Berlin, Straße des 17. Juni 135, D-10623 Berlin, Germany*<sup>2</sup>*Department of Chemical and Biomolecular Engineering, Engineering Building I, Box 7905, North Carolina State University, 911 Partners Way, Raleigh, North Carolina 27695, USA*

(Received 15 September 2010; revised manuscript received 4 December 2010; published 21 January 2011)

By means of Monte Carlo simulations in the isothermal-isobaric ensemble, we perform a finite-size scaling analysis of the isotropic-nematic (IN) phase transition. Our model consists of egg-shaped anisometric Lennard-Jones molecules. We employ the cumulant intersection method to locate the pressure  $P^*$  at which the IN phase transition occurs at a given temperature  $T$ . In particular, we focus on second-order cumulants of the largest and middle eigenvalues of the alignment tensor. At fixed  $T$ , cumulants for various system sizes intersect at a unique pressure  $P^*$ . Various known scaling relations for these cumulants are verified numerically. At  $P^*$ , the isobaric heat capacity passes through a maximum value  $c_p^m$ , which depends on the number of molecules  $N$ . This dependency can accurately be described by a power law such that  $\lim_{N \rightarrow \infty} c_p^m(N) \rightarrow \infty$ . For sufficiently large  $N$ , the pressure at which  $c_p^m$  is located shifts only very slightly in agreement with the apparent insensitivity of the cumulant intersection to  $N$ . In addition, we analyze our data in terms of Landau's theory of phase transitions. Our results are consistent with a weakly discontinuous entropy-driven phase transition.

DOI: [10.1103/PhysRevE.83.011704](https://doi.org/10.1103/PhysRevE.83.011704)

PACS number(s): 64.70.M-, 05.10.Ln, 05.20.Jj, 64.60.an

### I. INTRODUCTION

In the theory of thermal many-particle systems, today it is almost commonplace that any transition between different phases in these systems is affected by the actual size of the system under study. In fact, quite some time ago, it has been realized that thermodynamics, as the fundamental theory to treat thermal systems quantitatively, is significantly altered if it deals with small systems of finite size [1]. In statistical physics, on the other hand, conclusions are usually drawn on the basis of the explicit or implicit assumption that the so-called thermodynamic limit  $N/V = \text{const}$ ,  $N, V \rightarrow \infty$  ( $N$  number of molecules,  $V$  volume) exists and that it can be reached. In particular, our treatment of transformations between different phases of thermal systems often invokes the assumption of the thermodynamic limit. This poses a serious problem to the study of such phase transitions in computer simulations where one is inevitably restricted to finite systems, which typically contain less than  $\sim 10^6$  particles in most practical state-of-the-art applications. In the context of discontinuous phase transitions, perhaps the most prominent signature of finite system size is the rounding of such transitions [2]. Rounding refers to the phenomenon that, in any finite system, the variation of the equilibrium-order parameter with the thermodynamic field across a phase transition can be described by a continuous curve, whereas, in an infinite system, the order parameter would change discontinuously at the onset of the phase transition (see Fig. 4.6 of Ref. [3]).

The importance of system size or, more generally, the presence of specific length scales in studies of phase transitions inspired the development of finite-size scaling concepts quite some time ago [4,5]. Generally speaking, finite-size scaling

aims at a fundamental and quantitative understanding of how certain quantities computed for a finite system will change as one approaches the thermodynamic limit. Finite-size scaling, first applied to continuous phase transitions and critical phenomena, was inspired largely by renormalization group theory [6,7], a theoretical concept that first came into being in quantum electrodynamics [8]. In the meantime, overwhelming literature on the topic exists that can hardly be reviewed and summarized comprehensively in a research paper, such as the present one. Instead, for more information, the interested reader is referred to a—likely incomplete and certainly personal—selection of textbooks and review papers that have been published over the years [3,9–17].

However, to illustrate the power of finite-size scaling as a theoretical concept, it seems worthwhile to give examples of physical systems to which it has been applied successfully. Among these systems lattice models such as the Ising [4,5,18] or Potts model [19–21] rank prominently. As far as continuous model systems are concerned, finite-size scaling has been employed to investigate the gas-liquid phase transition in two- [22,23] and three-dimensional Lennard-Jones fluids [24,25]. In addition, Potoff and Panagiotopoulos also considered binary Lennard-Jones mixtures [25]. Even quantum fluids, such as the three-dimensional weakly interacting Bose gas, have been discussed within the framework of finite-size scaling [26].

In the context of this paper, finite-size scaling will be applied to the isotropic-nematic (IN) phase transition in liquid-crystalline materials. Here, finite-size scaling has been employed to obtain the critical temperature as well as various critical exponents of the planar Lebwohl-Lasher model [27]. Jayasri *et al.* used concepts of finite-size scaling within Wang-Landau Monte Carlo simulations of the three-dimensional Lebwohl-Lasher model [28]. Focusing on the IN phase transition, these authors considered the system-size dependence of the nematic order parameter  $S$ . With increasing

\*martin.schoen@tu-berlin.de

lattice size,  $S$  turns out to have lower values in the isotropic phase and a steeper increase with temperature  $T$  in the immediate vicinity of the transition point. The transition itself is located via Binder's fourth-order cumulant from which it is inferred that the IN phase transition is a discontinuous one. Finite-size effects at the IN phase transition have also been investigated by Fish and Vink [29] again within the Lebwohl-Lasher model. They employ Wang-Landau Monte Carlo simulations and demonstrate that, at discontinuous IN phase transitions, the scaling is approximately that expected for a  $q$ -state Potts model. In a later publication, the same authors investigated the crossover from discontinuous to continuous IN phase transitions in confinement [30]. A careful and very detailed finite-size scaling study of the IN phase transition in nanoconfinement has been published very recently by Almaraz *et al.* who based their work on the Maier-Saupe hard-sphere fluid [31]. López *et al.* used Monte Carlo simulations to study a two-dimensional lattice model of monomers that polymerize reversibly into chains [32]. Employing Binder's fourth-order cumulant, it is observed that the IN phase transition for monodisperse rods without self-assembly is of the same universality class as that of the two-dimensional Ising model; on the contrary, the model pertains to the universality class of the  $q = 1$  Potts model if self-assembly is taken into account. Vink and Schilling consider the interface between isotropic and nematic phases in a system of soft spherocylinders [33]. They apply finite-size scaling concepts to obtain accurate values for the interfacial tension. However, of particular relevance to the present paper is a paper by Weber *et al.* who studied the IN phase transition in a three-dimensional bond-fluctuation lattice model of semiflexible polymers [34]. This work is of central importance for our own study because Weber *et al.* discussed, very carefully, how the IN phase transition can be located through Binder's cumulant intersection technique and, more importantly, which cumulant was most suitable for this purpose. Moreover, as we will emphasize later, their lattice model behaves qualitatively very similarly to the continuous model on which our paper is based.

In our paper, we focus on a simple model of a liquid crystal suggested originally by Hess and Su [35]. It consists of a Lennard-Jones potential in which the attractive contribution has been modified to represent the orientation-dependent interaction between slightly elongated molecules. The charm of the Hess-Su model is its simplicity. Thus, in a computer simulation, it is relatively easy to implement this model in a numerically efficient way. Despite this simplicity, the model exhibits isotropic, nematic, and smectic phases characteristic of a typical liquid crystal [36,37]. Also, the model has recently been used successfully to investigate the impact of certain anchoring scenarios at solid surfaces on the IN phase transition in nanoconfined liquid crystals [38,39]. Unfortunately, the nature of this transition is still unknown for the Hess-Su model even in the bulk. For example, the variation of the nematic-order parameter around the IN phase transition turned out to be smooth and free of hysteresis for relatively large systems of 1000–2000 molecules [36–38]. This prompted us to *speculate* [38] that, for this particular model, the IN phase transition *may perhaps* be continuous. In fact, continuous IN phase transitions are observed in two dimensions [40–42]. However, as we also emphasize in Ref. [38], a finite-size

scaling analysis would be required to prove or disprove this speculation. Therefore, and in view of the usefulness of the Hess-Su model in computer simulations of both bulk and confined liquid crystals [36–39], a careful study of the mechanism of the IN phase transition seems both worthwhile and a bit overdue. Thus, the present paper is devoted to a finite-size scaling analysis of the IN phase transition in the Hess-Su model.

We have organized the remainder of this paper as follows. In Sec. II, we introduce our model system. Some basic concepts of its statistical mechanical treatment and a summary of key quantities, on which our work is based, are introduced in Sec. III. Our results are presented in Sec. IV and will be discussed further in the concluding Sec. V.

## II. THE MODEL SYSTEM

We consider a bulk liquid crystal composed of  $N$  molecules interacting with each other in a pairwise additive fashion such that the configurational potential energy is given by

$$U(\mathbf{R}, \widehat{\mathbf{U}}) = \frac{1}{2} \sum_{i=1}^N \sum_{j \neq i}^N u(\mathbf{r}_{ij}, \widehat{\mathbf{u}}_i, \widehat{\mathbf{u}}_j), \quad (2.1)$$

where  $\mathbf{r}_{ij} \equiv \mathbf{r}_i - \mathbf{r}_j$  is the distance vector between the centers of mass of particles  $i$  and  $j$ . In Eq. (2.1),  $\mathbf{R} \equiv \{\mathbf{r}_1, \mathbf{r}_2, \dots, \mathbf{r}_N\}$  and  $\widehat{\mathbf{U}} \equiv \{\widehat{\mathbf{u}}_1, \widehat{\mathbf{u}}_2, \dots, \widehat{\mathbf{u}}_N\}$  are shorthand notations for the sets of center-of-mass coordinates and unit vectors specifying the orientations of the liquid-crystalline molecules, respectively. Following earlier work [35–38], we adopt the intermolecular interaction potential,

$$u(\mathbf{r}_{ij}, \widehat{\mathbf{u}}_i, \widehat{\mathbf{u}}_j) = 4\varepsilon \left[ \left( \frac{\sigma}{r_{ij}} \right)^{12} - \left( \frac{\sigma}{r_{ij}} \right)^6 \{1 + \Psi(\widehat{\mathbf{r}}_{ij}, \widehat{\mathbf{u}}_i, \widehat{\mathbf{u}}_j)\} \right], \quad (2.2)$$

where  $r = |\mathbf{r}|$  and  $\widehat{\mathbf{r}} = \mathbf{r}/r$ . Hence,  $u$  is a Lennard-Jones potential where the attractive contribution is modified to account for different relative orientations of a pair of molecules. In Eq. (2.2),  $\sigma$  denotes the diameter of a spherical reference molecule, and  $\varepsilon$  is the depth of the attractive well in that reference model. The anisotropy of the fluid-fluid interaction is accounted for by the function,

$$\Psi(\widehat{\mathbf{r}}_{ij}, \widehat{\mathbf{u}}_i, \widehat{\mathbf{u}}_j) = 5\varepsilon_1 P_2(\widehat{\mathbf{u}}_i \cdot \widehat{\mathbf{u}}_j) + 5\varepsilon_2 [P_2(\widehat{\mathbf{u}}_i \cdot \widehat{\mathbf{r}}_{ij}) + P_2(\widehat{\mathbf{u}}_j \cdot \widehat{\mathbf{r}}_{ij})], \quad (2.3)$$

which one obtains from a summation of certain Wigner matrices selected to preserve the head-tail symmetry of the molecules [35]. In other words,  $\Psi$  remains unaltered if  $\widehat{\mathbf{u}}_i$  and/or  $\widehat{\mathbf{u}}_j$  are replaced by  $-\widehat{\mathbf{u}}_i$  and/or  $-\widehat{\mathbf{u}}_j$ . As in our previous paper, we take  $\varepsilon_1 = 0.04$  and  $\varepsilon_2 = -0.08$  for the anisotropy parameters such that the aspect ratio of each molecule is  $\sim 1.26$  (see Fig. 1) [38]. In Eq. (2.3),

$$P_2(x) = \frac{1}{2}(3x^2 - 1) \quad (2.4)$$

is the second Legendre polynomial.

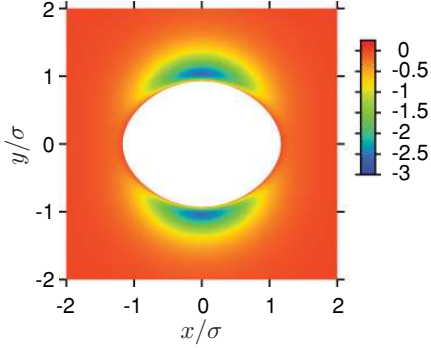


FIG. 1. (Color online) Plots of  $u(r_{12}, \hat{u}_1, \hat{u}_2)$  for a pair of molecules located in the  $x$ - $y$  plane such that  $\mathbf{r}_{12} = (x_{12}, y_{12}, 0)$  and  $\hat{\mathbf{u}}_1 \cdot \hat{\mathbf{u}}_2 = 1$ . The white area at the center of the plot is defined by the condition  $u_{ff}(\mathbf{r}_{12}, \hat{\mathbf{u}}_1, \hat{\mathbf{u}}_2) \geq 0$  such that it approximately represents the shape of the molecule at the center of the coordinate system true to scale. In colored parts of the figure,  $u_{ff}(\mathbf{r}_{12}, \hat{\mathbf{u}}_1, \hat{\mathbf{u}}_2) < 0$  where the color (see attached color bar) indicates the local value  $u_{ff}$  of in units of  $\epsilon$ .

### III. THEORETICAL BACKGROUND

#### A. Statistical thermodynamics

For reasons to be explained later (see Sec. IV A), we choose to describe the thermodynamic state of the liquid crystal in terms of  $N$ , temperature  $T$ , and pressure  $P$  as natural variables. This immediately suggests the Gibbs potential  $\mathcal{G}$  as the relevant thermodynamic potential, which assumes a minimum at equilibrium. One of the quantities we are interested in is the isobaric heat capacity, which can be derived from the exact differential of  $\mathcal{G}$  via

$$\frac{c'_p}{T} \equiv \left( \frac{\partial \mathcal{S}}{\partial T} \right)_{\{\cdot\} \setminus T} = - \left( \frac{\partial^2 \mathcal{G}}{\partial T^2} \right)_{\{\cdot\} \setminus T}, \quad (3.1)$$

where  $\mathcal{S}$  denotes entropy and  $\{\cdot\} \setminus x$  is a shorthand notation to indicate that, upon differentiation, the set of natural variables of  $\mathcal{G}$  is to be held constant except for variable  $x$ . In this paper, we consider the *specific* heat capacity  $c_p = c'_p/N$ .

The connection to a molecular level of description is provided through another textbook expression (see, for example, Chap. 3.29 of Ref. [43]), namely,

$$\mathcal{G} = -k_B T \ln \chi(N, P, T), \quad (3.2)$$

where  $k_B$  is the Boltzmann constant,

$$\chi = \sum_V \exp(-\beta PV) \mathcal{Q}(N, V, T) \quad (3.3)$$

is the partition function in the isothermal-isobaric ensemble,  $V$  denotes volume, and  $\beta \equiv 1/k_B T$ . In Eq. (3.3),  $\mathcal{Q}$  is the canonical ensemble partition function in the classical limit. As explained for arbitrary molecular symmetry in the book by Gray and Gubbins [44] and later for the special case of linear molecules by Gruhn and Schoen [45], one may express  $\mathcal{Q}$  as

$$\mathcal{Q} = \frac{1}{\Lambda^{3N}} \left( \frac{I}{m} \right)^N \mathcal{Z}, \quad (3.4)$$

where

$$\mathcal{Z} = \frac{1}{2^N N!} \int d\mathbf{R} d\hat{\mathbf{U}} \exp(-\beta U) \quad (3.5)$$

is the configuration integral. In Eq. (3.4),  $\Lambda \equiv h/\sqrt{2\pi m k_B T}$  is the thermal de Broglie wavelength ( $h$  is the Planck constant), and  $m$  and  $I$  denote molecular mass and moment of inertia, respectively. The factor  $1/2^N$  in Eq. (3.5) corrects for double counting equivalent configurations characterized by  $\hat{\mathbf{u}}_i$  and  $-\hat{\mathbf{u}}_i$  (head-tail symmetry).

#### B. Properties

From quantities introduced in Sec. III A, we can derive molecular expressions for  $c_p$ . Details of this derivation can be found elsewhere [38]. After considerable but straightforward algebra, one eventually obtains

$$c_p = \frac{5}{2} k_B + \frac{\langle \mathcal{H}^2 \rangle - \langle \mathcal{H} \rangle^2}{N k_B T^2}, \quad (3.6)$$

where  $\langle \dots \rangle$  denotes an ensemble average in the isothermal-isobaric ensemble. In Eq. (3.6), the energy function  $\mathcal{H} \equiv U(\mathbf{R}, \hat{\mathbf{U}}) + PV$  such that  $\frac{5}{2} k_B T + \langle \mathcal{H} \rangle$  can be interpreted as the enthalpy of the liquid crystal. At a phase transition,  $c_p$  undergoes a characteristic change [46] and, therefore, is a useful quantity in the context of this paper.

Moreover, the IN phase transition is characterized by a change in orientational order. To determine the degree of orientational order, we follow Maier and Saupe and introduce the nematic-order parameter  $S$  [47,48] (see also Refs. [49,50]). This order parameter is defined such that  $S = 0$  in an infinitely large isotropic phase, whereas  $S \simeq 1$  if the symmetry axes of all molecules point in the direction of the unit vector  $\hat{\mathbf{n}}$  usually referred to as the director. Because  $\hat{\mathbf{n}}$  is *a priori* unknown, a derivation of a molecular expression for  $S$  conveniently departs from the so-called alignment tensor [51],

$$\mathbf{Q} \equiv \frac{1}{2N} \sum_{i=1}^N (3\hat{\mathbf{u}}_i \otimes \hat{\mathbf{u}}_i - \mathbf{1}), \quad (3.7)$$

where  $\otimes$  denotes the direct (i.e., dyadic) product and  $\mathbf{1}$  is the unit tensor. The alignment tensor can be represented by a real symmetric traceless  $3 \times 3$  matrix that can be diagonalized numerically using Jacobi's method (see, for example, Chap. 11.1 of Ref. [52]). This procedure allows one to compute the three eigenvalues  $\lambda_- < \lambda_0 < \lambda_+$  of  $\mathbf{Q}$  and the associated eigenvectors. Following previous workers [34,38,53,54], we define the nematic-order parameter through the expression  $S \equiv \langle \lambda_+ \rangle$  and take, as  $\hat{\mathbf{n}}$ , the eigenvector associated with the largest *instantaneous* eigenvalue  $\lambda_+$ . Hence,  $\hat{\mathbf{n}}$  may vary during the course of the simulation. Moreover, a basic theorem of linear algebra establishes the trace of a tensor as one of its scalar invariants (see, for example, Chap. 4.2 of Ref. [55]). Therefore,  $\text{Tr} \mathbf{Q} = \text{Tr}(\text{diag} \mathbf{Q}) = 0$  where the operator  $\text{Tr}$  represents the trace and

$$\text{diag} \mathbf{Q} \equiv \begin{pmatrix} -\lambda_+/2 - \zeta & 0 & 0 \\ 0 & -\lambda_+/2 + \zeta & 0 \\ 0 & 0 & \lambda_+ \end{pmatrix}, \quad (3.8)$$

in the basis of eigenvectors of  $\mathbf{Q}$ . In Eq. (3.8),  $\zeta$  may be taken as a measure of apparent biaxiality. This expression was derived by Low who uses an expansion in terms of Wigner matrices [56]. As already pointed out by Eppenga and Frenkel [54],  $\zeta$  is nonzero in any finite system even in the isotropic phase (see also Sec. IV B). Because such finite-size effects are the focus of the present paper, it is useful to introduce the ostensible biaxiality-order parameter  $\xi \equiv \langle \zeta \rangle$  in accord with the definition of  $S$  introduced before.

In the study of finite-size effects at phase transitions, order-parameter *distributions* and their moments have been established as powerful tools [3]. In particular, suitably defined *ratios* of these moments known as cumulants are particularly useful [4,5]. For a nonvanishing order parameter  $\langle O \rangle$ , the  $n$ th-order cumulant may be defined as

$$g_n \equiv \frac{\langle O^n \rangle}{\langle O \rangle^n}, \quad (3.9)$$

where

$$\langle O^n \rangle = \int_0^1 d\tilde{O} \tilde{O}^n \mathcal{P}(\tilde{O}), \quad (3.10)$$

and  $\mathcal{P}(O)$  is the order-parameter distribution, which can be computed as a histogram of  $O$  in a computer simulation. In many applications,  $g_4$  has been considered (see, for example, Refs. [3,12]). However, from the definition of  $g_n$  in Eq. (3.9) and the expression in Eq. (3.10), it is apparent that the wings of  $\mathcal{P}(O)$  are probed more the larger  $n$  becomes. Unfortunately, the accuracy of numerically determined histograms  $\mathcal{P}(O)$  decreases rapidly as one moves into these wings where  $\mathcal{P}(O) \rightarrow 0$ . To circumvent this problem, Weber *et al.* proposed to employ lower-order cumulants, such as  $g_2$  [34]. We follow this proposition in Sec. IV C and, in particular, investigate  $g_2$  for  $O = -\lambda_0 = -\lambda_+/2 + \zeta$  and  $O = \lambda_+$  as the relevant order parameters.

It has also been argued by Weber *et al.* [34] that, at a continuous phase transition,

$$\langle O^n(\cdot, L) \rangle = L^{n\beta/\nu} \mathcal{X}(\cdot, L/\ell), \quad (3.11)$$

where  $L$  is the linear dimension of the system,  $\beta$  is the order-parameter critical exponent,  $\nu$  is the critical exponent governing the divergence of the correlation length  $\ell$  at the critical point, and  $\mathcal{X}$  is a scaling function depending on the thermodynamic field driving the phase transition (represented by  $\cdot$ ) and on the ratio  $L/\ell$ . Directly at the critical point,  $\ell \rightarrow \infty$ . Hence, in computing  $g_n$  directly at the critical point causes curves for different  $L$  to intersect in a single nonuniversal (i.e., model-dependent) point [3,20]. If, on the other hand, the phase transition is discontinuous but rounded on account of the finite size of the system under study,  $g_n$  for different  $L$  do not have to intersect in a single point. Specifically, a pair of curves for different  $L$  may intersect such that the relative magnitude of  $g_n$  for any two system sizes reverses at the location of the phase transition. The intersection may still be system-size dependent and may then scale as  $L^{-d}$  ( $N^{-d/3}$ ) where  $d$  is the dimension of the system as shown by Vollmayr *et al.* for the  $q$ -state Potts model [20]. This prediction was confirmed later by Weber *et al.* for their lattice model of flexible polymers [34]. However, it seems worthwhile to note at this point that the shift of the cumulant intersection may already be very weak over a range

of (sufficiently large) system sizes and, therefore, hard, if not impossible, to detect, although the phase transition is truly discontinuous.

For a discussion of the nature of the IN transition (i.e., whether it constitutes a continuous or a discontinuous phase transition for the present model), it will turn out to be prudent to determine the correlation length  $\ell$  of orientational correlations. To that end, it is useful to introduce the orientation correlation function,

$$G_2(r) = \langle P_2[\cos \alpha(r)] \rangle, \quad (3.12)$$

where  $\cos \alpha(r) = \hat{\mathbf{u}}_1(\mathbf{r}_1) \cdot \hat{\mathbf{u}}_2(\mathbf{r}_2)$  is the cosine of the angle  $\alpha(r)$  formed between the molecular directors  $\hat{\mathbf{u}}_1$  and  $\hat{\mathbf{u}}_2$  of a pair of molecules separated by a distance  $r = |\mathbf{r}_1 - \mathbf{r}_2|$  (see, for example, Ref. [57]). The subsequent discussion will particularly benefit from introducing the so-called *connected* correlation function,

$$G_2^c(r) \equiv G_2(r) - S^2 \xrightarrow{r \rightarrow \infty} 0. \quad (3.13)$$

Assuming an exponential decay of  $G_2(r)$  in a sufficiently large system [27,58], one may obtain a quantitative estimate of  $\ell$  by fitting  $f(r) = a \exp(-r/\ell)$  to  $G_2^c(r)$  in the limit of sufficiently large  $r$  taking  $a$  and  $\ell$  as fit parameters.

## IV. RESULTS

### A. Numerical aspects

To compute the quantities introduced in Sec. III B, we employ Monte Carlo simulations in the isothermal-isobaric ensemble in which a fluid composed of a fixed number of molecules  $N$  is exposed to a pressure  $P$  that remains constant during the course of an individual simulation. Consequently, the volume  $V$  of the simulation cell may fluctuate. We employ periodic boundary conditions in all three spatial directions. To generate a Markov chain of configurations in this ensemble, we utilize the algorithm described in Sec. 4.1 of Ref. [59]. As part of this algorithm attempts to change the volume of the simulation, cells have to be incorporated properly. In the simulation of ordered (nematic or smectic) phases of anisometric molecules, one would normally want to change the lengths of the simulation cell independently in each spatial direction such that these ordered phases can be accommodated properly. This is particularly important in the formation of smectic phases of molecules with a large aspect ratio. If, for example, the length of the simulation cell in the direction of the smectic layers would not be close to an integer multiple of the thickness of a smectic layer, the entire fluid would be under an artificial and unphysical stress because the smectic phase could not fit properly into the simulation cell. For the present model in which the molecules have a rather small aspect ratio of  $\sim 1.26$  and because we are not interested in smectic phases, this problem does not arise. We have verified this by monitoring diagonal components of the pressure tensor  $\mathbf{P} = P\mathbf{1}$  separately during the course of the simulation [38]. Thus, we assume our simulation cell to be roughly cubic throughout this paper and change the volume of the simulation cell isotropically, that is, simultaneously and by the same small amount  $\delta_s$  in each spatial direction. We adjust  $\delta_s$ , which is typically of the order of only a few percent of  $\sigma$  [see Eq. (2.2)], during the course

of a simulation to achieve an acceptance ratio of 40%–60% of all attempted changes of simulation-cell volume.

We refer to a Monte Carlo cycle as a sequence of  $N$  attempted displacements or rotations of sequentially selected fluid particles plus one attempted change of  $V$ . Rotations and displacements are attempted with equal probability. Most runs comprise initial  $5 \times 10^4$  Monte Carlo cycles for equilibration followed by  $2 \times 10^5$  Monte Carlo cycles; for the largest systems with  $N = 5000$  and  $10000$ , and, in the immediate vicinity of such a transformation, the length of a typical run was enlarged up to  $4 \times 10^5$  Monte Carlo cycles to guarantee sufficient statistical accuracy.

We express all quantities of interest in terms of the customary dimensionless (i.e., reduced) units. For example, length is given in units of  $\sigma$ , energy in units of  $\varepsilon$ , and temperature in units of  $\varepsilon/k_B$ . Other derived quantities are expressed in terms of suitable combinations of these basic quantities. For example, pressure is given in units of  $\varepsilon/\sigma^3$ . Throughout this paper, we fix the temperature  $T = 1.0$ , which should be sufficiently low to allow for a formation of both isotropic and nematic phases where we take the mean-field bulk phase diagram of Hess and Su as a rough guidance [35]. To save computer time, we cut off fluid-fluid interactions beyond a separation of  $r_c = 3.0$  between the centers of mass of a pair of fluid molecules with no shift [31] or long-range correction applied. In addition, we employ a combination of a linked-cell and a conventional (Verlet) neighbor list as described in the book by Allen and Tildesley to further speed up the simulations (see Chap. 5.3 of Ref. [60]). This latter list includes all particles as neighbors whose centers of mass are located within a distance of  $r_n = 3.5$  from a reference molecule at the origin of the neighbor sphere. Under these conditions, the smallest system we can study comprises  $N = 250$  molecules. If  $N < 250$ , the actual side lengths of the simulation cell could become shorter than  $2r_c$  such that the minimum image convention [60] would be violated. We could accommodate these smaller systems if we reduce  $r_c$ . However, this would inevitably change the physical nature of our model fluid. A comparison with our earlier papers [38,39] would then be disabled. Consequently, the simulations presented in this paper have been carried out for systems containing  $250 \leq N \leq 5000$  molecules. A few simulations for  $N = 10000$  have also been included to check certain scaling laws. However, these simulations take approximately up to 4 days of CPU time per state point on our computer cluster and, therefore, are too time consuming to be carried out routinely.

Finally, a comment seems appropriate concerning the choice of the isothermal-isobaric ensemble for this paper. Ideally, one would prefer to study phase transitions in the grand canonical ensemble [61]. Unfortunately, the IN phase transition normally arises in a density regime where the Metropolis algorithm adapted to simulations in the grand canonical ensemble is rather inefficient or breaks down completely [60]. The reason is that, during the particle creation or deletion substep of the adapted Metropolis algorithm, it becomes increasingly difficult to either remove existing particles mostly located at energetically favorable positions or to create new ones at energetically favorable holes as the fluid's average density increases. Because  $N$  is fixed in isothermal-isobaric Monte Carlo simulations, this problem does not arise so that

this latter ensemble seems a better choice for the present paper. However, it is noteworthy that finite-size scaling procedures developed originally for the grand canonical ensemble may be transferred to the isothermal-isobaric ensemble without modification as shown by Wilding and Binder a while ago [61].

### B. Finite-size effects

In the context of the IN phase transition, finite-size effects manifest themselves most notably in the nematic-order parameter  $S$  introduced in Sec. III B. As one can see from plots in Fig. 2(a),  $S$  does not vanish at low pressures in the isotropic phase but remains nonzero. Generally speaking,  $S$  increases with  $P$  as one goes from the isotropic ( $P = 1.0$ ) to the nematic phase ( $P = 2.0$ ). Our data show that  $S$ , in the isotropic phase, is larger the smaller  $N$  is. In going from the isotropic to the nematic phase, the overall increase of  $S$  with  $P$  is smaller the smaller  $N$  is. Around the IN phase transition,  $S$  increases more steeply as the number of molecules in the system becomes larger. On the contrary, the dependence of  $S$  on  $N$  in the nematic phase is much smaller. These features, which are relatively easy to understand, already have been reported and have been discussed many times in the literature. They are observed in quite different model systems, such as hard platelets [54], lattice polymers of variable stiffness [34], polydisperse mixtures of soft spherocylinders [53], and even under nanoconfinement conditions [31].

In a typical liquid-crystalline material, the interaction between a pair of mesogens is such that a parallel orientation of both members of the pair is usually favored regardless of whether these interactions are purely entropic or of a van der Waals type. In general, these interactions have a small but nonvanishing range so that the preferred relative orientation of a pair of nearest neighbors is transferred, to some extent, to more distant molecules. Hence, at the molecular level, nanoscopic clusters form in which molecules exhibit nematic order, although the thermodynamic state of the entire liquid crystal pertains to the isotropic phase. On account of thermal fluctuations, sufficiently remote clusters may have local directors pointing in different and uncorrelated directions. In an infinite system, where one would average over a vast (i.e., essentially infinite) number of such clusters, the order parameter would vanish identically according to its definition. In a finite system, however, and no matter how big the system is, some residual order inevitably remains, and this is the reason for the nonvanishing values of  $S$  in the isotropic phase that become smaller as  $N$  increases as one can see from Fig. 2(a).

The finite-size effect also manifests itself as an ostensible biaxiality as can be seen from plots in Fig. 2(b). In an infinite system and according to its definition,  $\xi$  should vanish in the isotropic phase where no preferred orientation of the molecules exists. It should also vanish in a perfect nematic phase of uniaxial symmetry. On the contrary, plots of  $\xi$  versus  $P$  in Fig. 2(b) reveal that, even in the isotropic phase, a substantial biaxiality exists that becomes smaller with increasing  $N$ . As one moves into the nematic regime,  $\xi$  becomes smaller because of the increasing uniaxiality of these phases where  $\hat{n}$  represents the dominant symmetry axis. Our results show that this drop of  $\xi$  may be relatively sharp in large systems (e.g.,  $N = 5000$ ),

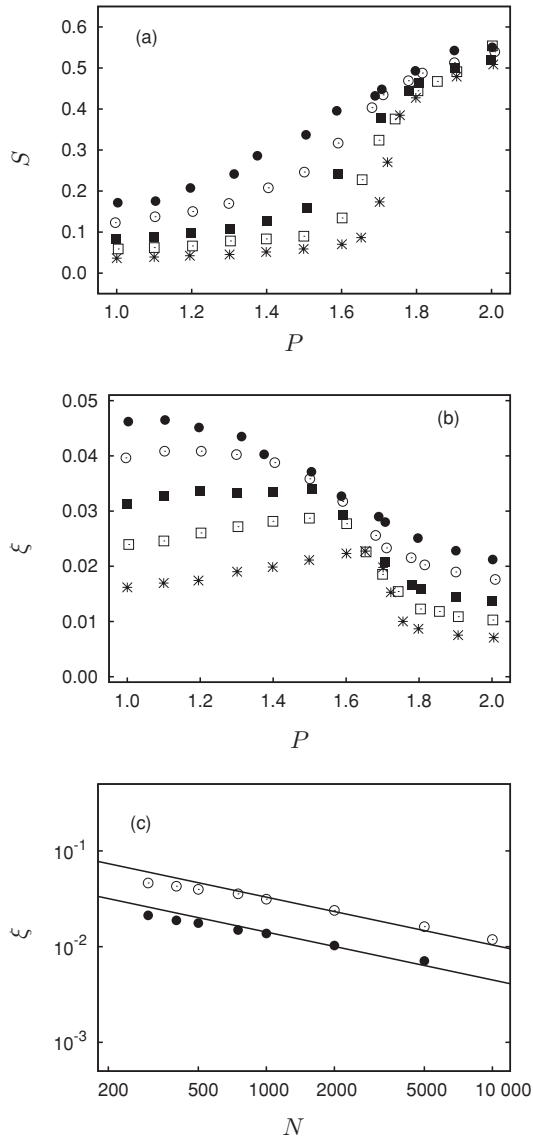


FIG. 2. (a) Nematic-order parameter  $S$  as function of applied pressure  $P$ ;  $\bullet$ ,  $N = 300$ ;  $\circ$ ,  $N = 500$ ;  $\blacksquare$ ,  $N = 1000$ ;  $\square$ ,  $N = 2000$ ; and  $*$ ,  $N = 5000$ . (b) as (a) but for the biaxial order parameter  $\xi$ . (c)  $\xi$  as a function of  $N$  for  $\circ$ ,  $P = 1.0$  in the isotropic and  $\bullet$ ,  $P = 2.0$  in the nematic phases; solid lines are fits of  $aN^{-1/2}$  to the discrete data points where  $\circ$ ,  $a = 1.042$  and  $\bullet$ ,  $a = 0.449$ , respectively (see Sec. IV C).

whereas, in smaller systems (e.g.,  $N = 300$ ), the variation of  $\xi$  with  $P$  is much weaker around the IN phase transition. Nevertheless, a small residual ostensible biaxiality remains even for the largest system and deep in the nematic phase as the plot of  $\xi$  for  $N = 5000$  molecules and  $P = 2.0$  in Fig. 2(b) shows. Moreover, the plot in Fig. 2(c) shows that our data can be very well represented by a power law providing further support for the presence of a perhaps vanishingly small but

always nonzero residual ostensible biaxiality in the nematic phase of any finite system. The power law decay of  $\xi$  will be rationalized later in Sec. IV C.

### C. Cumulant analysis

Because of the finite-size effects demonstrated in Sec. IV B, it is not immediately obvious at which pressure  $P$  the IN phase transition occurs in the thermodynamic limit nor what the nature (i.e., continuous versus discontinuous) of this phase transition is for the present model. For example, as Fig. 2(a) already indicated, the variation of  $S$  around the (assumed) phase transition becomes steeper with increasing  $N$  but still looks rather continuous, which would point toward a continuous phase transition. However, one knows that, in any finite system, phase transitions appear to be more or less rounded depending on the specific phase transition and the actual system size [3]. Hence, for the present model, even the system comprising  $N = 5000$  molecules may still be too small to reveal the true discontinuous steplike change of  $S$  at a discontinuous IN transition on account of the relative weakness of the transition. The notion that the IN phase transition in the Hess-Su model may be unusually weak is further corroborated by the surprisingly small increase of  $S$  across that transition. For example, it is evident from plots in Fig. 2(a) that  $S$  does not exceed 0.6 even deep in the nematic regime. This value is less than  $\frac{2}{3}$  of the ideal value  $S = 1$  in a nematic phase in which nearly all molecules are perfectly aligned with  $\hat{n}$  [62]. Further evidence for the formation of only weakly ordered nematic phases in the Hess-Su model is provided by the observation that, in our Monte Carlo simulations, the angle increment for the random orientation of molecules is adjusted to a remarkably large value of  $\Delta\alpha \simeq \frac{\pi}{2}$  to preserve an acceptance ratio of roughly 0.5 even deep in the nematic phase at  $P \simeq 2.0$ . This shows that, after the nematic phase has formed, molecules are still relatively free to rotate, thus, explaining the small values of  $S$  and, perhaps, the weakness of the IN phase transition in the Hess-Su model. Consequently, the apparent smoothness of the curves in Fig. 2(a) may erroneously be misinterpreted as a signature of a continuous IN phase transition.

To locate the transition point and to shed more light on the nature of the IN phase transition, it has been demonstrated, quite some time ago, in the pioneering work by Binder [3–5] that cumulants of suitably chosen order parameters are very useful not only in locating the transition point, but also in determining the nature of a specific phase transition. In this paper, we focus on the second-order cumulants  $g_2^0$  and  $g_2^+$  following the suggestion of Weber *et al.* [34], where the superscript refers to the associated eigenvalues  $\lambda_0$  and  $\lambda_+$  of  $\mathbf{Q}$ , respectively. Before turning to a detailed analysis of both cumulants and in view of a similar analysis performed earlier by Weber *et al.* for a lattice model of flexible polymers [34], it seems worthwhile to investigate the scaling behavior of those moments of  $\lambda_0$  and  $\lambda_+$  on which both cumulants are based [see Eq. (3.9)]. In the isotropic phase, one anticipates

$$\langle \lambda_0 \rangle \propto N^{-1}, \quad (4.1a)$$

$$\langle \lambda_0^n \rangle \propto N^{-n/2}, \quad n \geq 2, \quad (4.1b)$$

$$\langle \lambda_+^n \rangle \propto N^{-n/2}. \quad (4.1c)$$

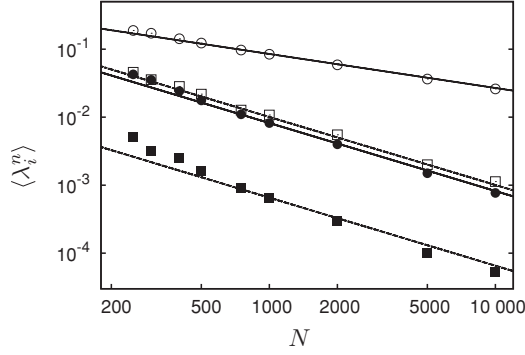


FIG. 3. Moments of the order-parameter distribution  $\mathcal{P}(\lambda_i)$  ( $i = 0, +$ ) [see Eq. (3.10)] as functions of  $N$  for  $P = 1.0$  in the isotropic phase. Results are shown for  $\circ$ ,  $i = +, n = 1$ ;  $\bullet$ ,  $i = +, n = 2$ ;  $\square$ ,  $i = 0, n = 1$ ; and  $\blacksquare$ ,  $i = 0, n = 2$ . Solid and dashed lines represent the various scaling laws given in Eqs. (4.1) (see text).

The scaling laws given in Eqs. (4.1a) and (4.1c) for  $n = 1$  have been obtained analytically by Eppenga and Frenkel [54], whereas the ones given in Eqs. (4.1b) and (4.1c) have been conjectured and numerically confirmed by Weber *et al.* [34].

Plots in Fig. 3 confirm the scaling laws introduced in Eq. (4.1) quite nicely for a range of particle numbers varying by a factor of 40 between the smallest and the largest one considered. In terms of an associated variation of the side length of the (cubic) simulation cell, this translates to a, perhaps, somewhat less impressive factor of only 3.4 if this number is compared with a factor of 32 by which Weber *et al.* have varied the number of lattice sites in one spatial dimension [34]. However, one has to keep in mind that these latter authors employed a (three-dimensional) lattice model, which—like most, if not all lattice models—is computationally much less demanding than a continuous model, such as the one studied here. Nevertheless, it is gratifying that even over a smaller range of system sizes, our data already obey the asymptotic behavior predicted by Eqs. (4.1). We have made this test as rigorous as possible by fitting power laws  $aN^{-b}$  to the discrete Monte Carlo data where we only took  $a$  but not  $b$  as a fit parameter; values for  $b$  are taken directly from Eqs. (4.1). This procedure also enables us to detect a small deviation from the scaling laws as far as  $\langle \lambda_0 \rangle$  and  $\langle \lambda_0^2 \rangle$  for  $N < 500$  are concerned. This deviation from the scaling laws indicates that these systems may be a little bit too small for the asymptotic expressions in Eqs. (4.1) to be fully valid. In fact, for insufficiently large  $N$ , there should be correction terms to the asymptotic expressions given in Eqs. (4.1) (see, for example, Eqs. (A12) of Ref. [54]).

Also, we are now in a position to rationalize the scaling behavior of the ostensible biaxiality already displayed in Fig. 2(c). From Eq. (3.8), it follows that

$$\xi \equiv \langle \zeta \rangle = \langle \lambda_+ \rangle \left( \frac{1}{2} + \frac{\langle \lambda_0 \rangle}{\langle \lambda_+ \rangle} \right) \stackrel{N \rightarrow \infty}{\propto} N^{-1/2}, \quad (4.2)$$

where we employed the scaling laws stated in Eqs. (4.1). In the nematic phase, however, Eppenga and Frenkel's analysis

indicates a different scaling behavior of the eigenvalues of  $\mathbf{Q}$ , namely,

$$\langle \lambda_0 \rangle \propto N^{-1/2}, \quad (4.3a)$$

$$\langle \lambda_+ \rangle \propto N^{-1}, \quad (4.3b)$$

such that

$$\xi = \langle \lambda_0 \rangle \left( \frac{1}{2} \frac{\langle \lambda_+ \rangle}{\langle \lambda_0 \rangle} + 1 \right) \stackrel{N \rightarrow \infty}{\propto} N^{-1/2} \quad (4.4)$$

leads to the same scaling behavior of the ostensible biaxiality in both isotropic and nematic phases. Our data plotted in Fig. 2(c) are consistent with both Eqs. (4.2) and (4.4) as far as sufficiently large systems ( $N \gtrsim 500$ ) are concerned. Deviations from the scaling laws in Eqs. (4.2) and (4.4) at smaller particle numbers are anticipated on account of additional  $N$ -dependent corrections that were neglected in our analysis [54]. However, our data do not permit us to verify Eqs. (4.3) directly because, in the nematic phase, the variation of both eigenvalues over the range of system sizes considered is vanishingly small as one can see, for instance, from the plots in Fig. 2(a).

After analyzing these various scaling laws, it follows from Eqs. (4.1) and the plots in Fig. 3 that, in the isotropic phase,  $g_2^+ \approx c$  and  $g_2^0 \propto N$  where  $c$  is a nonuniversal model-specific constant. This scaling behavior of the cumulants makes it somewhat more cumbersome to analyze  $g_2^+$  because curves for different  $N$  bundle up in the isotropic phase as we will demonstrate shortly. A similar bundling up is not expected for  $g_2^0$ , and this is the reason why analyzing this latter cumulant was suggested earlier by Weber *et al.* [34]. However, we will show later that both cumulants provide data sets that are consistent with each other. However, before turning to that discussion, it seems worthwhile to point out that numerical accuracy of  $g_2^0$  in the isotropic phase decreases with increasing  $N$  despite the more favorable scaling behavior. This is because an increasing value of  $g_2^0$  with increasing  $N$  is obtained by taking the ratio of two numbers, both of which tend to zero as  $N \rightarrow \infty$  [see Eqs. (3.9), (4.1a), and (4.1b)]. Therefore, the accuracy of  $g_2^0$  is expected to go down with system size. Focusing on small systems to circumvent this problem is not advisable either because the linear dimension(s) of the simulation cell may eventually become comparable in magnitude with  $\ell$ . In this latter case, one has to be prepared for additional features that render the interpretation of the cumulant difficult [34].

Plots in Fig. 4(a) illustrate the behavior of  $g_2^+$  with  $P$  and for different system sizes. In the isotropic regime, one clearly sees the bundling up of curves for different  $N$  as anticipated. As  $P$  increases,  $g_2^+$  decreases monotonically as far as smaller systems ( $N \leq 500$ ) are concerned. In larger systems,  $g_2^+$  exhibits a nonmonotonic dependence on  $P$  and passes through a maximum located at a system-size-dependent pressure in the isotropic phase [cf., Fig. 2(a)]. The height of this maximum, which is most clearly visible in the plot for  $N = 5000$ , increases with  $N$  similar to what has been observed earlier by Weber *et al.* [34]. Most importantly, however, curves for different  $N$  have a common intersection at the transition pressure  $P^* \simeq 1.74$  and reverse their magnitude for  $P > P^*$ . Comparing Figs. 4(a) and 4(b), one notices a

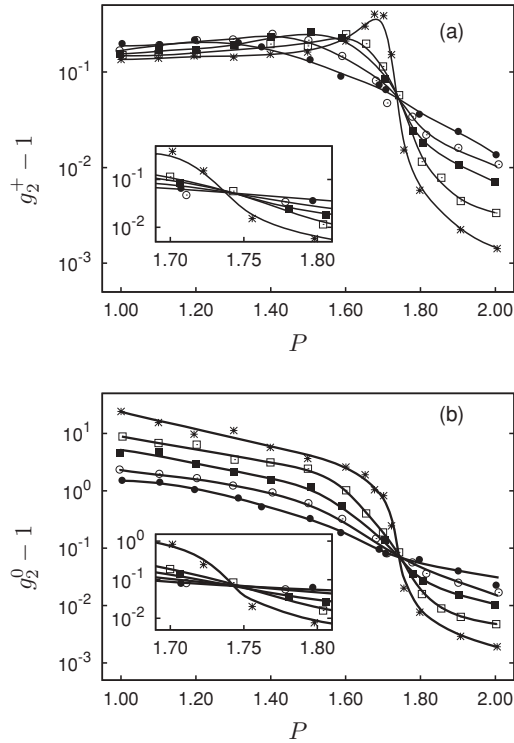


FIG. 4. (a) Second-order cumulant  $g_2^+ - 1$  as a function of applied pressure  $P$ ;  $\bullet$ ,  $N = 300$ ;  $\circ$ ,  $N = 500$ ;  $\blacksquare$ ,  $N = 1000$ ;  $\square$ ,  $N = 2000$ ; and  $*$ ,  $N = 5000$ . (b) as (a) but for  $g_2^0$ . The insets show enlargement of plots around the IN phase transition (see text).

couple of differences. First, as predicted on the basis of Eqs. (4.1a), (4.1b), and Fig. 3, plots of  $g_2^0$  in Fig. 4(b) do not bundle up in the isotropic phase. In fact,  $g_2^0$  at  $P = 1.0$  changes by little more than an order of magnitude over the range  $300 \leq N \leq 5000$  as expected. The pressure dependence of all curves is monotonic. All curves intersect at  $P^* \simeq 1.74$  (as do the curves  $g_2^+$ ), where they change their curvature and reverse their order for  $P > P^*$ . Hence, from plots in both parts of Fig. 4, we conclude that the IN phase transition at  $T = 1.0$  occurs at  $P_{\text{IN}} = P^* \simeq 1.74$ .

#### D. Nature of the isotropic-nematic phase transition

Although this result and the observation of a common cumulant intersection for both  $g_2^+$  and  $g_2^0$  are gratifying, they still leave the question concerning the *nature* of the IN phase transition unanswered. For example, the fact that a common intersection of the second-order cumulants exists is not necessarily indicative of a continuous phase transition as emphasized earlier by Vollmayr *et al.* [20]. On the contrary, a unique cumulant intersection could also mean that the system-size-dependent shift of the intersection characteristic of a discontinuous phase transition is too weak to be detected over the range of system sizes accessible and the statistical accuracy with which  $g_2^+$  and  $g_2^0$  can be computed.

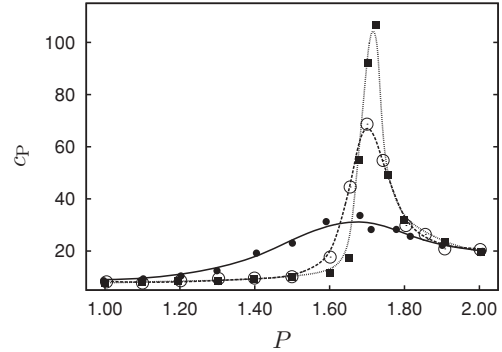


FIG. 5. Isobaric heat capacity  $c_p$  as a function of applied pressure  $P$ ;  $\bullet$ ,  $N = 300$ ;  $\circ$ ,  $N = 2000$ ; and  $\blacksquare$ ,  $N = 5000$ .

To gain more insight into the nature of the IN phase transition, we considered additional quantities in this paper. Plots in Fig. 5 show the variation of the isobaric heat capacity [see Eq. (3.6)] as a function of pressure for three selected system sizes. One notices that sufficiently far away from the maximum, the heat capacity apparently is independent of  $N$ . This holds for low pressures in the isotropic as well as for sufficiently high pressures in the nematic phases. In the vicinity of the phase transition, the shape of  $c_p$  exhibits a marked system-size dependence. Generally speaking, the larger  $N$ , the sharper and taller the maximum  $c_p^m$  of the curve  $c_p$ . For the largest system of  $N = 5000$  molecules considered in Fig. 5, the location of  $c_p^m$  agrees very well with  $P^* \simeq 1.74$  obtained via the cumulant intersection approach and, therefore, is taken as a fingerprint of the IN phase transition as in our previous work [38,39]. One also sees from Fig. 5 that the location of  $c_p^m$  is remarkably insensitive to the system size, whereas, both the width of the curves plotted in Fig. 5 as well as the height of their maximum depend strongly on  $N$ .

According to Vollmayr *et al.*, one expects  $c_p^m$  in a three-dimensional system to scale with  $N^{2/3\nu-1}$  if the IN phase transition is continuous [20]. In this scaling relation,  $\nu = 0.6289$  is the relevant critical exponent [63] such that the divergence of  $c_p^m$  with increasing system size at a continuous phase transition would be rather weak. If, on the other hand, the IN phase transition was discontinuous,  $c_p^m$  should increase linearly with  $N$  [20]. However, in analyzing the scaling behavior of  $c_p^m$ , some care has to be taken. This is because it was pointed out by Bruce and Wilding [64] and reemphasized more recently by Fernandez *et al.* [65] that the scaling law for  $c_p^m$  contains an analytical background that does not scale with system size (see, for example, Eq. (48) of Ref. [65]). As we show in Fig. 6,  $c_p^m$  may be represented by an expression of the form  $aN^y + b$ . Fitting this expression to our data, the analytic background  $b \simeq 8.2$  turns out to be rather substantial and amounts to roughly  $\frac{1}{4}$  of  $c_p^m$  for  $N = 300$ . In addition, our fit gives  $y \simeq 0.58$ , which is much larger than the value  $2/3\nu - 1 \simeq 0.06$  expected for a continuous phase transition. Nevertheless, our value of  $y$  is still smaller than 1, which would be anticipated for a strongly discontinuous IN transition. A scaling behavior intermediate between those characteristics of a continuous and that of a discontinuous phase transition

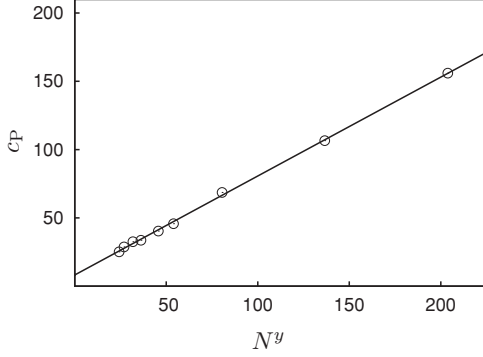


FIG. 6. Maximum of the isobaric heat capacity  $c_p^m$  as a function of the number of molecules  $N^y$  where  $y \simeq 0.58$  is obtained by fitting the expression  $aN^y + b$  to the simulation data.

has been reported earlier by Vollmayr *et al.* for the  $q$ -state Potts model [20]. However, Vollmayr *et al.* did not include the analytical background in their scaling analysis of  $c_p^m$ . Nevertheless, we follow these authors and conclude that, for the Hess-Su model, the IN phase transition is most likely to be weakly discontinuous because our value of  $y$  turns out to be midway between that characteristic of a continuous and that of a strongly discontinuous phase transition.

Further evidence for this conclusion is provided by an inspection of the orientational correlation function  $G_2(r)$  [see Eq. (3.12)] plotted in Fig. 7 for two state points in the immediate vicinity of the IN phase transition at  $P \simeq 1.735$  and 1.745. These values are very close to  $P^* \simeq 1.74$  at which all cumulants  $g_2^0$  and  $g_2^+$  intersect (see Fig. 4). For a large system containing  $N = 10000$  molecules, both curves converge nicely to their asymptotic values  $S^2$  within the range of accessible intermolecular distances. For the state at lower pressure  $P = 1.735$ , the system is still in its isotropic phase ( $S \simeq 0.072$ ); whereas, at the higher pressure  $P = 1.745$ , one has already entered the nematic regime ( $S \simeq 0.343$ ). For  $N = 10000$ , the IN phase transition is already relatively sharp as these numbers indicate. Whereas this already suggests that, in the limit  $N \rightarrow \infty$ , one is probably dealing with a discontinuous rather than a continuous phase transition, plots in Fig. 7(b) provide further evidence for this interpretation. These plots reveal that, over a relatively large range of intermolecular separations  $r$ ,  $G_2^c(r)$  can be described by an exponential function as discussed at the end of Sec. III B. A fit of an exponential function gives  $\ell \simeq 2.13$  at  $P = 1.735$ , whereas an only slightly larger value of  $\ell \simeq 2.33$  is observed at  $P = 1.745$  immediately above the IN phase transition. In other words, across the IN phase transition,  $\ell$  does not exceed two times the length of the long molecular axis. Moreover, directly at the IN phase transition,  $\ell$  remains smaller by a factor of 3 than the length of the computational cell for the smallest system studied ( $N = 300$ ,  $L \simeq 7$ ). From our data, it seems unlikely to expect that  $\ell \rightarrow \infty$  as one would if the IN phase transition were continuous. Similar observations have been made by Weber who found that  $\ell$  passes through a maximum at the IN phase transition but remains small and finite [66].

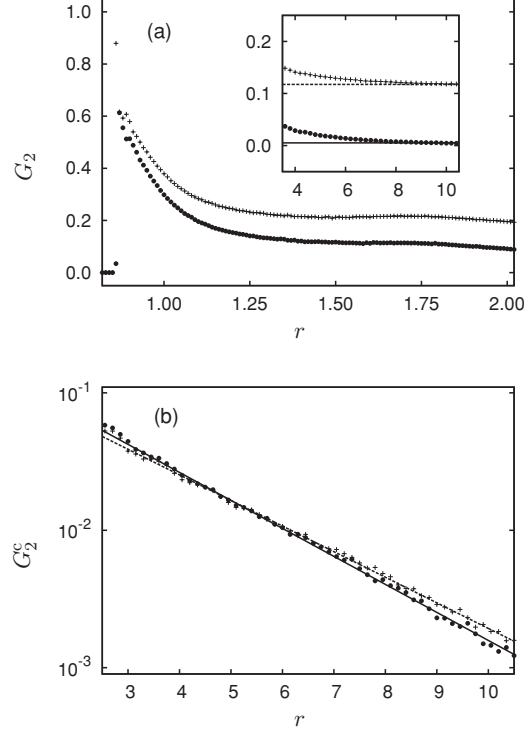


FIG. 7. (a) Orientational correlation function  $G_2(r)$  for  $N = 10000$  and  $\bullet$ ,  $P \simeq 1.735$  and  $+$ ,  $P \simeq 1.745$ . The inset shows long-range behavior of  $G_2(r) \rightarrow S^2$  [—,  $S \simeq 0.072$  and ----,  $S \simeq 0.343$ , see Eq. (3.13)]. (b) as (a) but for  $G_2^c(r)$  on a semilogarithmic scale; lines are fits of an exponential function to the curves for —,  $P \simeq 1.735$  and ----,  $P \simeq 1.745$ .

### E. Predictions of Landau theory

Finally, it seems worthwhile to analyze the IN phase transition in terms of Landau's theory of phase transitions [50]. To that end, one expresses the relevant thermodynamic potential as a Taylor series in terms of the order parameter. In the present case, where the relevant thermodynamic field driving the phase transition is the pressure, we may expand  $\mathcal{G}$  in terms of  $\mathbf{Q}$  as [50]

$$\beta\mathcal{G} = \beta g_0 + \frac{1}{2}A(P)\langle\mathbf{Q}\rangle : \langle\mathbf{Q}\rangle + \frac{1}{3}B(P)\langle\mathbf{Q}\rangle : (\langle\mathbf{Q}\rangle \cdot \langle\mathbf{Q}\rangle) + \frac{1}{4}C(P)(\langle\mathbf{Q}\rangle : \langle\mathbf{Q}\rangle)^2 + \dots, \quad (4.5)$$

where  $A(P)$ ,  $B(P)$ , and  $C(P)$  are dimensionless coefficients depending only on  $P$  under the present isothermal conditions. In Eq. (4.5), we employ the notation of Gray and Gubbins for single and double contractions of the second-rank tensor  $\mathbf{Q}$  [44]. In the uniaxial case ( $\xi = 0$ ) and after diagonalizing  $\mathbf{Q}$  in the basis of its eigenvectors, it follows from Eq. (3.8) that second- and third-order scalar invariants of  $\mathbf{Q}$  are given by

$$\langle\mathbf{Q}\rangle : \langle\mathbf{Q}\rangle = \frac{3}{2}S^2, \quad (4.6a)$$

$$\langle\mathbf{Q}\rangle : (\langle\mathbf{Q}\rangle \cdot \langle\mathbf{Q}\rangle) = \frac{3}{4}S^3, \quad (4.6b)$$

and, therefore, [50],

$$\beta\mathcal{G} = \beta\mathcal{G}_0 + \frac{3}{4}A(P)S^2 + \frac{1}{4}B(P)S^3 + \frac{9}{16}C(P)S^4 + \dots \quad (4.7)$$

Notice that the expansion of  $\beta\mathcal{G}$  starts with the second-order scalar invariant of  $\mathbf{Q}$  as the first nontrivial term because the first-order scalar invariant  $\text{Tr } \mathbf{Q} = 0$  on account of Eq. (3.7). In principle,  $A(P)$ ,  $B(P)$ , and  $C(P)$  may be obtained from  $\mathcal{P}(S)$  because [54]

$$\mathcal{P}(S) = \mathcal{P}_0 \exp[-\beta\mathcal{G}(S)], \quad (4.8)$$

where the normalization constant  $\mathcal{P}_0$  is determined such that

$$\int_0^1 dS \mathcal{P}(S) = 1 \quad (4.9)$$

according to the discussion in Sec. 5.6.3 of Chap. 1 in Ref. [11].

In the simulations, we obtain  $\mathcal{P}(S)$  as a histogram using a width  $\delta S = 0.005$  for the histogram bins. Plots in Fig. 8 reveal that, in the isotropic phase and sufficiently far away from the IN phase transition,  $\mathcal{P}(S)$  exhibits a single maximum. This maximum is larger the smaller  $P$  is. Likewise, the width of  $\mathcal{P}(S)$  increases as  $P$  increases toward  $P^*$ . In the immediate vicinity of the IN phase transition,  $\mathcal{P}(S)$  becomes bimodal where the two peaks of the distribution are not completely separated because our system is still finite. However, we notice that the shape of this bimodal distribution can still be fitted very well with the Landau expansion of  $\beta\mathcal{G}$ . In a sequence of very careful simulations, we have also been able to determine  $\mathcal{P}(S)$  directly at the pressure  $P^* \simeq 1.74$  at which the cumulants  $g_2^0$  and  $g_2^+$  apparently intersect (see Fig. 4). It is particularly gratifying that, at this pressure,  $\mathcal{P}(S)$  is bimodal with two peaks of equal height as the inset in Fig. 8 clearly shows. Hence, in the sense of Eq. (4.8),  $\mathcal{P}(S)$  at  $P^*$  may be interpreted as an order-parameter distribution for coexisting isotropic and nematic phases in a system of finite size.

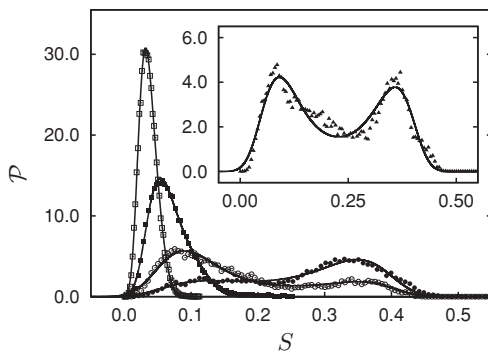


FIG. 8. Order-parameter distribution  $\mathcal{P}(S)$  as a function of the nematic-order parameter  $S$  for  $N = 5000$ ;  $\square$ ,  $P = 1.00$ ;  $\blacksquare$ ,  $P = 1.60$ ;  $\circ$ ,  $P = 1.70$ ; and  $\bullet$ ,  $P = 1.75$ . Full line is a fit based upon  $\mathcal{G}$  from Eq. (4.7) treating  $A(P)$ ,  $B(P)$ , and  $C(P)$  as fit parameters and replacing  $S \rightarrow S - S_{\text{res}}$  where the residual nematic-order parameter  $S_{\text{res}}$  is treated as an additional fit parameter accounting for the nonvanishing nematic order in any finite system [see Fig. 2(a)]. The inset shows  $\mathcal{P}(S)$  directly at  $\blacktriangle$ ,  $P^* \simeq 1.74$  (see also Fig. 4).

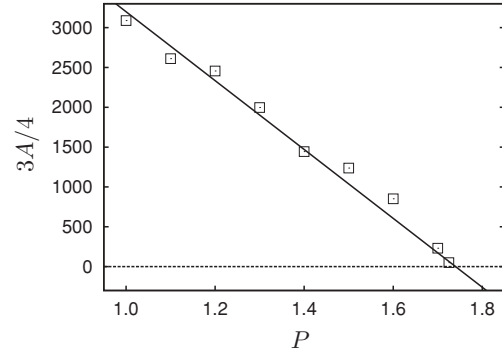


FIG. 9. Plot of  $A(P)$  in the Landau expansion of  $\beta\mathcal{G}$  [see Eq. (4.7)] as a function of pressure  $\square$ ,  $P$ . The solid line is a fit of Eq. (4.10) to the discrete data points taking  $A_0$  as a fit parameter and  $P^* = 1.74$  from the cumulant analysis presented in Sec. IV C.

It is also apparent from the plots in Fig. 8 that  $\mathcal{P}(S)$  is not Gaussian in agreement with the Landau expansion of  $\mathcal{G}$  in Eq. (4.7) if one assumes both  $B(P)$  and  $C(P)$  to be appreciable in magnitude. We obtain information about  $A(P)$ ,  $B(P)$ , and  $C(P)$  by fitting Eqs. (4.7) and (4.8) to the histograms representing  $\mathcal{P}(S)$ . As noted earlier by Eppenga and Frenkel [54],  $B(P)$  and  $C(P)$  are determined mostly by the wings of  $\mathcal{P}(S)$ , which can only be determined with limited accuracy so that we refrain from plotting any data. However, our results seem to suggest that  $B(P)$  decreases toward  $P^*$  but remains small, whereas,  $C(P) > 0$  everywhere. These general features are consistent with requirements of Landau's theory as far as discontinuous phase transitions are concerned (see Sec. 143 of Ref. [46]). At such a transition,  $A(P)$  has to change sign at  $P^*$ . Here, the usual assumption [46] is that, sufficiently close to  $P^*$ ,

$$A(P) = A_0(P - P^*), \quad (4.10)$$

such that  $A(P)$  changes sign at  $P = P^*$ . Results of our fit plotted in Fig. 9 are consistent with this general prediction of Landau's theory, thereby supporting our earlier conclusion that the IN phase transition in the Hess-Su model is likely to be weakly discontinuous.

## V. DISCUSSION AND CONCLUSIONS

In this paper, we employed Monte Carlo simulations in the isothermal-isobaric ensemble to investigate finite-size effects at the IN phase transition in the Hess-Su model of a liquid crystal [35] and to gain a more detailed picture of the nature of this phase transition. In particular, we wished to determine whether this phase transition was continuous or discontinuous. Finite-size effects manifest themselves most directly as nonvanishing values of the nematic-order parameter  $S$  in the isotropic phase. From an operational point of view,  $S$  is usually computed as an ensemble average of a suitably chosen eigenvalue of the alignment tensor  $\mathbf{Q}$ . From the pioneering work by Eppenga and Frenkel, one knows how these ensemble averages should scale with the number of molecules  $N$  both in the isotropic and in the nematic phases and, of course,

irrespective of the specific model system [54]. Later, Weber *et al.* proposed similar scaling laws for higher-order moments of the eigenvalue distributions [34]. All these scaling laws are confirmed numerically in this paper and for the range of system sizes chosen.

Another fingerprint of finite-size effects is an ostensible biaxiality  $\xi$  that is small but does not vanish completely, although the molecules of our model are uniaxial and there are no external fields that would cause nematic phases to have true biaxial symmetry [39]. From the scaling relations for ensemble averages of eigenvalues of  $\mathbf{Q}$ , the system-size dependence of  $\xi$  is given by  $N^{-1/2}$  both in the isotropic and in the nematic phases. Here, this prediction is tested and is confirmed, at least, for sufficiently large system sizes. The detailed investigation of various scaling predictions is important because it allows us to verify that the range of system sizes chosen for this paper is large enough for our model. Moreover, the confirmation of analytically predicted scaling laws indicates that the statistical accuracy of our Monte Carlo results is sufficient to determine both location  $P^*$  and nature of the IN phase transition in the Hess-Su model.

In this regard, the cumulant intersection method originally proposed by Binder [4,5] is particularly useful. Based upon the second-order cumulant of  $\lambda_+$  and  $\lambda_0$  of  $\mathbf{Q}$ , we obtain  $P^* = 1.74$  at the given temperature  $T = 1.00$ . In this regard, it is somewhat striking that our cumulants seem to intersect at a universal pressure  $P^*$  irrespective of system size and seemingly contrary to what one would have anticipated for a discontinuous phase transition. However, following arguments put forth by Vollmayr *et al.* [20], this observation alone is insufficient to conclude that the IN phase transition is, in fact, continuous. In principle, it is conceivable that, at a very weak discontinuous phase transition, one may fail to observe the anticipated shift of the intersection between pairs of cumulants proportional to  $N^{-1}$ . This could happen if, for instance, the constant of proportionality is too small to be detected given the statistical accuracy of the data. In fact, looking at Fig. 8 of Ref. [34], one sees that their system-size-dependent temperature  $T_{cr}(L)$  changes rather weakly with  $L$  for lattices with more than only  $L = 10$  sites.

Therefore, to decide whether the IN phase transition in the present model is continuous or discontinuous, additional information is required. To that end, we compute the orientation correlation function  $G_2(r)$  for a large system with  $N = 10000$  molecules. Around the phase transition,  $G_2^c(r)$  exhibits an exponential decay governed by a correlation length  $\ell$ , which does not exceed twice the long axis of our molecules and, thus, remains finite and small in the immediate vicinity of the IN phase transition. Similar observations have been made earlier by Weber for his lattice model of flexible polymer chains. For example, in his thesis, Weber shows that  $\ell$  remains finite but passes through a weak maximum during the IN phase transition [66]. The finiteness of  $\ell$  clearly points to a discontinuous phase transition. However, if that were the case, one anticipates the maximum of the associated isobaric heat capacity to scale proportional to  $N$ . In the actual simulations, we find an increase of  $c_p^m \propto N^y$  where  $y \simeq 0.58$  is significantly *smaller* than 1. On the other hand,  $y$  is significantly *larger* than  $\frac{2}{3v} - 1 \simeq 0.06$  expected for a continuous phase transition [20]. The scaling of  $c_p^m$ , with an

effective exponent intermediate to that characteristic of a continuous and that of a discontinuous phase transition, parallels results obtained by Vollmayr *et al.* for a thermally driven discontinuous phase transition in a three-dimensional  $q$ -state Potts model ( $q \geq 3$ ). Moreover, we notice that, for particle numbers  $500 \leq N \leq 5000$ , the shift of  $c_p^m$  with  $N$  is surprisingly minute. This seems consistent with the observation that we have been unable to detect any dependence of the intersection between pairs of neighboring cumulants  $g_2^0$  and  $g_2^+$  with  $N$ .

The apparent insensitivity of the location of  $c_p^m$  to changes in  $N$  is particularly gratifying in view of our earlier studies of the IN phase transition in various confined geometries [38,39]. In these works, we located the IN phase transition solely via the position of the maximum of the isobaric heat capacity and only for  $1500 \leq N \leq 2000$  molecules. From our present more extensive investigation, we conclude that, in this range of particle numbers,  $c_p^m$  is a sufficiently accurate indicator to locate the IN phase transition. Nevertheless, it needs to be stressed that the value of  $P^* \simeq 1.70$  first reported by Steuer *et al.* [37] and confirmed later by us [38], which was based upon system sizes of  $N = 1000$  [37] and  $N = 1500$  [38], is presumably a bit too low because of a small residual system-size effect.

Moreover, it is interesting to note that Landau's theory of phase transitions [46] seems qualitatively applicable here similar to what has been concluded by Eppenga and Frenkel [54] for their model liquid crystal of hard platelets. Within this theory, the continuous or discontinuous character of a phase transition depends on whether or not the coefficient  $B$  in front of the third-order term of the expansion of the thermodynamic potential vanishes [46,50]. Although our data do not permit us to distinguish, with absolute certainty, between the two, they seem to suggest that  $B$  is small but nonzero at  $P^*$ . In addition, at the IN phase transition, the symmetric bimodal shape of  $\mathcal{P}(S)$  reveals that the free-energy barrier  $\beta\Delta\mathcal{G}$  separating coexisting isotropic and nematic states (see, for example, the inset in Fig. 8) is only on the order of  $k_B T$ . Therefore, the IN phase transition is most likely to be weakly discontinuous. This notion is corroborated further by the observation that the variation of  $S$  with  $P$  still looks rather smooth even for  $N = 5000$ . Moreover, the pronounced peak in plots of  $c_p$  versus  $P$  indicates a loss of orientational entropy caused by the preferential alignment of molecules with the director  $\hat{n}$  as one goes from the isotropic to the nematic phase [38]. Thus, we conclude that all observations made in this paper are consistent with a weakly discontinuous entropy-driven IN phase transition. Similar conclusions have been reached for the lattice polymer model investigated by Weber *et al.* [34] despite the fact that, in their study, the IN phase transition was thermally driven.

#### ACKNOWLEDGMENTS

We are grateful to Professor Kurt Binder (Johannes-Gutenberg Universität Mainz) and Dr. Pawel Bryk (Uniwersytet Marii-Curie Skłodowskiej) for reading our manuscript and commenting, in detail, on our results. In addition, we are most grateful to an anonymous referee for bringing

Refs. [64,65] to our attention and for very insightful and helpful comments that doubtlessly led to a substantial improvement of our presentation. We are also grateful for financial

support from the International Graduate Research Training Group 1524 “Self-assembled soft-matter nanostructures at interfaces.”

- 
- [1] T. L. Hill, *Thermodynamics of Small Systems* (Dover, Mineola, NY, 2002).
- [2] Y. Imry, *Phys. Rev. B* **21**, 2042 (1980).
- [3] D. P. Landau and K. Binder, *A Guide to Monte Carlo Simulations in Statistical Physics*, 2nd ed. (Cambridge University Press, Cambridge, UK, 2005).
- [4] K. Binder, *Z. Phys. B: Condens. Matter* **43**, 119 (1981).
- [5] K. Binder, *Phys. Rev. Lett.* **47**, 693 (1981).
- [6] K. Wilson, *Phys. Rev. B* **4**, 3174 (1971).
- [7] K. Wilson, *Phys. Rev. B* **4**, 3184 (1971).
- [8] M. Gell-Mann and F. E. Low, *Phys. Rev.* **95**, 1300 (1954).
- [9] K. Binder, *Ann. Rev. Phys. Chem.* **43**, 33 (1992).
- [10] K. Binder, *Computational Methods in Field Theory* (Springer-Verlag, Berlin, 1992), p. 57.
- [11] V. Privman, *Finite Size Scaling and Numerical Simulation of Statistical Systems* (World Scientific, Singapore, 1990).
- [12] K. Binder and D. W. Heermann, *Monte Carlo Simulation in Statistical Physics* (Springer-Verlag, Berlin, 1988).
- [13] J. L. Cardy, *Finite Size Scaling* (North-Holland, Amsterdam, 1988).
- [14] K. Binder, *Ferroelectrics* **73**, 43 (1987).
- [15] M. N. Barber, *Phase Transitions and Critical Phenomena* (Academic, New York, 1983), p. 145.
- [16] H. E. Stanley, *Phase Transitions and Critical Phenomena* (Oxford University Press, Oxford, 1971).
- [17] M. E. Fisher, in *Critical Phenomena*, Proceedings of the 1970 Enrico Fermi International School of Physics (Academic, New York, 1971), p. 1.
- [18] K. Binder and D. P. Landau, *Phys. Rev. B* **30**, 1477 (1984).
- [19] M. S. S. Challa, D. P. Landau, and K. Binder, *Phys. Rev. B* **34**, 1841 (1986).
- [20] K. Vollmayr, J. D. Reger, M. Scheucher, and K. Binder, *Z. Phys. B: Condens. Matter* **91**, 113 (1993).
- [21] R. L. C. Vink, *Phys. Rev. Lett.* **98**, 217801 (2007).
- [22] M. Rovere, D. W. Heermann, and K. Binder, *J. Phys. Condens. Matter* **2**, 7009 (1990).
- [23] A. D. Bruce and N. B. Wilding, *Phys. Rev. Lett.* **68**, 193 (1992).
- [24] N. B. Wilding, *Phys. Rev. E* **52**, 602 (1995).
- [25] J. J. Potoff and A. Z. Panagiotopoulos, *J. Chem. Phys.* **109**, 10914 (1998).
- [26] J.-H. Wang and Y.-L. Ma, *J. Phys. B* **43**, 175301 (2010).
- [27] E. Mondal and S. K. Roy, *Phys. Lett. A* **312**, 397 (2003).
- [28] D. Jayasri, V. S. S. Sastry, and K. P. N. Murthy, *Phys. Rev. E* **72**, 036702 (2005).
- [29] J. M. Fish and R. L. C. Vink, *Phys. Rev. B* **80**, 014107 (2009).
- [30] J. M. Fish and R. L. C. Vink, *Phys. Rev. E* **81**, 021705 (2010).
- [31] N. G. Almaraz, C. Martín, and E. Lomba, *Phys. Rev. E* **80**, 031501 (2009).
- [32] L. G. López, D. H. Linares, and A. J. Ramirez-Pastor, *Phys. Rev. E* **80**, 040105 (2009).
- [33] R. L. C. Vink and T. Schilling, *Phys. Rev. E* **71**, 051716 (2005).
- [34] H. Weber, W. Paul, and K. Binder, *Phys. Rev. E* **59**, 2168 (1999).
- [35] S. Hess and B. Su, *Z. Naturforsch.* **54a**, 559 (1999).
- [36] H. Steuer, S. Hess, and M. Schoen, *Physica A* **328**, 322 (2003).
- [37] H. Steuer, S. Hess, and M. Schoen, *Phys. Rev. E* **69**, 031708 (2004).
- [38] M. Greschke, M. Melle, and M. Schoen, *Soft Matter* **6**, 1898 (2010).
- [39] M. Greschke and M. Schoen, *Soft Matter* **6**, 4931 (2010).
- [40] D. Frenkel and R. Eppenga, *Phys. Rev. A* **31**, 1776 (1985).
- [41] H. Kunz and G. Zumbach, *Phys. Rev. B* **46**, 662 (1992).
- [42] M. A. Bates and D. Frenkel, *J. Chem. Phys.* **112**, 10034 (2010).
- [43] D. A. McQuarrie, *Statistical Mechanics* (Harper & Row, New York, 1976).
- [44] C. G. Gray and K. E. Gubbins, *Theory of Molecular Fluids* (Clarendon, Oxford, 1984), Vol. 1.
- [45] T. Gruhn and M. Schoen, *Phys. Rev. E* **55**, 2861 (1997).
- [46] L. D. Landau and E. M. Lifschitz, *Lehrbuch der Theoretischen Physik* (Akademie Verlag, Berlin, 1987), Vol. V.
- [47] W. Maier and A. Saupe, *Z. Naturforsch. A* **14**, 882 (1959).
- [48] W. Maier and A. Saupe, *Z. Naturforsch. A* **15**, 287 (1960).
- [49] G. Vertogen and W. H. de Jeu, *Thermotropic Liquid Crystals, Fundamentals* (Springer-Verlag, Berlin, 1988).
- [50] P. G. de Gennes and J. Prost, *The Physics of Liquid Crystals* (Clarendon, Oxford, 1995).
- [51] I. Pardowitz and S. Hess, *Physica A* **100**, 540 (1980).
- [52] W. H. Press, S. A. Teukolsky, W. T. Vetterling, and B. P. Flannery, *Numerical Recipes in FORTRAN* (Cambridge University Press, Cambridge, UK, 1989).
- [53] A. Richter and T. Gruhn, *J. Chem. Phys.* **125**, 064908 (2006).
- [54] R. Eppenga and D. Frenkel, *Mol. Phys.* **52**, 1303 (1984).
- [55] G. Arfken, *Mathematical Methods for Physicists* (Academic, San Diego, 1985).
- [56] R. Low, *Eur. J. Phys.* **23**, 111 (2002).
- [57] C. Zannoni, *The Molecular Physics of Liquid Crystals* (Academic, London, 1979), Chap. 3, p. 76.
- [58] R. V. Gavai, F. Karsch, and B. Peterson, *Nucl. Phys. B* **322**, 738 (1989).
- [59] M. Schoen, *Physica A* **270**, 353 (1999).
- [60] M. Allen and D. Tildesley, *Computer Simulation of Liquids* (Oxford Science Publications, Oxford, 1986).
- [61] N. B. Wilding and K. Binder, *Physica A* **231**, 439 (1996).
- [62] M. G. Mazza, M. Greschke, R. Valiullin, J. Kärger, and M. Schoen, *Phys. Rev. Lett.* **105**, 227802 (2010).
- [63] A. M. Ferrenberg and D. P. Landau, *Phys. Rev. B* **44**, 5081 (1991).
- [64] A. D. Bruce and N. B. Wilding, *Phys. Rev. E* **60**, 3748 (1999).
- [65] L. A. Fernandez, A. Gordillo-Guerrero, V. Martin-Mayor, and J. J. Ruiz-Lorenzo, *Phys. Rev. E* **80**, 051105 (2009).
- [66] H. Weber, Ph.D. thesis, Johannes-Gutenberg Universität Mainz, 1997 (unpublished).

## 4.2 Homogeneous Slit-Pore

### 4.2.1 *Isotropic-nematic phase transitions in confined mesogenic fluids. The role of substrate anchoring*

Manuel Greschek<sup>a</sup>, Michael Melle<sup>a</sup> and Martin Schoen<sup>a,b</sup>

<sup>a</sup>Stranski-Laboratorium für Physikalische und Theoretische Chemie, Fakultät für Mathematik und Naturwissenschaften, Technische Universität Berlin, Straße des 17. Juni 135, D-10623 Berlin, Germany

<sup>b</sup>Department of Chemical and Biomolecular Engineering, Engineering Building I, Box 7905, North Carolina State University, 911 Partners Way, Raleigh, North Carolina 27695, USA

published in *Soft Matter* **6**, 1898 (2010)

## Isotropic–nematic phase transitions in confined mesogenic fluids. The role of substrate anchoring

Manuel Greschek,<sup>a</sup> Michael Melle<sup>a</sup> and Martin Schoen<sup>\*ab</sup>

Received 20th November 2009, Accepted 14th January 2010

First published as an Advance Article on the web 10th March 2010

DOI: 10.1039/b924417d

The anchoring of rodlike liquid-crystalline molecules at solid surfaces plays an important role in the design of novel nanotechnological devices such as, for example, biosensors. In this work we investigate the impact of various anchoring scenarios on the isotropic–nematic phase transition of weakly anisometric, prolate mesogens confined to a mesoscopic slit-pore. We employ isostress ensemble Monte Carlo simulations in which the isotropic–nematic transition is driven by applying an external stress in the direction parallel to the substrate plane. The fluid–fluid interaction is described by a Lennard-Jones potential with an orientation-dependent attractive term. Our simulations show that different anchoring scenarios may shift the isotropic–nematic phase transition considerably. We locate this transition through response functions such as an isostress heat capacity, isothermal compressibility, and the Maier–Saupe order parameter. Our results suggest that for the present model system the isotropic–nematic transition is likely to be continuous. For the planar anchoring scenario we observe the formation of a new layer of fluid molecules during a structural transformation preceding the isotropic–nematic transition.

### I. Introduction

Since their discovery in the late 19th century by the Viennese chemist Reinitzer<sup>1</sup> and his colleague Lehmann<sup>2</sup> the liquid-crystalline state, often referred to as the “fourth state of matter”, has received a lot of attention because of its fascinating physical properties.<sup>3</sup> The unique properties of liquid-crystalline materials prompted numerous important technological developments. Perhaps the most traditional ones are in the area of display technology where one utilizes the fact that liquid crystals can form ordered structures if exposed to suitable external fields.<sup>4,5</sup> Depending on whether these fields are switched off or on the liquid-crystalline material may be transparent to visible light or not. More recently the range of potential applications of liquid crystals has considerably broadened. It is nowadays possible to use liquid crystals as sensors in the recognition and detection of biomaterials.<sup>7, 8</sup> In tribology liquid crystals have been employed as lubricants to reduce friction coefficients, wear rates, and contact temperature of sliding surfaces.<sup>9</sup> Other applications include photonic<sup>10,11</sup> and organic electronic devices.<sup>12,13</sup> Even in food industry liquid crystals are used to stabilize dispersions and emulsions.<sup>14</sup>

With the advent of nanotechnology liquid-crystalline materials are nowadays studied with regard to their interaction with specific surface structures<sup>15,16</sup> or in nanoconfinement.<sup>6</sup> The additional length scale added through specific substrate patterns enriches the structural complexity of liquid-crystalline phases.

This was shown recently by Hough *et al.* who studied helical nanofilament phases.<sup>17</sup> The complexity of the structure of these novel, surface-induced phases could only be unravelled using a combination of different experimental techniques such as atomic force microscopy, X-ray and electron microscopy, and depolarized transmission light microscopy.

In the context of this article mesoporous materials are of particular interest. These materials can nowadays be synthesized with controllable and tailored pore-surface chemistry<sup>18</sup> such that specific anchoring scenarios for mesogenic liquid crystal molecules can be realized. The interplay between the range of the fluid–fluid interaction and the characteristic dimensions of the mesopores may cause the formation of new structures of the liquid-crystal phase in confinement that have no counterpart in a corresponding bulk system under identical thermodynamic conditions.<sup>19</sup>

If the inner surface of the mesopore is functionalized chemically the resulting anchoring scenario “experienced” by a liquid-crystal molecule in its immediate vicinity may give rise to even more complex structures that may have correlation lengths exceeding by far the range of the fluid–substrate interactions. This was recently demonstrated by Guzmán *et al.* who considered a model for a bionanosensor based upon a confined liquid-crystalline phase.<sup>6</sup> The sensor consists of thin films of liquid-crystalline materials confined between substrate surfaces with specific anchoring characteristics. If particles such as proteins or viruses bind to these solid surfaces they give rise to long-range orientational order in a nematic phase that reports the binding of these particles at specific receptors on the solid surfaces.<sup>20–22</sup> The binding process perturbs the local structure of the liquid-crystal phase over sufficiently long distances so that optical methods can be used to detect the perturbation.

This interesting phenomenon prompts us to study in greater detail various anchoring scenarios at the solid surfaces of a slit nanopore and their impact on the formation of nematic phases in

<sup>a</sup>Stranski-Laboratorium für Physikalische und Theoretische Chemie, Fakultät für Mathematik und Naturwissenschaften, Technische Universität Berlin, Straße des 17. Juni 135, 10623 Berlin, Germany. E-mail: martin.schoen@tu-berlin.de

<sup>b</sup>Department of Chemical and Biomolecular Engineering, Engineering Building I, Box 7905, North Carolina State University, 911 Partners Way, Raleigh, NC, 27695, U.S.A

confinement. In Monte Carlo simulations employing a so-called isostress ensemble<sup>23</sup> we investigate the isotropic–nematic phase transition in a confined liquid crystal employing a model potential suggested earlier by Hess and Su.<sup>24</sup> This potential is basically a Lennard-Jones (12 – 6) potential in which the attractive interaction is modified to take into account the anisotropy of prolate (or oblate) mesogens. The potential of Hess and Su has the charm of being rather simple and easy to implement. At the same time it is sufficiently realistic and has already been shown to be capable of describing the interaction between mesogens in the isotropic, nematic, and smectic phases.<sup>25,26</sup> Using this potential Steuer *et al.*<sup>25</sup> considered confined liquid crystal phases employing two anchoring scenarios: one in which no particular orientation of the mesogens is energetically preferred by the substrates (isotropic or nonspecific anchoring) and one representing a mesoscopic twisted nematic cell. However, the main focus of these earlier works<sup>25,26</sup> was on the formation of smectic phases in confinement. As we shall demonstrate below the exposure of the mesogens to surface fields favoring a specific anchoring may result in subtle structural changes very similar to those recently reported by Jordanovic and Klapp for dipolar fluids exposed to external magnetic fields.<sup>27,28</sup>

We have organized this manuscript such that we give a brief introduction to the relevant theoretical background in the subsequent Sec. II followed by a description of our model system in Sec. III. Our results for various anchoring scenarios are presented in Sec. IV. In Sec. V we summarize our findings and put them into perspective. We enclose an appendix in which we derive a molecular expression for the pressure tensor for the present model.

## II. Theoretical background

### A. Phenomenological thermodynamics

Consider  $N$  molecules in a volume of fixed but arbitrary shape and magnitude that we maintain at constant temperature  $T$ . Under these conditions thermodynamic equilibrium states correspond to minima of the free energy  $\mathcal{F}$  whose exact differential may be expressed as<sup>29</sup>

$$d\mathcal{F} = -SdT + \mu dN + V_0 \text{Tr}(\tau d\boldsymbol{\sigma}) \quad (2.1)$$

where  $S$  denotes entropy,  $\mu$  is the chemical potential of the fluid and  $V_0 = s_{x0}s_{y0}s_{z0} \equiv A_0s_{z0}$  is its volume in some undeformed reference state. Quantities  $\{s_{\alpha 0}\}$  refer to the sidelengths of a rectangular fluid lamella in that reference state. In eqn (2.1) the mechanical work exchanged between the confined fluid and its surroundings is cast in terms of stress and strain tensors  $\tau$  and  $\boldsymbol{\sigma}$ , respectively, to take notice of the anisotropy of the confined phase.<sup>29</sup>

A more explicit form of eqn (2.1) can be derived based upon the realization that in our system of ultimate interest the fluid is confined to a slit-pore where  $s_{z0}$  is the distance between the substrate surfaces. Moreover, these surfaces are assumed smooth on an atomic length scale such that for a fixed orientation of a fluid molecule the fluid–substrate potential depends only on the distance between the substrate plane and the center of mass of the molecule along the  $z$ -axis. As a consequence fluid properties are translationally invariant across the  $x$ - $y$  plane. To take notice of this symmetry we introduce

$$\frac{s_x}{s_{x0}} = \frac{s_y}{s_{y0}} = \frac{\sigma_{\parallel}}{2} + 1 \quad (2.2)$$

where the set  $\{s_{\alpha}\}$  characterizes the fluid’s shape in a (rectangular) deformed state (*i.e.*, in the absence of shear strains). Hence, we have

$$V_0 d\sigma_{xx} = d(V_0\sigma_{xx}) = \frac{s_{z0}}{2} d(\sigma_{\parallel}A_0 + 2A_0) = \frac{s_{z0}}{2} dA = V_0 d\sigma_{yy} \quad (2.3a)$$

$$V_0 d\sigma_{zz} = d(V_0\sigma_{zz}) = A_0 ds_z \quad (2.3b)$$

where  $A \equiv A_0\sigma_{\parallel}$  ( $A_0 = \text{const}$ ). Inserting these expressions into eqn (2.1) it is easy to verify that the mechanical-work contributions can be cast more explicitly as<sup>29</sup>

$$d\mathcal{F} = -SdT + \mu dN + \tau_{\parallel}s_{z0}dA + \tau_{zz}A_0ds_z \quad (2.4)$$

where

$$\tau_{\parallel} \equiv \frac{1}{2}(\tau_{xx} + \tau_{yy}) \quad (2.5)$$

is introduced for notational convenience in view of eqn (2.2).

Eqn (2.4) indicates that  $\mathcal{F}$  depends on  $T$ ,  $N$ ,  $A$ , and  $s_z$  as natural variables. However, here we wish to focus on phase transformations driven by  $\tau_{\parallel}$ . Under conditions of fixed  $\tau_{\parallel}$  equilibrium states correspond to minima of the Gibbsian potential

$$d\mathcal{G} \equiv d(\mathcal{F} - \tau_{\parallel}As_{z0}) = -SdT + \mu dN - As_{z0}d\tau_{\parallel} + \tau_{zz}A_0 ds_z \quad (2.6)$$

introduced as a Legendre transform of  $\mathcal{F}$ . In the context of this study two thermodynamic quantities, that can be derived directly from eqn (2.6), are of particular interest. These are the isostress heat capacity  $c_{\tau}$  and the isothermal compressibility  $\kappa_{\tau}$  usually referred to as “response functions”. They can be derived from eqn (2.6) *via*

$$\left(\frac{\partial^2 \mathcal{G}}{\partial T^2}\right)_{\{\cdot\}\backslash T} = -\left(\frac{\partial S}{\partial T}\right)_{\{\cdot\}\backslash T} \equiv -\frac{c_{\tau}}{T} \quad (2.7a)$$

$$\left(\frac{\partial^2 \mathcal{G}}{\partial \tau_{\parallel}^2}\right)_{\{\cdot\}\backslash \tau_{\parallel}} = -s_{z0} \left(\frac{\partial A}{\partial \tau_{\parallel}}\right)_{\{\cdot\}\backslash \tau_{\parallel}} \equiv -As_{z0}\kappa_{\tau} \quad (2.7b)$$

In eqn (2.7) we use the shorthand notation “ $\{\cdot\}\backslash x$ ” to indicate that upon differentiation the set of natural variables of  $\mathcal{G}$  is to be held constant except for variable “ $x$ ”.

### B. Molecular expressions for response functions

The connection between the thermodynamic treatment developed in Sec. IIA and the molecular level is then made through the expression<sup>23</sup>

$$\mathcal{G} = -k_B T \ln \chi \quad (2.8)$$

where  $\chi = \chi(T, N, \tau_{\parallel}, s_z)$  is the partition function of the so-called isostress ensemble. The detailed derivation presented in ref. 29 showed that

$$\chi = \sum_A \exp(\beta \tau_{\parallel} A s_{z0}) \mathcal{Q} \quad (2.9)$$

where  $\beta \equiv 1/k_B T$ ,  $k_B$  denotes Boltzmann's constant, and  $\mathcal{Q}$  is the canonical ensemble partition function in the classical limit. Following the arguments presented in detail by Gruhn and Schoen<sup>19</sup> (see also ref. 30) one may factorize  $\mathcal{Q}$  according to

$$\mathcal{Q} = \mathcal{Q}_t \mathcal{Q}_r \mathcal{Z} \quad (2.10)$$

where

$$\mathcal{Q}_t = \left( \frac{2\pi m k_B T}{h^2} \right)^{3N/2} \equiv \frac{1}{\Lambda^{3N}} \quad (2.11a)$$

$$\mathcal{Q}_r = \frac{1}{\Lambda^{2N}} \left( \frac{I}{m} \right)^N \quad (2.11b)$$

denote translational and rotational contributions to the partition function  $\mathcal{Q}$ , respectively. In eqn (2.11b),  $I$  is the moment of inertia and  $m$  is the mass of a mesogen. The specific forms of  $\mathcal{Q}_t$  and  $\mathcal{Q}_r$  result from an analytic integration over translational and angular momentum subspaces, respectively. The third factor on the right side of eqn (2.10)

$$\mathcal{Z} = \frac{1}{2^N N!} \left[ \int d\mathbf{R} d\hat{\mathbf{U}} \exp[-\beta U(\mathbf{R}, \hat{\mathbf{U}})] \right] \quad (2.12)$$

is the configuration integral where we have introduced the set  $\hat{\mathbf{U}} = \{\hat{\mathbf{u}}_1, \hat{\mathbf{u}}_2, \dots, \hat{\mathbf{u}}_N\}$ . Here  $\hat{\mathbf{u}}_i$  is a unit vector that specifies the orientation of mesogen  $i$ . The prefactor  $1/2^N$  in eqn (2.12) corrects for double-counting equivalent configurations characterized by  $\hat{\mathbf{u}}_i$  and  $-\hat{\mathbf{u}}_i$  (head–tail symmetry). Combining eqn (2.10)–(2.12) finally permits us to recast eqn (2.9) as

$$\chi = \frac{1}{\Lambda^{5N}} \left( \frac{I}{m} \right)^N \sum_A \exp(\beta \tau_{\parallel} A s_{z0}) \mathcal{Z} \quad (2.13)$$

Eqn (2.13) enables us to derive molecular expressions for the response functions introduced in Eqn (2.7). From Eqn (2.7), (2.8), and (2.13) it is a simple matter to verify

$$c'_t = 2k_B T \left( \frac{\partial \ln \chi}{\partial T} \right)_{\{\cdot\} \setminus T} + k_B T^2 \left( \frac{\partial^2 \ln \chi}{\partial T^2} \right)_{\{\cdot\} \setminus T} \quad (2.14a)$$

$$\kappa_T = \frac{k_B T}{A s_{z0}} \left( \frac{\partial^2 \ln \chi}{\partial \tau_{\parallel}^2} \right)_{\{\cdot\} \setminus \tau_{\parallel}} \quad (2.14b)$$

Starting with the somewhat simpler expression in eqn (2.14b) one first obtains

$$\frac{\partial \ln \chi}{\partial \tau_{\parallel}} = \frac{s_{z0}}{k_B T} \frac{1}{\chi} \frac{1}{\Lambda^{5N}} \left( \frac{I}{m} \right)^N \sum_A A \exp(\beta \tau_{\parallel} A s_{z0}) \mathcal{Z} = \frac{s_{z0}}{k_B T} \langle A \rangle \quad (2.15)$$

where  $\langle \dots \rangle$  denotes an average in the isostress ensemble. It is then easy to show that

$$\frac{\partial^2 \ln \chi}{\partial \tau_{\parallel}^2} = \left( \frac{s_{z0}}{k_B T} \right)^2 (\langle A^2 \rangle - \langle A \rangle^2) \quad (2.16)$$

Inserting eqn (2.16) into eqn (2.14b) we obtain

$$\kappa_T = \frac{s_{z0}}{k_B T} \frac{\langle A^2 \rangle - \langle A \rangle^2}{\langle A \rangle} \quad (2.17)$$

as the desired molecular expression for the isothermal compressibility.

To derive a similar expression for  $c'_t$  it is useful to begin by rewriting eqn (2.13) as

$$\chi = \frac{1}{2^N N! \Lambda^{5N}} \left( \frac{I}{m} \right)^N \sum_A \left[ \int d\mathbf{R} d\hat{\mathbf{U}} \exp[-\beta \mathcal{H}(\mathbf{R}, \hat{\mathbf{U}})] \right] \quad (2.18)$$

where we introduced the definition

$$\mathcal{H}(\mathbf{R}, \hat{\mathbf{U}}) \equiv U(\mathbf{R}, \hat{\mathbf{U}}) - \tau_{\parallel} A s_{z0} \quad (2.19)$$

for later convenience. Differentiating eqn (2.18) with respect to  $T$  one obtains

$$\begin{aligned} \frac{\partial \ln \chi}{\partial T} &= \frac{1}{\chi} \frac{1}{2^N N!} \left( \frac{I}{m} \right)^N \left[ \frac{5}{2} \frac{N}{T} \frac{1}{\Lambda^{5N}} \sum_A \int d\mathbf{R} d\hat{\mathbf{U}} \exp(-\beta \mathcal{H}) \right. \\ &\quad \left. + \frac{1}{\Lambda^{5N}} \frac{1}{k_B T^2} \sum_A \int d\mathbf{R} d\hat{\mathbf{U}} \mathcal{H} \exp(-\beta \mathcal{H}) \right] = \frac{5}{2} \frac{N}{T} + \frac{\langle \mathcal{H} \rangle}{k_B T^2} \end{aligned} \quad (2.20)$$

Differentiating this expression one more time with respect to  $T$  we find

$$\begin{aligned} \frac{\partial^2 \ln \chi}{\partial T^2} &= -\frac{5}{2} \frac{N}{T^2} - \frac{2\langle \mathcal{H} \rangle}{k_B T^3} \\ &\quad + \frac{1}{k_B T^2} \frac{\partial}{\partial T} \frac{\sum_A \int d\mathbf{R} d\hat{\mathbf{U}} \mathcal{H} \exp(-\beta \mathcal{H})}{\sum_A \int d\mathbf{R} d\hat{\mathbf{U}} \exp(-\beta \mathcal{H})} \\ &= -\frac{5}{2} \frac{N}{T^2} - \frac{2\langle \mathcal{H} \rangle}{k_B T^3} + \frac{1}{k_B T^2} (\langle \mathcal{H}^2 \rangle - \langle \mathcal{H} \rangle^2) \end{aligned} \quad (2.21)$$

From eqn (2.14a), (2.20), and (2.21) one finally realizes that the specific isostress heat capacity is given by

$$c_t \equiv \frac{c'_t}{N} = \frac{5}{2} k_B + \frac{\langle \mathcal{H}^2 \rangle - \langle \mathcal{H} \rangle^2}{N k_B T^2} \quad (2.22)$$

### III. The model

The mesogenic fluid considered in this work is confined to a mesoscopic slit-pore such that we may decompose the total configurational energy into a fluid–fluid (ff) and into a fluid–substrate (fs) contribution according to

$$U(\mathbf{R}, \hat{\mathbf{U}}) = U_{\text{ff}}(\mathbf{R}, \hat{\mathbf{U}}) + U_{\text{fs}}(\mathbf{R}, \hat{\mathbf{U}}) \quad (3.1)$$

More specifically,

$$U_{\text{ff}}(\mathbf{R}, \hat{\mathbf{U}}) = \frac{1}{2} \sum_{i=1}^N \sum_{j \neq i}^N u_{\text{ff}}(\mathbf{r}_{ij}, \hat{\mathbf{u}}_i, \hat{\mathbf{u}}_j) \quad (3.2)$$

where  $\mathbf{r}_{ij} \equiv \mathbf{r}_i - \mathbf{r}_j$  is the distance vector between the centers of mass of particles  $i$  and  $j$  assuming pairwise additivity of their interactions. Following a suggestion by Hess and Su<sup>24</sup> we take  $u_{\text{ff}}$  as

$$u_{\text{ff}}(\mathbf{r}_{ij}, \hat{\mathbf{u}}_i, \hat{\mathbf{u}}_j) = 4\epsilon \left[ \left( \frac{\sigma}{r_{ij}} \right)^{12} - \left( \frac{\sigma}{r_{ij}} \right)^6 \left[ 1 + \Psi(\hat{\mathbf{r}}_{ij}, \hat{\mathbf{u}}_i, \hat{\mathbf{u}}_j) \right] \right] \quad (3.3)$$

where  $r = |\mathbf{r}|$ , and  $\hat{\mathbf{r}} = \mathbf{r}/r$ . Hence,  $u_{\text{ff}}$  is a Lennard-Jones potential where the attractive contribution is modified to account for the orientation dependence of the interaction between a pair of mesogens. In eqn (3.3),  $\sigma$  denotes the “diameter” of a spherical reference molecule and  $\epsilon$  is the well depth in that reference model. An explicit form of  $\Psi$  is obtained by considering a suitable set of rotational invariants constructed from irreducible tensors of rank  $l$ . The first five rotational invariants are taken into account to preserve the head–tail symmetry  $\hat{\mathbf{u}}_i = -\hat{\mathbf{u}}_i$  of the mesogens. As a result  $\Psi$  is given by<sup>24</sup>

$$\Psi(\mathbf{r}_{ij}, \hat{\mathbf{u}}_i, \hat{\mathbf{u}}_j) = 5\epsilon_1 P_2(\hat{\mathbf{u}}_i \cdot \hat{\mathbf{u}}_j) + 5\epsilon_2 [P_2(\hat{\mathbf{u}}_i \cdot \hat{\mathbf{r}}_{ij}) + P_2(\hat{\mathbf{u}}_j \cdot \hat{\mathbf{r}}_{ij})] \quad (3.4)$$

where

$$P_2(x) = \frac{1}{2}(3x^2 - 1) \quad (3.5)$$

is the second Legendre polynomial. Depending on sign and magnitude of the anisotropy parameters  $\epsilon_1$  and  $\epsilon_2$  prolate or oblate mesogens of variable aspect ratios can be realized. Specific values of  $\epsilon_1$  and  $\epsilon_2$  employed here will be given below in Sec. IV A. The main advantage of eqn (3.3) is its simple mathematical structure. This permits rather long simulations (see Sec. IV A) at relatively moderate computational expense.

To model the fluid–substrate contribution to  $U$  we follow Steuer *et al.*<sup>25</sup> and introduce

$$U_{\text{fs}}(\mathbf{R}, \hat{\mathbf{U}}) = \sum_{k=1}^2 \sum_{i=1}^N u_{\text{fs}}^{[k]}(\mathbf{r}_i, \hat{\mathbf{u}}_i) \quad (3.6)$$

where

$$u_{\text{fs}}^{[k]}(\mathbf{r}_i, \hat{\mathbf{u}}_i) = u_{\text{fs}}^{[k]}(z_i, \hat{\mathbf{u}}_i) = 2\pi\epsilon\rho_s\sigma^2 \left[ \frac{2}{5} \left( \frac{\sigma}{\mathbf{r}_i \cdot \hat{\mathbf{e}}_z \pm s_{z0}/2} \right)^{10} - \left( \frac{\sigma}{\mathbf{r}_i \cdot \hat{\mathbf{e}}_z \pm s_{z0}/2} \right)^4 g(\hat{\mathbf{u}}_i) \right] \quad (3.7)$$

In eqn (3.7),  $\hat{\mathbf{e}}_z$  is a unit vector pointing along the  $z$ -axis of a space-fixed Cartesian coordinate system. In this coordinate system we assume the lower substrate ( $k = 1$ ) to be located at  $z_w = -s_{z0}/2$  whereas the upper one is located at  $z_w = +s_{z0}/2$  ( $k = 2$ ). In other words, eqn (3.7) assumes the substrates to be structureless such that at fixed molecular orientation  $u_{\text{fs}}$  depends only on the distance between the center of mass of each mesogen and either substrate along the  $z$ -axis. In the prefactor the areal density of the solid substrates  $\rho_s = 2/\ell^2$  where  $\ell/\sigma = \sqrt[3]{4}$  is the lattice constant of a single (100) plane of a face-centred cubic lattice.

In eqn (3.7),  $g(\hat{\mathbf{u}}_i)$  is the so-called anchoring function. By choosing different functional forms the anchoring function permits us to realize different, energetically favorable orientations of the mesogens with respect to the substrate plane. However, irrespective of the specific anchoring scenario  $0 \leq g(\hat{\mathbf{u}}) \leq 1$ . Therefore,  $g(\hat{\mathbf{u}})$  does not only affect the value of  $u_{\text{fs}}^{[k]}$  at a given center-of-mass position and orientation of a mesogen but also shifts the *location* of the potential minimum with respect to  $s_{z0}$ . Hence, one may argue that our mesogenic fluid is confined by

(thin) *soft* solid substrates. The various anchoring scenarios are introduced in Sec. IV A together with other detailed information about the simulations carried out in this work.

## IV. Results

### A. Numerical details

In this work we employ Monte Carlo simulations to study the nematization of prolate mesogens. Ideally, one would like to carry out these simulations in the grand canonical ensemble in which the thermodynamic state of the fluid is specified by the chemical potential  $\mu$  (in addition to other state variables). This would enable a direct determination of substrate-induced features of confined fluids in (virtual) thermodynamic equilibrium with the bulk. Unfortunately, nematic phases, that are at the focus of our work, are characterized by densities that are too large so that the conventional Monte Carlo algorithm for the grand canonical ensemble becomes prohibitively inefficient.<sup>31</sup> To circumvent this problem we employ an isostress ensemble in which the size of the simulation cell may vary at a constant number of fluid molecules.

In order to generate a Markov chain of configurations distributed in state space proportional to  $\exp(-\beta\mathcal{H})$  [see eqn (2.18) and (2.19)] we employ the algorithm described in Sec. 4.1 of Ref. 23. We refer to a Monte Carlo cycle as a sequence of  $N$  attempted displacements and rotations of sequentially selected fluid particles plus one attempted change of the area  $A$ . Typical runs comprise  $6 \times 10^4$  Monte Carlo cycles in regions where the fluid does not undergo any structural or phase changes. In the immediate vicinity of an isotropic–nematic (IN) phase transition one anticipates large fluctuations of  $\mathcal{H}$ . Consequently, the length of a typical run was enlarged to  $3 \times 10^5$  Monte Carlo cycles to guarantee sufficient statistical accuracy of the results (see Sec. IV B).

We express all quantities of interest in terms of the customary dimensionless (*i.e.*, “reduced”) units. For example, length is given in units of  $\sigma$ , energy in units of  $\epsilon$ , and temperature in units of  $\epsilon/k_B$ . Other derived quantities are expressed in terms of suitable combinations of these basic quantities. For example, stress is given in units of  $\epsilon/\sigma^3$ . Throughout this work we fix the temperature  $T = 1.0$  and the substrate separation  $s_{z0} = 10$ . Our systems comprise  $N = 1500$  mesogens in the bulk and  $N = 2000$  under confinement conditions. Because the anisometry of the molecules is small equilibration of our systems is relatively easy and takes typically about  $5 \times 10^3$  Monte Carlo cycles.

We follow Steuer *et al.*<sup>25,26</sup> and focus on prolate mesogens characterized by  $\epsilon_1 = 0.04$  and  $\epsilon_2 = -0.08$ . Hence, our particles are ellipsoids of revolution with an aspect ratio of 1.26. As a definition of the aspect ratio we use the ratio of zeros of  $u_{\text{ff}}$  for the end–end and side–side configuration of two mesogens. The shape of a molecule is illustrated by the contour plot of  $u_{\text{ff}}$  in Fig. 1. As one would have anticipated regions in which  $u_{\text{ff}}$  is smallest are associated with the side–side arrangements, that is configurations in which a pair of particles is arranged such that  $\hat{\mathbf{u}}_1 \cdot \hat{\mathbf{u}}_2 = 1$  and  $\hat{\mathbf{u}}_{1,2} \cdot \hat{\mathbf{r}}_{12} = 0$ . End–end configurations characterized by  $\hat{\mathbf{u}}_1 \cdot \hat{\mathbf{u}}_2 = 1$  but  $\hat{\mathbf{u}}_{1,2} \cdot \hat{\mathbf{r}}_{12} = 1$  are energetically less favorable as the plot in Fig. 1 indicates. Even though the aspect ratio of the mesogens is rather small in comparison with typical experimental

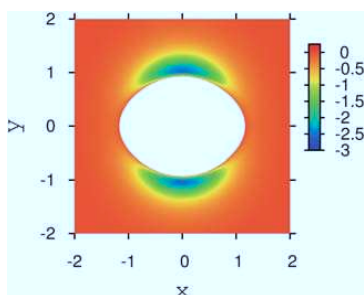


**Fig. 1** Plots of  $u_{ff}(r_{12}, \hat{u}_1, \hat{u}_2)$  for a pair of molecules located in the  $x$ - $y$  plane such that  $r_{12} = (x_{12}, y_{12}, 0)$ . The white area at the center of the plot is defined by the condition  $u_{ff}(r_{12}, \hat{u}_1, \hat{u}_2) \geq 0$  such that it approximately represents the shape of the molecule at the center of the coordinate system true to scale. In colored parts of the figure  $u_{ff}(r_{12}, \hat{u}_1, \hat{u}_2) < 0$  where the color indicates the local value of the fluid–fluid potential.

systems we have chosen these numbers for reasons of comparison with earlier work.<sup>25,26</sup>

Moreover, Hess and Su determined the bulk phase diagram for the present system at mean-field level which serves as a good orientation for selecting thermodynamic states in this work.<sup>24</sup> In particular, their results show that at the present temperature thermodynamically stable gas phases are characterized by nearly vanishing density. Preliminary (grand canonical ensemble) Monte Carlo simulations by us indeed showed that at  $T = 1.0$  gas phases in the bulk can be described by the ideal-gas equation of state to a good approximation. Under these conditions one would not expect any wetting transitions which we have indeed failed to observe.

The main focus of this paper is on various anchoring scenarios at the confining solid substrates, that is energetically favored orientations of a single mesogen with respect to the substrate plane. Specifically we consider the following four anchoring functions:

$$g(\hat{u}) = (\hat{u} \cdot \hat{e}_x)^2 + (\hat{u} \cdot \hat{e}_y)^2 \quad (4.1a)$$

$$g(\hat{u}) = (\hat{u} \cdot \hat{e}_x)^2 \quad (4.1b)$$

$$g(\hat{u}) = \hat{u} \cdot \hat{u} = 1 \quad (4.1c)$$

$$g(\hat{u}) = (\hat{u} \cdot \hat{e}_z)^2 \quad (4.1d)$$

The anchoring scenarios described by eqn (4.1) form three qualitatively different groups. If eqn (4.1c) is used the walls themselves do not favor any particular orientation of a molecule (nonspecific anchoring). However, nonetheless one anticipates weakly homeotropic alignment because

1. more molecules can be anchored per unit substrate area if their longer axis is perpendicular to the substrate plane and

2. because Fig. 1 indicates that the side-side arrangement of any pair of molecules is energetically most favorable.

Hence, the homeotropic alignment at the substrate arises only *indirectly* as a consequence of their symmetry-breaking presence such that the anchoring is weak. Using the anchoring function given in eqn (4.1d) the substrates themselves favor homeotropic alignment *directly*. In this case the symmetry-breaking presence

of the substrate and the intermolecular interaction potential have a cooperative impact. Consequently, anchoring is very strong in this case. The third group of anchoring scenarios is represented by the anchoring functions given in eqn (4.1a) and (4.1b). In both cases planar alignment is favored energetically. Anchoring is again considered strong because it is capable of overcoming the homeotropic alignment arising in the mere presence of nonspecifically anchoring substrates. The difference is that eqn (4.1a) gives a molecule the freedom to assume *any* orientation in the substrate plane whereas the anchoring function introduced in eqn (4.1b) “pins” the longer molecular axis to the  $x$ -axis. Hence, in this latter case anchoring at the substrates is stronger than in the case described by eqn (4.1a).

## B. Accuracy and reliability

At this point it seems worthwhile to demonstrate the reliability and accuracy of our simulation technique fully described in ref. 23. As already explained in Sec. II,  $\tau_{||}$  is a fixed input parameter in each individual Monte Carlo run. However, using eqn (A1) and (A2) we are able to also *compute*  $\tau_{||, ff}$  as an ensemble average. Because the fluid–substrate interaction depends only on the  $z$ -coordinate of the center of mass of each particle  $\tau_{||} = \tau_{||, ff}$  should hold. Entries in Table 1 illustrate the accuracy with which the numerical data satisfy this equality. Note that we have deliberately selected state points in the vicinity of the IN transition for the various anchoring scenarios (see Fig. 3).

We base our analysis of the IN phase transition largely on the response functions  $\kappa_T$  and  $c_\tau$  computed from eqn (2.17) and (2.22), respectively. In Fig. 2 we show the evolution of the response functions with the number of Monte Carlo cycles. We have deliberately chosen a thermodynamic state in the immediate vicinity of an IN transition. In the vicinity of such a transition both response functions become relatively large indicating that fluctuations in both  $\mathcal{H}$  and  $A$  are substantial. Therefore, care needs to be taken to compute both quantities with sufficient accuracy. The plots in Fig. 2 clearly show that runs of about  $2.0 \times 10^5$  Monte Carlo cycles can be expected to give reliable results; much shorter runs of about  $6.0 \times 10^4$  Monte Carlo cycles are sufficient if the thermodynamic state considered is sufficiently far away from any phase transition as we have checked through plots similar to the ones presented in Fig. 2.

**Table 1** Comparison between input values  $\tau_{||}$  for the isostress ensemble Monte Carlo simulations and  $\tau_{||, ff}$  computed as an ensemble average from eqn (2.5) and (A5) in those simulations

Anchoring	$g(\hat{u})$	$-\tau_{  }$	$-\tau_{  , ff}$
Bulk system	–	–1.65	–1.6505
		–1.70	–1.7038
Planar	eqn (4.1a)	–1.50	–1.5000
		–1.55	–1.5499
Directional	eqn (4.1b)	–1.00	–1.0009
		–1.10	–1.0997
Nonspecific	eqn (4.1c)	–1.30	–1.3011
		–1.40	–1.3999
Homeotropic	eqn (4.1d)	–1.00	–1.0004
		–1.10	–1.0977

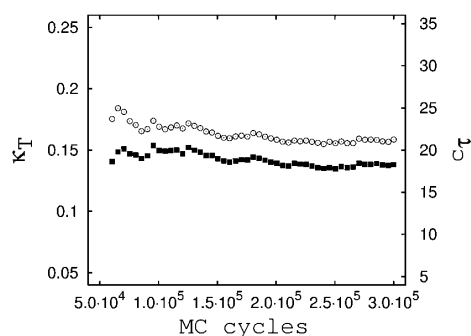


**Fig. 2** Isothermal compressibility  $\kappa_T$  (■) (left ordinate) and isostress heat capacity (○) (right ordinate) as a function of the length of a typical Monte Carlo (MC) run in the vicinity of the IN phase transition at  $\tau_{||} = -1.500$  and planar anchoring [see eqn (4.1a), Fig. 6(b)].

### C. Formation of nematic phases in confinement

For the following quantitative discussion of various anchoring scenarios it is useful to introduce the Maier–Saupe nematic order parameter  $S^{32-34}$  through the so-called alignment tensor<sup>35</sup>

$$\mathbf{Q} \equiv \frac{1}{2N} \sum_{i=1}^N (3\hat{u}_i\hat{u}_i - \mathbf{1}) \quad (4.2)$$

where  $\hat{u}\hat{u}$  is the direct (*i.e.*, dyadic) product of the vector  $\hat{u}$  with itself and  $\mathbf{1}$  is the unit tensor. Hence,  $\mathbf{Q}$  is a symmetric, traceless, second-rank tensor which can be represented by a (symmetric)  $3 \times 3$  matrix. We follow Eppenga and Frenkel<sup>36</sup> and compute the largest eigenvalue  $\lambda_m$  of this matrix using Jacobi's method.<sup>37</sup> The Maier–Saupe order parameter may then be obtained as an ensemble average  $S \equiv \langle \lambda_m \rangle$ . On account of its definition  $S = 0$  for an isotropic phase whereas  $S = 1$  if a nematic phase of perfectly oriented mesogens forms. A value of  $S \geq 0.4$  is already indicative of a nematic phase according to the mean-field theory of Maier and Saupe.<sup>32,33</sup>

In Fig. 3 we present plots of  $S$  as a function of the applied external compressional stress  $\tau_{||}$ . We begin our discussion by presenting data for the bulk as a reference in Fig. 3(a). Bulk phases were also investigated earlier by Steuer *et al.*<sup>25</sup> The plot of  $S$  in Fig. 3(a) shows that for low compressional stresses  $|\tau_{||}|$ ,  $S \leq 0.1$  indicating that the liquid crystal is in its isotropic phase as one would have anticipated. At  $\tau_{||} \approx -1.70$ ,  $S$  rises sharply but seemingly continuously and reaches a final value of  $S \approx 0.6$ . The apparent continuous variation of  $S$  with  $\tau_{||}$  (given our resolution of data points) indicates that the IN phase transition is likely to be continuous, too. This notion is supported by the mean-field phase diagram of Hess which exhibits a line of continuous IN phase transitions in the temperature range relevant to this study.<sup>24</sup> We locate the transition point *via* the inflection of  $S$

$$\frac{d^2 S}{d\tau_{||}^2} \Big|_{\tau_{||} = \tau_{||}^N} \stackrel{!}{=} 0 \quad (4.3)$$

The solution of this equation gives  $\tau_{||}^N \approx -1.70$  for the IN phase transition in perfect agreement with the findings of Steuer *et al.*<sup>25</sup>

That this definition of the IN phase transition is operationally meaningful is supported by the plot of the isostress heat capacity

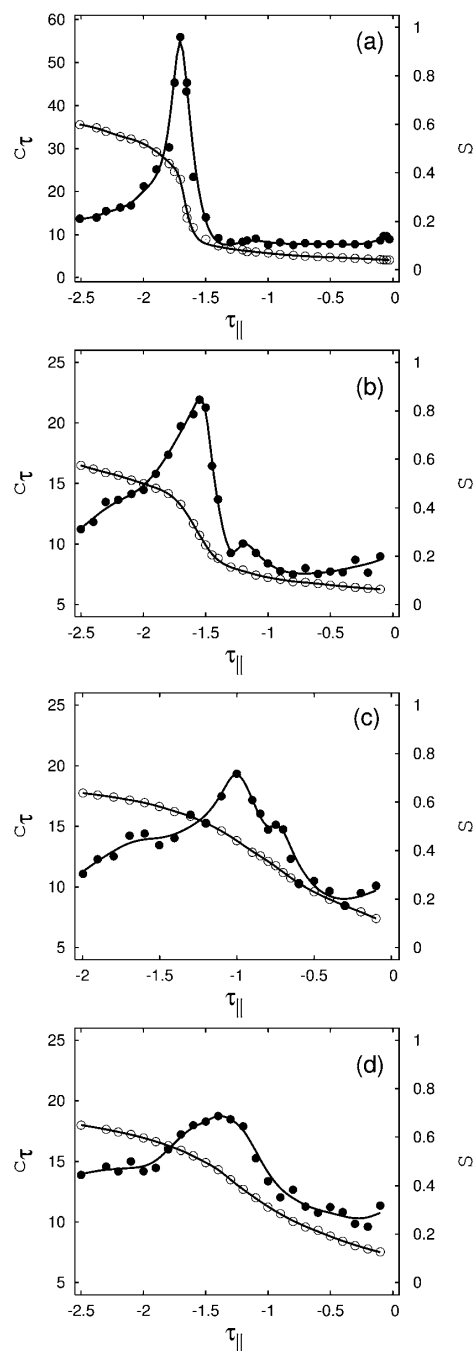


**Fig. 3** Plots of isostress heat capacity  $c_T$  (●) (left ordinate) and nematic order parameter  $S$  (○) (right ordinate) as functions of the applied transverse stress  $\tau_{||}$  for the bulk (a) and confined fluids (b) with planar [see eqn (4.1a)], (c) directional [see eqn (4.1b)], and (d) isotropic anchoring [see eqn (4.1c)].

$c_r$  also presented in Fig. 3(a). It exhibits a pronounced peak at the same  $\tau_{\parallel}^N \approx -1.70$  where  $S$  has its inflection. In addition, the variation of  $c_r$  around  $\tau_{\parallel}^N$  supports the notion of a continuous transition where one would expect large values of  $c_r$ . Moreover the shape of this curve is reminiscent of the  $\lambda$ -transition at which ordinary liquid  $^4\text{He}$  becomes superfluidic through a phase transition that is also continuous<sup>38</sup> but driven by temperature as the relevant thermodynamic field.

Additional support for the IN phase transition as a continuous one is provided by plots of the mean density  $\rho \equiv N/\langle A \rangle_{s_{z0}}$  in Fig. 4 which varies continuously with the compressional stress. Data for the bulk liquid in that figure show, in fact, only a slight change in slope around  $\tau_{\parallel}^N$  in agreement with earlier findings of Steuer *et al.* (see data for the compressional scan in the uppermost part of Fig. 3 of ref. 25). Last but not least all the data sets presented in this work turn out to be fully reversible with no hysteresis as one would expect for continuous phase transitions.

Turning next to results for the confined fluid with planar anchoring [see eqn (4.1a)] plots in Fig. 3(b) reveal a number of differences. First, the increase of  $S$  with  $\tau_{\parallel}$  in the isotropic phase is more pronounced than in the bulk [cf., Fig. 3(a)]. This reflects the prealignment of the mesogens in the isotropic phase on account of anchoring at the substrates. As  $|\tau_{\parallel}|$  becomes larger increasingly more mesogens arrange their longer axes in directions parallel with the substrate plane. Hence, prealignment extends into regions of the confined fluid that are farther removed from the walls as  $|\tau_{\parallel}|$  increases. Because of prealignment in the isotropic phase the variation of  $S$  at the IN transition turns out to be weaker compared with the bulk. Second, on account of a substantial degree of planar prealignment in the isotropic phase the confined fluid loses less rotational entropy compared with the previously discussed bulk system. Consequently, the peak visible in the plot of  $c_r$  at the IN transition in Fig. 3(b) is smaller compared with its bulk counterpart [see Fig. 3(a)]. Third, the location of the IN transition appears to be shifted to a lower compressional stress  $\tau_{\parallel}^N \approx -1.55$  because the substrates play a cooperative role in the formation of nematic phases. However, for the sake of brevity we defer a more comprehensive discussion of the relation between the loss of rotational entropy and the location of the IN transition to Sec. V.

At this point it seems more interesting to compare the previous anchoring scenario with one in which the anchoring function still favors a planar orientation but in addition ‘pins’ the mesogens along the  $x$ -axis. This is effected by  $g(\hat{u})$  given in eqn (4.1b). As one notices by comparing plots for  $S$  in Fig. 3(b) and 3(c) the variation of  $S$  in the isotropic phase is even stronger for the directional anchoring. This is because prealignment is stronger on account of the directional pinning. The cooperative effect of the substrates in the formation of nematic phases is even stronger and causes a substantial shift of the IN transition to a lower value of  $\tau_{\parallel}^N \approx -1.00$ . Because of the stronger prealignment of the mesogens in the isotropic phase the loss of rotational entropy at the IN transition is smaller than in the previously discussed case in which the mesogens in the isotropic phase had more freedom to rotate in the  $x$ - $y$  plane. Consequently, the maximum visible in the plot of  $c_r$  at the IN transition is lower in Fig. 3(c) compared with Fig. 3(b) and compared especially with the bulk in Fig. 3(a).

For the sake of completeness we also include the nonspecific anchoring represented by eqn (4.1c). As pointed out in Sec. IV A

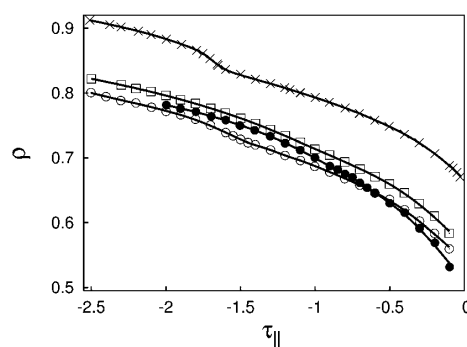


**Fig. 4** Mean density  $\rho$  as a function of external transverse stress. ( $\times$ ) bulk; the other three data sets are obtained for confined fluids using a specific anchoring scenario represented by  $g(\hat{u})$  from eqn (4.1a) ( $\circ$ ), eqn (4.1b) ( $\bullet$ ), and eqn (4.1c) ( $\square$ ).

the substrates still have a cooperative effect on the formation of nematic phases but favor homeotropic rather than planar alignment of the mesogens. The prealignment in the isotropic phase is comparable to planar anchoring with directional pinning as reflected by similar values of the nematic order parameter in Fig. 3(c) and 3(d). However, because the substrates do not support the formation of nematic phases energetically (see Sec. V) the IN transition occurs at  $|\tau_{\parallel}^N| \approx 1.40$  which is substantially larger than  $|\tau_{\parallel}^N| \approx 1.00$  observed for planar anchoring with directional pinning [see Fig. 3(c)]. We also note that our value for  $\tau_{\parallel}^N$  for the nonspecific anchoring is slightly smaller than the value  $|\tau_{\parallel}^N| \approx 1.50$  reported by Steuer *et al.*<sup>25</sup> who did, however, consider a larger slit-pore of  $s_{z0} = 15$ . Because of a similar degree of prealignment in the isotropic phases for nonspecific anchoring and planar anchoring with directional pinning one anticipates the fluid to lose a comparable amount of rotational entropy at the IN transition. This argument suggests that the peak in  $c_r$  at the IN transition should be comparable in height for the two anchoring scenarios. A comparison of plots in Fig. 3(c) and 3(d) supports that notion. However, regardless of the specific anchoring scenario the IN transition turns out likely to be continuous for the present model. This is supported also by corresponding plots of the mean density presented in Fig. 4.

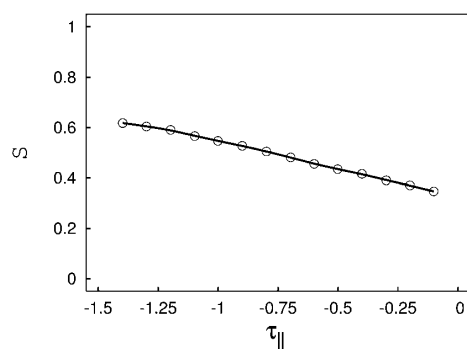


**Fig. 5** Plot of the nematic order parameter  $S$  as a function of  $\tau_{\parallel}$  for the homeotropic anchoring scenario [see eqn (4.1d)].

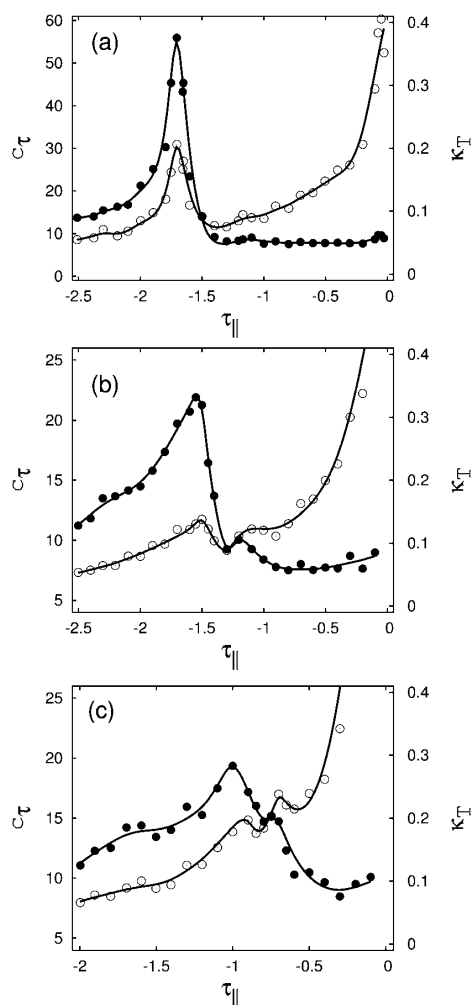


**Fig. 6** As Fig. 3 but for heat capacity  $c_T$  (●) (left ordinate) and isothermal compressibility  $\kappa_T$  (○) (right ordinate). Parts (a)–(c) of the figure parallel those of Fig. 3. No data are shown parallel to the plots in Fig. 3(d).

Finally, in the case of homeotropic anchoring [see eqn (4.1d)] we do not observe any IN phase transition. The reason is that even at the lowest compressional stress the value of the nematic order parameter exceeds the threshold  $S \approx 0.4$  predicted for the IN transition by the Maier–Saue theory as one can see from Fig. 5. The plot shows that  $S$  is no longer sigmoidal but varies almost linearly.

#### D. Structure and local order

Plots in Fig. 3(b) and 3(c) reveal another interesting feature which accompanies the IN phase transition. For both planar anchoring scenarios the isostress heat capacity exhibits a small maximum at lower compressional stress. This peak is located at  $|\tau_{\parallel}| < |\tau_{\parallel}^N|$ , that is prior to the one associated with the IN phase transition. To analyze the significance of this “side” peak it is useful to compare plots of  $c_T$  with those of  $\kappa_T$ .

Plots in Fig. 6(b) and 6(c) show that the small side maxima in  $c_T$  at  $\tau_{\parallel} \approx -1.20$  [see Fig. 6(b)] and at  $\tau_{\parallel} \approx -0.75$  [see Fig. 6(c)] are preceded by a shoulder or a small maximum in  $\kappa_T$  at  $\tau_{\parallel} \approx -1.10$  and  $-0.70$ , respectively. Because these subtle features occur at stresses prior to the onset of nematization they must reflect some other, apparently rather weak, structural feature that arises before the confined fluid attains a significant degree of nematic order. To gain some deeper insight we analyze the local structure of the confined fluid in terms of the local density that we may define through

$$\rho(z) = \frac{1}{\delta z} \left\langle \frac{N(z)}{A} \right\rangle \quad (4.4)$$

where  $N(z)$  is the number of mesogens in a given configuration that have the  $z$ -coordinate of their center-of-mass position within a small interval  $\delta z$  centered on  $z$ . Here we take  $\delta z = 0.1$ . In a similar fashion we analyze the local orientation of the confined fluid. To that end we introduce the *local* alignment tensor  $\mathbf{Q}(z)$  paralleling precisely the definition of the global one given in eqn (4.2). Using the same procedure already explained in Sec. 4.3 we obtain a *local* nematic order parameter  $S(z) \equiv \langle \lambda_m(z) \rangle$  where  $\lambda_m(z)$  is the largest *local* eigenvalue of  $\mathbf{Q}(z)$ . However, it has been noted by Eppenga and Frenkel<sup>36</sup> and later by Richter and Gruhn<sup>39</sup> that  $S(z)$  depends on  $N(z)$  for small values of this latter

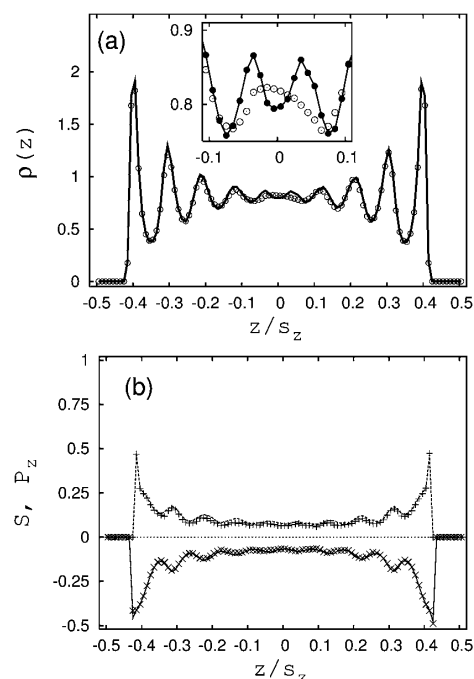


**Fig. 7** (a) Local density  $\rho(z)$  as a function of position between lower and upper substrate planes located at  $z_w = \pm 0.5$  for  $\tau_{\parallel} = -1.00$  (○) and  $\tau_{\parallel} = -1.10$  (—) [cf., Fig. 6(b)] for the planar anchoring scenario [see eqn (4.1a)]. The inset is an enlargement where (●) refers to the case  $\tau_{\parallel} = -1.10$ . (b) As (a) but for the local nematic order parameter  $S(z)$  where  $\tau_{\parallel} = -1.00$  (+),  $\tau_{\parallel} = -1.10$  (—). Also shown are data for  $P_z(z)$  [see eqn (4.5)];  $\tau_{\parallel} = -1.00$  (×),  $\tau_{\parallel} = -1.10$  (—).

quantity. The reason is that for small particle numbers there is always a certain net alignment that gives rise to spurious nematic-like order even though the *entire* system is still in an isotropic phase. As a result  $S(z)$  is nonzero even in the isotropic phase. To correct for this spurious order we follow the procedure advocated by Richter and Gruhn [see eqn (B6) and (B7) of ref. 39] and apply their finite-size correction to our results for  $S(z)$ . Using  $\delta z = 0.1$  and given the typical system sizes employed in this study  $N(z)$  is typically of the order of 25 such that the finite-size correction proposed by Richter and Gruhn should give reliable results for  $S(z)$  in the isotropic phase.

Plots of  $\rho(z)$  and  $S(z)$  are presented in Fig. 7 for  $\tau_{\parallel} = -1.00$  and  $-1.10$  and planar anchoring of the mesogenic molecules at the substrate. The states selected pertain to the range where  $c_{\tau}$  and  $\kappa_{\tau}$  in Fig. 6(b) exhibit a small maximum and a shoulder, respectively. As the plot in Fig. 7(a) indicates the fluid undergoes a structural change during which a new layer of fluid molecules is forming at the center of the slit-pore. The formation of this new layer can be seen more clearly from the inset of that figure. As the plots in Fig. 7(b) indicate there is a very weak increase of the local nematic order with increasing compression. Nevertheless, in both cases the fluid at the center of the pore is still in an isotropic state because  $S(z) < 0.4$  according to the criterion suggested by Maier and Saupe's theory.<sup>32,33</sup>

The occurrence of a new layer at the pore center can be attributed to the anisotropy of the mesogens in conjunction with the planar anchoring scenario. To appreciate this we need to demonstrate first that the orientation of the mesogens is preferentially parallel with the substrate plane. To that end it is useful to introduce

$$P_z(z) \equiv \frac{1}{2} \left\langle \frac{1}{N(z)} \sum_{i=1}^{N(z)} [3(\hat{u}_i \cdot \hat{e}_z)^2 - 1] \right\rangle \quad (4.5)$$

Hence,  $P_z(z) = 1$  if all molecules are homeotropically aligned ( $|\hat{u}_i \cdot \hat{e}_z| = 1$ ). If, on the other hand, molecules would be aligned in a parallel fashion  $P_z(z) = -0.5$  ( $|\hat{u}_i \cdot \hat{e}_z| = 0$ ).

An inspection of Fig. 7(b) shows that as one approaches either substrate the nematic order increases because  $S(z)$  increases as  $|z| \rightarrow s_{20}/2$ . Moreover, particles in the immediate vicinity of the substrate are oriented such that their long axes are parallel with the substrate plane. This follows because  $P_z \rightarrow -0.5$  as  $|z| \rightarrow s_{20}/2$  indicating an almost complete absence of homeotropically oriented molecules. Because  $P_z(z) < 0$  everywhere we conclude that  $S(z) > 0$  for  $|z| \rightarrow 0$  indicates a weak but preferentially planar orientation of molecules as one approaches the pore center. However, this weak planar orientation still present at  $z = 0$  causes a more efficient packing of the mesogens because they align with their neighbors such that their longer axes are preferentially perpendicular to the  $z$ -direction. Hence, the weak planar prealignment visible in the plots of  $S(z)$  in Fig. 7(b) is ultimately responsible for the formation of a new fluid layer.

At the compressional stress at which the IN transition occurs packing of the mesogens is only slightly affected by increasing  $|\tau_{\parallel}|$  as plots in Fig. 8(a) reveal. However, as one would have expected from plots of  $S$  versus  $\tau_{\parallel}$  in Fig. 3(b) and 6(b) the local planar order increases substantially in the vicinity of the transition. This can be seen from Fig. 8(b) where  $S(z)$  increases significantly with increasing compression whereas  $P_z(z)$  decreases simultaneously.

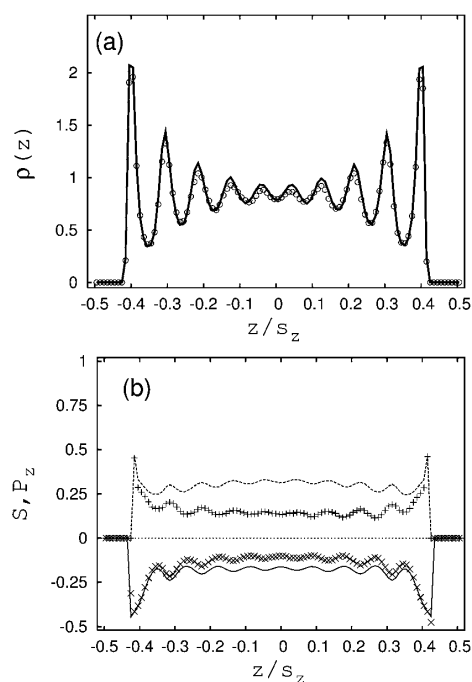


**Fig. 8** As Fig. 7, but for (a)  $\tau_{\parallel} = -1.30$  ( $\circ$ ),  $\tau_{\parallel} = -1.55$  (—); (b)  $S(z)$ :  $\tau_{\parallel} = -1.30$  (+),  $\tau_{\parallel} = -1.55$  (---);  $P_z(z)$ :  $\tau_{\parallel} = -1.30$  ( $\times$ ),  $\tau_{\parallel} = -1.55$  (—) [cf., Fig. 3(b) and 6(b)].

The same structural features arise in the case where the mesogens are anchored in a planar manner but are directionally pinned [see eqn (4.1b), Fig. 6(c)] as we have verified by analyzing  $\rho(z)$ ,  $S(z)$ , and  $P_z(z)$  for this case. Again the peak in  $\kappa_{\tau}$  and  $c_{\tau}$  at lower compressional stress  $|\tau_{\parallel}|$  in Fig. 6(c) can be attributed to the formation of an additional layer through the mechanism explained above.

In the case of homeotropic anchoring the structure of the confined fluid is distinctly different as a comparison between plots in Fig. 7 and 8 on one hand and Fig. 9 on the other hand indicate. In the homeotropic case packing of the mesogens within a single layer turns out to be more efficient because peaks of  $\rho(z)$  are generally higher compared with the planar anchoring scenario over a comparable pressure range [see Fig. 8(a)]. In general, increasing  $|\tau_{\parallel}|$  causes long-range translational order to develop in the direction perpendicular to the substrate plane as the plots in Fig. 9(a) illustrate. The bulk-like region at the pore center visible in the plot of  $\rho(z)$  for  $\tau_{\parallel} = -0.10$  gives way to an oscillatory structure at  $\tau_{\parallel} = -1.40$ . On account of the larger compressional stress in this latter case  $\rho(z)$  oscillates around a somewhat higher mean density. The decay of the amplitude of the oscillations indicates that the system is still not in a smectic phase at  $\tau_{\parallel} = -1.40$ . The plot in Fig. 9(b) shows that irrespective of  $\tau_{\parallel}$  the homeotropic alignment of molecules directly at the surface is almost perfect because both  $P_z(z)$  and  $S(z)$  tend to 1 as  $|z| \rightarrow s_{20}/2$ . At  $\tau_{\parallel} = -0.10$  the local order depends rather strongly on the distance from the substrate. Note a small deviation between  $S(z)$  and  $P_z(z)$  around the pore mid plane. This reflects the small remaining finite-size effect in  $S(z)$  due to the small

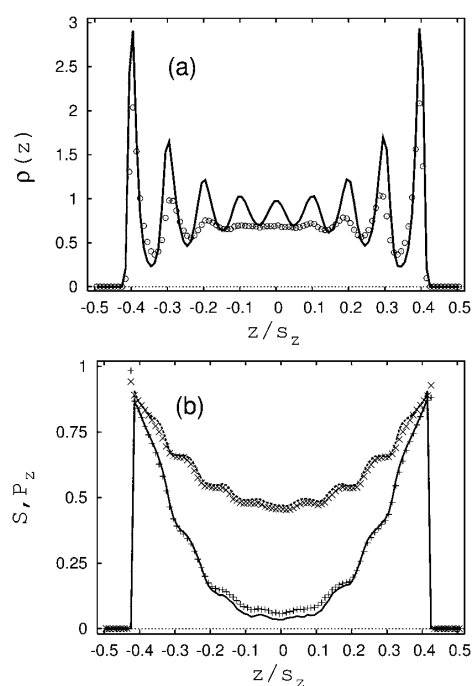


**Fig. 9** As Fig. 6 but for (a)  $\tau_{\parallel} = -0.10$  ( $\circ$ ),  $\tau_{\parallel} = -1.40$  ( $-$ ); (b)  $S(z)$ :  $\tau_{\parallel} = -0.10$  ( $+$ ),  $\tau_{\parallel} = -1.40$  ( $\times$ );  $P_z(z)$ :  $\tau_{\parallel} = -0.10$  ( $-$ ),  $\tau_{\parallel} = -1.55$  ( $- -$ ).

number of particles in each histogram bin. The empirical finite-size correction of Richter and Gruhn<sup>39</sup> is not capable of eliminating this effect completely. At  $\tau_{\parallel} = -1.40$  the position dependence of the local order is much weaker and more pronounced in the additional layers forming at the pore center.

## V. Summary and conclusions

We are using Monte Carlo simulations in an isostress ensemble to investigate the structure of prolate mesogens confined to a mesoscopic slit-pore. Our focus is on the impact of four different anchoring scenarios on the IN transition. We present results for a single characteristic temperature  $T = 1.0$  at which isotropic and nematic phases of the present model fluid may form.<sup>24</sup> We consider one pore width  $s_{z0} = 10$  such that the confined fluid is still weakly stratified at the pore center and for compressional stresses at which the IN transition occurs. The selection of the present pore width turns out to be advantageous because the orientation dependent fluid–substrate interaction at the pore center turns out to be strong enough to support the formation of additional fluid layers in the case of planar anchoring scenarios. The formation of these layers occurs prior to the IN transition. This formation of additional layers can be ascribed to a more efficient packing of the mesogens that becomes possible if in the isotropic phase the mesogens prealign their longer axes with the substrate plane as the compressional stress increases towards  $\tau_{\parallel}^N$ . On account of this planar prealignment the shorter axes of these mesogens point in the  $z$ -direction in which stratification of the confined fluid is

supported by the symmetry-breaking presence of the substrates. Because the structural reorganization of the mesogens is associated with a change in their packing characteristics it is preceded by a characteristic change in the fluid’s isothermal compressibility [see Fig. 6(b) and 6(c)].

Perceiving the confining solid substrates as an external field a similar field-induced formation of additional layers has been reported recently by Jordanovic and Klapp who investigated confined dipolar fluids in external magnetic fields pointing in different directions relative to the substrate plane.<sup>27,28</sup> In the present study the specific anchoring scenario may be interpreted as the analogue of the direction of the magnetic field in the study of Jordanovich and Klapp. Hence, the appearance of additional layers in a confined fluid of anisometric molecules caused by some direction-dependent external field seems to be a generic feature which is qualitatively independent of details of the intermolecular interaction potential or the precise nature of the external field.

From a more general perspective the IN transition turns out to be driven by energetic and entropic effects. For example, in the nematic phase the configurational potential energy of the mesogens is generally lower than in the isotropic phase because the number of side–side configurations of pairs of mesogens increases. In the nematic phase only configurations in which the orientations of individual mesogens are preferentially aligned with the global director  $\hat{n}$  contribute to the configuration integral. Hence, the IN transition is accompanied by a loss in rotational entropy. The entropic effects are most clearly visible in the variation of the isostress heat capacity  $c_{\tau}$  during the IN transition.

In confinement the location of the IN transition is determined by the specific anchoring scenario which may [see eqn (4.1a), (4.1b), and (4.1d)] or may not discriminate energetically between various orientations of the mesogens [see eqn (4.1c)] even in the isotropic phase. However, even with a comparable degree of energetic discrimination in the isotropic phase the loss of rotational entropy during the IN transition may be quite different.

Take as an example the planar and directional anchoring scenarios. At the same compressional stress  $\tau_{\parallel} = -0.5$  in the isotropic phase the total mean configurational energy  $\langle U \rangle$  turns out to be nearly the same irrespective of the specific anchoring scenario ( $-5.531$ , planar anchoring;  $-5.522$ , directional anchoring). However, prealignment is much larger for the directional ( $S \approx 0.23$ ) than for the planar anchoring scenario ( $S \approx 0.08$ ). This is because in the planar anchoring scenario mesogens have greater freedom to orient themselves in the  $x$ – $y$  plane under isoenergetic conditions. Hence, in this latter case the loss of rotational entropy during the IN transition is bigger. This notion is supported by the fact that at the IN transition the peak in the plot of  $c_{\tau}$  is taller for the planar anchoring scenario. Given the location of the IN transition for both anchoring scenarios [see Fig. 3(b) and 3(c)] we conclude that a smaller loss in rotational entropy supports the transition.

Comparing next the directional with the nonspecific anchoring scenario one notices that prealignment in the isotropic phases is nearly the same because the plots of  $S$  versus  $\tau_{\parallel}$  in Fig. 3(c) and 3(d) can be mapped onto one another if properly shifted with respect to  $\tau_{\parallel}^N$ . Hence, the loss of rotational entropy at the IN transition should be comparable. However, in case of nonspecific anchoring the substrates do not support the IN transition

energetically. This is illustrated by the fact that  $\langle U_{fs} \rangle \approx -0.653$  ( $\tau_{\parallel} = -1.000$ ) and  $\langle U_{fs} \rangle \approx -0.659$  ( $\tau_{\parallel} = -2.500$ ). In the case of the directional anchoring scenario we obtain  $\langle U_{fs} \rangle \approx -0.282$  ( $\tau_{\parallel} = -0.500$ ) but  $\langle U_{fs} \rangle \approx -0.413$  ( $\tau_{\parallel} = -2.000$ ) over a comparable range of stresses around the IN transition. Because  $|\tau_{\parallel}^N|$  is smaller for the directional than for the nonspecific anchoring scenario we conclude that energetic discrimination of mesogen configurations by the solid substrates is also cooperative in the IN transition.

These conclusions make sense in view of our results for the homeotropic anchoring scenario where we have been unable to observe an IN transition even at the lowest compressional stress  $\tau_{\parallel} = -0.100$ . In this case the alignment is strongest indicated by plots of  $S(z)$  which show that the first two layers at each wall are already nematic for this low compressional stress. Unlike for the nonspecific anchoring scenario, eqn (4.1d) supports a homeotropic alignment of individual mesogens energetically. Hence, a strong energetic discrimination in combination with a minimum loss of rotational entropy shifts the IN phase transition presumably to vanishingly low compressional stresses if this transition is not completely suppressed in our current system.

Moreover, all our results at the IN transition seem free of any hysteresis as we vary  $\tau_{\parallel}$ . This suggests that for the present model the IN phase transition may be continuous or weakly discontinuous. However, to discriminate between continuous and discontinuous phase transitions beyond doubt one would have to resort to a careful finite-size analysis. While this is computationally quite demanding for the present system we emphasize that in this work we are concerned with the impact of various anchoring scenarios on thermodynamic and structural features at the IN transition rather than the nature of the phase transition itself. We also note that the observation of reversibility is not in contradiction with the results of Steuer *et al.* who reported a pronounced hysteresis associated with the isotropic-nematic transition.<sup>25</sup> These earlier authors increased the compressional stress until eventually a smectic phase formed in their system. Starting from the smectic regime and reducing the compressional stress eventually returned the system to the isotropic without intermittent nematic phases. This is because the smectic phases are exceedingly more stable than the nematic ones.

Continuous isotropic–nematic transitions have also been reported experimentally by Selinger *et al.* who studied the nematic order parameter for elastomers<sup>40</sup> and by Finkelmann and co-workers<sup>41</sup> as well as by Thomsen *et al.*<sup>42</sup> both for the same system class. On the theoretical side it was shown that an entropically driven IN phase transition exists in lattice-polymer models.<sup>43</sup> However, by applying a careful finite-size scaling analysis these latter authors could establish this transition as a discontinuous one.

### Appendix A: Molecular expression for the stress tensor

Here we derive an expression for the pressure tensor  $\mathbf{P}$  in an anisotropic fluid without taking recourse to any thermodynamic potential. Employing the so-called hypervirial theorem discussed in Appendix E.2 of ref. 30 one eventually obtains

$$\mathbf{P} = -\boldsymbol{\tau} = \rho k_B T \mathbf{1} + \frac{1}{V} \left\langle \sum_{i=1}^N \mathbf{r}_i \mathbf{F}_i \right\rangle \quad (\text{A1})$$

for the pressure tensor in an inhomogeneous fluid where the first term on the far right side follows by assuming a Maxwell–Boltzmann distribution of the linear momenta of the fluid molecules. To derive a molecular expression for  $\tau_{\parallel}$  [see eqn (2.5)] from eqn (A1), we will focus only on fluid–fluid contributions to the forces because for our model  $U_{fs}$  depends only on  $\{z_i\}$  such that the fluid–substrate potential does not contribute to  $\tau_{\parallel}$ . In eqn (A1)

$$\sum_{i=1}^N \mathbf{r}_i \mathbf{F}_i = \frac{1}{2} \sum_{i=1}^N \sum_{j \neq i}^N \mathbf{r}_{ij} \mathbf{F}_{ij} = -\frac{1}{2} \sum_{i=1}^N \sum_{j \neq i}^N \nabla u_{ff}(\mathbf{r}_{ij}, \hat{\mathbf{u}}_i, \hat{\mathbf{u}}_j) \quad (\text{A2})$$

where  $\nabla \equiv \partial/\partial \mathbf{r}_{ij}$ . Using eqn (3.3) it is straightforward to verify that

$$\begin{aligned} \nabla u_{ff} = & 48\varepsilon \left[ \left( \frac{\sigma}{r_{ij}} \right)^{12} - \frac{1}{2} \left( \frac{\sigma}{r_{ij}} \right)^6 \Psi(\hat{\mathbf{r}}_{ij}, \hat{\mathbf{u}}_i, \hat{\mathbf{u}}_j) \right] \frac{\hat{\mathbf{r}}_{ij}}{r_{ij}} \\ & + 60\varepsilon\varepsilon_2 \left( \frac{\sigma}{r_{ij}} \right)^6 \left\{ (\hat{\mathbf{u}}_i \cdot \hat{\mathbf{r}}_{ij}) \hat{\mathbf{u}}_i + (\hat{\mathbf{u}}_j \cdot \hat{\mathbf{r}}_{ij}) \hat{\mathbf{u}}_j - [(\hat{\mathbf{u}}_i \cdot \hat{\mathbf{r}}_{ij})^2 + (\hat{\mathbf{u}}_j \cdot \hat{\mathbf{r}}_{ij})^2] \frac{\hat{\mathbf{r}}_{ij}}{r_{ij}} \right\} \end{aligned} \quad (\text{A3})$$

However, to derive eqn (A3) some care has to be taken upon differentiating  $\Psi$  with respect to  $\mathbf{r}_{ij}$  [see eqn (3.3) and (3.4)]. One can easily verify that

$$\frac{\partial}{\partial \mathbf{r}_{ij}} (\hat{\mathbf{u}}_i \cdot \hat{\mathbf{r}}_{ij}) = \frac{\partial}{\partial \mathbf{r}_{ij}} \frac{\hat{\mathbf{u}}_i \cdot \mathbf{r}_{ij}}{r_{ij}} = \frac{\hat{\mathbf{u}}_i - (\hat{\mathbf{u}}_i \cdot \hat{\mathbf{r}}_{ij}) \hat{\mathbf{r}}_{ij}}{r_{ij}} \quad (\text{A4})$$

resulting from  $\nabla P_2$ . Straightforward algebra then leads to the expressions on the second line of eqn (A3). From eqn (A1), (A2), and (A3) together with  $\hat{\mathbf{u}}_i^\alpha = \hat{\mathbf{u}}_i \cdot \hat{\mathbf{e}}_\alpha$  and  $\hat{r}_{ij}^\alpha = \hat{\mathbf{r}}_{ij} \cdot \hat{\mathbf{e}}_\alpha$

$$\begin{aligned} (\tau_{ff})_{\alpha\alpha} = & -\rho k_B T \\ & + \frac{24\varepsilon}{V} \left\langle \sum_{i=1}^N \sum_{j \neq i}^N \left[ \left( \frac{\sigma}{r_{ij}} \right)^{12} - \frac{1}{2} \left( \frac{\sigma}{r_{ij}} \right)^6 \Psi(\hat{\mathbf{r}}_{ij}, \hat{\mathbf{u}}_i, \hat{\mathbf{u}}_j) \right] \hat{r}_{ij}^\alpha \hat{r}_{ij}^\alpha \right\rangle \\ & + \frac{30\varepsilon\varepsilon_2}{V} \left\langle \sum_{i=1}^N \sum_{j \neq i}^N \left( \frac{\sigma}{r_{ij}} \right)^6 \left\{ (\hat{\mathbf{u}}_i \cdot \hat{\mathbf{r}}_{ij}) \hat{u}_i^\alpha \hat{r}_{ij}^\alpha + (\hat{\mathbf{u}}_j \cdot \hat{\mathbf{r}}_{ij}) \hat{u}_j^\alpha \hat{r}_{ij}^\alpha \right. \right. \\ & \left. \left. - [(\hat{\mathbf{u}}_i \cdot \hat{\mathbf{r}}_{ij})^2 + (\hat{\mathbf{u}}_j \cdot \hat{\mathbf{r}}_{ij})^2] \hat{r}_{ij}^\alpha \hat{r}_{ij}^\alpha \right\} \right\rangle, \quad \alpha = x, y \end{aligned} \quad (\text{A5})$$

Eqn (A5) is identical with eqn (9) and (10) of ref. 26 where unfortunately individual terms have been grouped together in a somewhat awkward and less transparent way.

### Acknowledgements

We are grateful for financial support from the International Graduate Research Training Group 1524 ‘‘Self-assembled soft-matter nanostructures at interfaces’’. In addition, we thank three anonymous referees for their supportive reviews and insightful comments that helped to improve the original presentation of our work considerably.

## References

- 1 F. Reinitzer, *Monatsh. Chem.*, 1888, **9**, 421.
- 2 O. Lehmann, *Z. Phys. Chem.*, 1889, **4**, 462.
- 3 P. G. de Gennes and J. Prost, *The Physics of Liquid Crystals*, Clarendon, Oxford, 1995.
- 4 I. A. Shanks, *Contemp. Phys.*, 1982, **23**, 65.
- 5 R. A. M. Hikmet and H. Kempermann, *Nature*, 1998, **392**, 476.
- 6 O. Guzmán, N. L. Abbott and J. J. de Pablo, *J. Chem. Phys.*, 2005, **122**, 184711.
- 7 A. Hussain, A. S. Pina and A. C. A. Roque, *Biosens. Bioelectron.*, 2009, **25**, 1.
- 8 S. V. Shiyankovskii, T. Schneider, I. I. Smalyukh, T. Ishikawa, G. D. Niehaus, K. J. Doane, C. J. Woolverton and O. D. Lavrentovich, *Phys. Rev. E: Stat., Nonlinear, Soft Matter Phys.*, 2005, **71**, 020702.
- 9 F.-J. Carrion, G. Martinez-Nicolas, P. Inglesias, J. Sanes and M.-D. Bermudez, *Int. J. Mol. Sci.*, 2009, **10**, 4102.
- 10 D. Kang, J. E. Maclennan, N. A. Clark, A. A. Zakhidov and R. H. Baughman, *Phys. Rev. Lett.*, 2001, **86**, 4052.
- 11 S. Juodzakis, V. Mizeikis and H. Misawa, *J. Appl. Phys.*, 2009, **106**, 051101.
- 12 W. Pisula, M. Zorn, J. Y. Chang, K. Müllen and R. Zentel, *Macromol. Rapid Commun.*, 2009, **30**, 1179.
- 13 S.-H. Yang and C.-S. Hsu, *J. Polym. Sci., Part A: Polym. Chem.*, 2009, **47**, 2713.
- 14 K. Larsson, *Curr. Opin. Colloid Interface Sci.*, 2009, **14**, 16.
- 15 J.-H. Kim, M. Yoneya and H. Yokoyama, *Nature*, 2002, **420**, 159.
- 16 S.-Y. Huang, S.-T. Wu and A. Y.-G. Fuh, *Appl. Phys. Lett.*, 2006, **88**, 041104.
- 17 L. E. Hough, H. T. Jung, D. Krüerke, M. S. Heberling, M. Nakata, C. D. Jones, D. Chen, D. R. Link, J. Zasadzinski, G. Heppke, J. P. Rabe, W. Stocker, E. Körblova, D. M. Walba, M. A. Glaser and N. A. Clark, *Science*, 2009, **325**, 456.
- 18 Z. Yang, Y. Lu and Z. Yang, *Chem. Commun.*, 2009, 2270.
- 19 T. Gruhn and M. Schoen, *J. Chem. Phys.*, 1998, **108**, 9124.
- 20 V. K. Gupta, J. J. Skaife, T. B. Dubrovsky and N. L. Abbott, *Science*, 1998, **279**, 2077.
- 21 J. J. Skaife and N. L. Abbott, *Langmuir*, 2000, **16**, 3529.
- 22 J. J. Skaife and N. L. Abbott, *Langmuir*, 2001, **17**, 5595.
- 23 M. Schoen, *Phys. A*, 1999, **270**, 353.
- 24 S. Hess and B. Su, *Z. Naturforsch.*, 1999, **54a**, 559.
- 25 H. Steuer, S. Hess and M. Schoen, *Phys. Rev. E: Stat., Nonlinear, Soft Matter Phys.*, 2004, **69**, 031708.
- 26 H. Steuer, S. Hess and M. Schoen, *Phys. A*, 2003, **328**, 322.
- 27 J. Jordanovic and S. H. L. Klapp, *Phys. Rev. Lett.*, 2008, **101**, 038302.
- 28 J. Jordanovic and S. H. L. Klapp, *Phys. Rev. E: Stat., Nonlinear, Soft Matter Phys.*, 2009, **79**, 021405.
- 29 M. Schoen and S. Klapp, *Nanoconfined fluids. Soft matter between two and three dimensions*, Wiley-VCH, New York, 2007.
- 30 C. G. Gray and K. E. Gubbins, *Theory of Molecular Fluids*, Vol. 1, Clarendon, Oxford, 1984.
- 31 D. Frenkel and B. Smit, *Understanding Molecular Simulation. From Algorithms to Applications*, Academic Press, London, 2002.
- 32 W. Maier and A. Saupe, *Z. Naturforsch.*, 1959, **14a**, 882.
- 33 W. Maier and A. Saupe, *Z. Naturforsch.*, 1960, **15a**, 287.
- 34 G. Vertogen and W. H. de Jeu, *Thermotropic liquid crystals, Fundamentals*, Springer, Berlin, 1988.
- 35 I. Pardowitz and S. Hess, *Phys. A*, 1980, **100**, 540.
- 36 R. Eppenga and D. Frenkel, *Mol. Phys.*, 1984, **52**, 1303.
- 37 W. H. Press, S. A. Teukolsky, W. T. Vetterling, and B. P. Flannery, *Numerical recipes in FORTRAN*, Cambridge University Press, Cambridge, 1989.
- 38 G. Morandi, F. Napoli, and E. Ercolessi, *Statistical Mechanics. An intermediate course*, World Scientific, Singapore, 2001.
- 39 A. Richter and T. Gruhn, *J. Chem. Phys.*, 2006, **125**, 064908.
- 40 J. V. Selinger, H. G. Jeon and B. R. Ratna, *Phys. Rev. Lett.*, 2002, **89**, 225701.
- 41 H. Finkelmann, E. Nishikawa, G. G. Pereira and M. Warner, *Phys. Rev. Lett.*, 2001, **87**, 015501.
- 42 D. L. Thomsen, P. Keller, J. Naciri, R. Pink, H. Jeon, D. Shenoy and B. R. Ratna, *Macromolecules*, 2001, **34**, 5868.
- 43 H. Weber, W. Paul and K. Binder, *Phys. Rev. E: Stat. Phys., Plasmas, Fluids, Relat. Interdiscip. Top.*, 1999, **59**, 2168.

## 4.3 Hybrid Slit-Pore

### 4.3.1 *Frustration of nanoconfined liquid crystals due to hybrid substrate anchoring*

Manuel Greschek<sup>a</sup> and Martin Schoen<sup>a,b</sup>

<sup>a</sup>Stranski-Laboratorium für Physikalische und Theoretische Chemie, Fakultät für Mathematik und Naturwissenschaften, Technische Universität Berlin, Straße des 17. Juni 135, D-10623 Berlin, Germany

<sup>b</sup>Department of Chemical and Biomolecular Engineering, Engineering Building I, Box 7905, North Carolina State University, 911 Partners Way, Raleigh, North Carolina 27695, USA

published in *Soft Matter* **6**, 4931 (2010)

## Frustration of nanoconfined liquid crystals due to hybrid substrate anchoring

Manuel Greschek<sup>a</sup> and Martin Schoen<sup>\*ab</sup>

Received 2nd April 2010, Accepted 19th July 2010

DOI: 10.1039/c0sm00197j

We present Monte Carlo simulations of liquid-crystalline material confined to a nanoscopic slit-pore. The simulations are carried out under isothermal conditions in a specialized isostress ensemble in which  $N$  fluid molecules are exposed to a compressional stress  $\tau_{\parallel}$  acting on the fluid in directions parallel with the substrate planes. Fluid-fluid and fluid-substrate interactions are modelled as in our previous work (M. Greschek *et al.*, *Soft Matter*, 2010, **6**, 1898). We study several anchoring mechanisms at the solid substrate by introducing an anchoring function  $0 \leq g(\hat{\mathbf{u}}) \leq 1$  that depends on the orientation  $\hat{\mathbf{u}}$  of a fluid molecule relative to the substrate plane;  $g(\hat{\mathbf{u}})$  “switches” the fluid-substrate attraction on or off. Here we focus on various *heterogeneous* (i.e., hybrid) anchoring scenarios imposing different anchoring functions at the opposite substrates. As in our previous study we compute the isostress heat capacity which allows us to identify states at which the confined fluid undergoes a structural transformation. The isotropic-nematic transformation turns out to be nearly independent of the specific anchoring scenario. This is because the director in the nematic phase assumes a direction that is a compromise between the directions enforced by the competing anchoring scenarios at either substrate. On the contrary, at lower compressional stresses molecules prealign near the slit-pore’s midplane in specific directions that depend on details of the anchoring scenario.

### I. Introduction

If a liquid crystal is in its nematic phase specific orientations of the director [i.e., the (unit) vector  $\hat{\mathbf{n}}$  with which molecules align preferentially] can be realized through specific anchoring scenarios at a solid substrate. The substrate-induced alignment can be perturbed if an external field is superimposed such that it is competing with the director. An example is the so-called Fréedericksz cell in which a nematic liquid crystal is exposed to a magnetic field pointing in a direction other than that in which molecules are anchored at the walls of the cells.<sup>1,2</sup> If the external field is sufficiently strong and if the substrate separation is large enough there will be a region in the liquid crystal where the local director points in another direction than that enforced by substrate anchoring. In other words, the orientational order in the nematic phase is perturbed by the presence of the external field. Because the correlation lengths of these perturbations may be substantial they can be used in sensor applications. This was recently demonstrated by Guzmán *et al.* who considered a model for a bionanosensor based upon a confined liquid-crystalline phase.<sup>3</sup> The sensor consists of thin films of liquid-crystalline materials squeezed between substrate surfaces with specific anchoring characteristics. If particles such as proteins or viruses bind to these solid surfaces they give rise to long-range perturbations of the orientational order in a nematic phase that reports the binding of these particles at specific receptors on the solid surfaces.<sup>4–6</sup> The binding process perturbs the local

structure of the liquid-crystal phase over sufficiently long distances so that optical methods can be used to detect the perturbation.

The apparent importance of substrate anchoring for the nematic phase of such nanoconfined liquid crystals prompted us to investigate the impact of various anchoring scenarios on the isotropic-nematic (IN) transformation in a model liquid crystal of prolate ellipsoids of revolution confined to a nanoscopic slit-pore.<sup>7</sup> Our results indicate that the nature of the anchoring at the substrate has a pronounced effect on the location of the IN transition and on structural details associated with it. In view of our earlier results it thus seems interesting to replace in this work the original *homogeneous* by *heterogeneous* (or “hybrid”) anchoring scenarios where the anchoring is different at the opposite substrates forming the slit-pore. This will cause the director field to be inhomogeneous such that interesting new physical phenomena are anticipated.

That heterogeneous or competing fluid-wall interactions can lead to exciting effects and interesting new physics has already been demonstrated in the past in several contexts. Perhaps the best-known example is the localization-delocalization transition that occurs for the gas-liquid interface in fluids confined between two planar walls where one wall favors the liquid- and the other one favors the gas-like phase.<sup>8–10</sup> If the substrate is nonplanar such as in the bi-pyramid considered by Milchev *et al.*<sup>11</sup> competing surface fields can cause the spontaneous magnetization in an Ising magnet to vanish at a filling temperature  $T_f$  below the bulk critical temperature  $T_{cb}$ ; the spontaneous magnetization remains zero for all  $T \geq T_f$ .

In the context of liquid crystals some attention has already been paid to hybrid anchoring scenarios which are particularly important for optical applications.<sup>12,13</sup> For example, Schmid and Cheung employ Landau-de Gennes theory to study the interplay between wetting and anchoring of nematic liquid crystals.<sup>14</sup>

<sup>a</sup>Stranski-Laboratorium für Physikalische und Theoretische Chemie, Fakultät für Mathematik und Naturwissenschaften, Technische Universität Berlin, Straße des 17. Juni 135, 10623 Berlin, Germany. E-mail: martin.schoen@tu-berlin.de

<sup>b</sup>Department of Chemical and Biomolecular Engineering, Engineering Building I, North Carolina State University, Box 7905, 911 Partners Way, Raleigh, NC, 27695, USA

Using lattice Boltzmann simulations Marenduzzo *et al.* consider the impact of hybrid anchoring on the rheology of nematic liquid crystals in nonequilibrium situations.<sup>15</sup> In another study, Zihlerl *et al.* consider a situation in which the molecules of a liquid crystal are aligned homeotropically at one wall and planar at the opposite such that in the nematic phase molecules appear to be frustrated with respect to the direction of  $\hat{n}$ .<sup>2</sup> The authors focus on the impact of this frustration on fluctuation-induced forces that can be interpreted as an analogue of the well-known Casimir forces in quantum systems.<sup>16</sup> For the same hybrid anchoring scenario Rodríguez-Ponce *et al.* employ mean-field density functional theory and observe a linear variation of the tilt angle between the local director field and the substrate normal (see also Ref. 17) as far as strong anchoring at the substrate is concerned.<sup>18</sup> Such a linear variation of the tilt-angle profile has also been reported by Steuer *et al.*<sup>19</sup> for hybrid anchoring corresponding to a nanoscopic twisted nematic cell and for the same model system used in this work. However, to date a systematic molecular study of the impact of hybrid anchoring on the IN transition is still lacking. Nevertheless, Harnau *et al.* investigate the phase behavior of a nematic liquid crystal in contact with chemically patterned nonplanar substrates where the pattern consists of alternating stripes that anchor molecules in a parallel and homeotropic fashion.<sup>20,21</sup> Based upon the (continuum) Frank-Oseen model they observe a rich phase behavior depending on details of the substrate structure. A related model has been investigated by Harnau and Dietrich which is based upon the well-known Frank elastic free energy amended by terms representing dielectric electrostatic and flexoelectric free energy contributions.<sup>22</sup> Applying a voltage allows these authors to switch between a homeotropically and a hybrid-anchored state in the nematic phase.

Experimentally, hybrid anchoring scenarios can be realized in a number of ways. For example, Chung *et al.* use photoalignment to fabricate planar substrates where the anchoring at each substrate differs by an angle of  $\pi/4$ .<sup>23</sup> They show that the resulting molecular orientation in a confined liquid crystal can be controlled by the photoirradiation time. The same authors show that very similar results can be obtained if the surfaces are rubbed in specific directions and under controlled conditions. Zappone *et al.* perform experiments using the surface forces apparatus (SFA) to measure the solvation force in nematic liquid crystals under hybrid anchoring conditions.<sup>24</sup> They set up a hybrid (homeotropic-planar) anchoring scenario by dipping muscovite mica surfaces, with which the crossed cylinders in the SFA setup are coated, in various cationic surfactant solutions where the surfactants differ only in the length of the aliphatic chains.

In this work we study the impact of various hybrid anchoring scenarios on properties of nanoconfined model liquid crystals by means of Monte Carlo simulations in a specialized isostress ensemble used in our previous study.<sup>7</sup> Our emphasis is on structural changes arising in the confined phase as the transverse compressional stress  $\tau_{\parallel}$  increases. Increasing  $\tau_{\parallel}$  eventually drives the system from an isotropic to a nematic phase. We have organized the remainder of our manuscript such that we briefly describe the model system in Sec. II. Our results are presented in Sec. III and summarized and discussed in the concluding Sec. IV.

## II. The model system

### A. Interaction potentials

The model liquid crystal considered in this work is confined to a mesoscopic slit-pore such that we may decompose the total configurational energy into a fluid-fluid (ff) and into a fluid-substrate (fs) contribution according to

$$U(\mathbf{R}, \hat{\mathbf{U}}) = U_{\text{ff}}(\mathbf{R}, \hat{\mathbf{U}}) + U_{\text{fs}}(\mathbf{R}, \hat{\mathbf{U}}) \quad (2.1)$$

where  $\mathbf{R} \equiv \{\mathbf{r}_1, \mathbf{r}_2, \dots, \mathbf{r}_N\}$  and  $\hat{\mathbf{U}} \equiv \{\hat{\mathbf{u}}_1, \hat{\mathbf{u}}_2, \dots, \hat{\mathbf{u}}_N\}$  are shorthand notations for the sets of center-of-mass coordinates and unit vectors specifying the orientations of the  $N$  liquid-crystalline molecules, respectively. More specifically,

$$U_{\text{ff}}(\mathbf{R}, \hat{\mathbf{U}}) = \frac{1}{2} \sum_{i=1}^N \sum_{j=1 \neq i}^N u_{\text{ff}}(\mathbf{r}_{ij}, \hat{\mathbf{u}}_i, \hat{\mathbf{u}}_j) \quad (2.2)$$

where  $\mathbf{r}_{ij} \equiv \mathbf{r}_i - \mathbf{r}_j$  is the distance vector between the centers of mass of particles  $i$  and  $j$  assuming pairwise additivity of their interactions. We take  $u_{\text{ff}}$  as<sup>7</sup> (see also Ref. 25)

$$u_{\text{ff}}(\mathbf{r}_{ij}, \hat{\mathbf{u}}_i, \hat{\mathbf{u}}_j) = 4\epsilon \left[ \left( \frac{\sigma}{r_{ij}} \right)^{12} - \left( \frac{\sigma}{r_{ij}} \right)^6 \left\{ 1 + \Psi(\hat{\mathbf{r}}_{ij}, \hat{\mathbf{u}}_i, \hat{\mathbf{u}}_j) \right\} \right] \quad (2.3)$$

where  $r = |\mathbf{r}|$ , and  $\hat{\mathbf{r}} = \mathbf{r}/r$ . Hence,  $u_{\text{ff}}$  is a Lennard-Jones potential where the attractive contribution is modified to account for different orientations of a pair of molecules. In eqn (2.3),  $\sigma$  denotes the ‘‘diameter’’ of a spherical reference molecule and  $\epsilon$  is the depth of the attractive well in that reference model. The anisotropy of the fluid-fluid interaction is accounted for by the function

$$\Psi(\hat{\mathbf{r}}_{ij}, \hat{\mathbf{u}}_i, \hat{\mathbf{u}}_j) = 5\epsilon_1 P_2(\hat{\mathbf{u}}_i \cdot \hat{\mathbf{u}}_j) + 5\epsilon_2 [P_2(\hat{\mathbf{u}}_i \cdot \hat{\mathbf{r}}_{ij}) + P_2(\hat{\mathbf{u}}_j \cdot \hat{\mathbf{r}}_{ij})] \quad (2.4)$$

where we take  $\epsilon_1 = 0.04$  and  $\epsilon_2 = -0.08$ .<sup>7</sup> As we have demonstrated earlier (see Fig. 1 of Ref. 7) our molecules turn out to be prolate ellipsoids of revolution with an aspect ratio corresponding to 1.26. The function  $\Psi$  preserves the head-tail symmetry of our molecules, that is orientations  $\hat{\mathbf{u}}_i$  and  $-\hat{\mathbf{u}}_i$  are equivalent. In eqn (2.4)

$$P_2(x) = \frac{1}{2}(3x^2 - 1) \quad (2.5)$$

is the second Legendre polynomial. To model the fluid-substrate contribution to  $U$  we follow earlier work<sup>7,19</sup> and introduce

$$U_{\text{fs}}(\mathbf{R}, \hat{\mathbf{U}}) = \sum_{k=1}^2 \sum_{i=1}^N u_{\text{fs}}^{[k]}(\mathbf{r}_i, \hat{\mathbf{u}}_i) \quad (2.6)$$

where

$$u_{\text{fs}}^{[k]}(z_i, \hat{\mathbf{u}}_i) = 2\pi\epsilon\rho_s\sigma^2 \left[ \frac{2}{5} \left( \frac{\sigma}{z_i \pm s_{z0}/2} \right)^{10} - \left( \frac{\sigma}{z_i \pm s_{z0}/2} \right)^4 g^{[k]}(\hat{\mathbf{u}}_i) \right] \quad (2.7)$$

In eqn (2.7),  $z_i$  is the  $z$ -coordinate of the center-of-mass position of molecule  $i$  in a space-fixed Cartesian coordinate system. In this coordinate system we assume the lower substrate ( $k = 1$ ) to be located at  $z_w = -s_{z0}/2$  whereas the upper one is located at  $z_w = +s_{z0}/2$  ( $k = 2$ ). In other words, eqn (2.7) assumes the

substrates to be structureless such that at fixed molecular orientation  $u_{fs}$  depends only on the distance of molecule  $i$  from either substrate along the  $z$ -axis. In the prefactor the areal density of the solid substrates  $\rho_s = 2/\ell^2$  where  $\ell/\sigma = \sqrt[3]{4}$  is the lattice constant of a single (100) plane of a face-centred cubic lattice.

### B. Anchoring scenarios

In eqn (2.7),  $0 \leq g^{(k)}(\hat{\mathbf{u}}_i) \leq 1$  is the so-called anchoring function. Choosing different functional forms the anchoring function permits to realize different, energetically favorable orientations of molecule  $i$  with respect to the substrate plane. Specifically, we take  $g^{(k)}(\hat{\mathbf{u}}_i)$  to be given by one of the following expressions:

$$g_0(\hat{\mathbf{u}}) = 1 \quad (2.8a)$$

$$g_{\perp}(\hat{\mathbf{u}}) = (\hat{\mathbf{u}} \cdot \hat{\mathbf{e}}_z)^2 \quad (2.8b)$$

$$g_{\parallel}(\hat{\mathbf{u}}) = (\hat{\mathbf{u}} \cdot \hat{\mathbf{e}}_x)^2 + (\hat{\mathbf{u}} \cdot \hat{\mathbf{e}}_y)^2 \quad (2.8c)$$

$$g_x(\hat{\mathbf{u}}) = (\hat{\mathbf{u}} \cdot \hat{\mathbf{e}}_x)^2 \quad (2.8d)$$

Where  $\hat{\mathbf{e}}_{\alpha}$  is a unit vector pointing along the  $\alpha$ -axis of the Cartesian coordinate system.

The anchoring functions given in eqn (2.8) have the following physical significance. As we rationalize elsewhere,<sup>7</sup> if  $g^{(k)}(\hat{\mathbf{u}})$  is given by  $g_0(\hat{\mathbf{u}})$  molecules orient themselves in a homeotropic fashion at the substrates even though the substrates themselves do not discriminate any molecular orientation energetically. Employing the expression given in eqn (2.8b) also results in homeotropic alignment which is, however, stronger than the one induced by  $g_0(\hat{\mathbf{u}})$  because the substrates explicitly favor homeotropic alignment. To overcome the homeotropic alignment already supported by the mere presence of the substrate we also consider the anchoring functions specified in eqn (2.8c) and (2.8d). In both cases a planar orientation parallel with the substrate plane is energetically favored. The difference is that by employing eqn (2.8c) any orientation of a molecule parallel with the substrate plane is energetically favorable whereas eqn (2.8d) selects those orientations where  $\hat{\mathbf{u}}$  is aligned with the  $x$ -axis. We shall distinguish *homogeneous* anchoring scenarios where  $g^{(1)}(\hat{\mathbf{u}}_i) = g^{(2)}(\hat{\mathbf{u}}_i)$  from *heterogeneous* (i.e., “hybrid”) ones characterized by  $g^{(1)}(\hat{\mathbf{u}}_i) \neq g^{(2)}(\hat{\mathbf{u}}_i)$  (see Table I).

## III. Results

### A. Numerical details

As in our previous study<sup>7</sup> we employ Monte Carlo simulations in a specialized isostress ensemble in which the fluid is exposed to

**Table 1** Hybrid anchoring scenarios employed in this work

$g^{(k)}(\hat{\mathbf{u}})$		anchoring scenario	acronym
$k = 1$	$k = 2$		
$g_{\perp} \hat{\mathbf{u}}$	$g_{\parallel} \hat{\mathbf{u}}$	homeotropic-planar	<i>hp</i>
$g_0 \hat{\mathbf{u}}$	$g_{\parallel} \hat{\mathbf{u}}$	nonspecific-planar	<i>np</i>
$g_0 \hat{\mathbf{u}}$	$g_x \hat{\mathbf{u}}$	nonspecific-directional	<i>nd</i>

a constant compressional stress in directions parallel with the substrate planes. We employ periodic boundary conditions in the  $x$ - and  $y$ -directions. To generate a Markov chain of configurations in this ensemble we utilize the algorithm described in Sec. 4.1 of Ref. 26. We refer to a Monte Carlo cycle as a sequence of  $N$  attempted displacements and rotations of sequentially selected fluid particles plus one attempted change of the  $z$ -directed area  $A$  of the computational cell. Typical runs comprise  $10^5$  Monte Carlo cycles in regions where the fluid does not undergo an IN transformation; in the immediate vicinity of such a transformation the length of a typical run was enlarged to  $3 \times 10^6$  Monte Carlo cycles to guarantee sufficient statistical accuracy.

We express all quantities of interest in terms of the customary dimensionless (i.e., “reduced”) units. For example, length is given in units of  $\sigma$ , energy in units of  $\epsilon$ , and temperature in units of  $\epsilon/k_B$ . Other derived quantities are expressed in terms of suitable combinations of these basic quantities. For example, stress is given in units of  $\epsilon/\sigma^3$ . Throughout this work we fix the temperature  $T = 1.0$  which should be sufficiently subcritical taking the mean-field bulk phase diagram of Hess and Su as a rough guidance.<sup>25</sup> Our systems comprise  $N = 3000$  fluid molecules which we equilibrate during an initial  $10^4$  Monte Carlo cycles. To save computer time we cut off fluid-fluid interactions beyond a separation of  $r_c = 3.0$  between the centers-of-mass of a pair of fluid molecules. In addition, we employ a linked-cell in combination with a conventional (Verlet) neighbor list as described in the book by Allen and Tildesley to further speed up the simulations (see Chap. 5.3 of Ref. 27). This list includes all particles as neighbors whose centers-of-mass are located within a distance of  $r_n = 3.5$  from a reference molecule at the origin of the neighbor sphere.

The simulations of this work are carried out for a substrate separation  $s_{z0} = 20$ . This value has been chosen because then our confined fluid contains a sufficiently large region centered around the middle of the slit-pore in which fluid molecules do not interact with either of the two substrates. This is illustrated by plots in Fig. 1 indicating that  $u_{fs}^{(1)}(z, \hat{\mathbf{u}}) + u_{fs}^{(2)}(z, \hat{\mathbf{u}}) \lesssim 3 \times 10^{-3}$  for distances  $\Delta z \approx 4$  from either substrate surfaces.

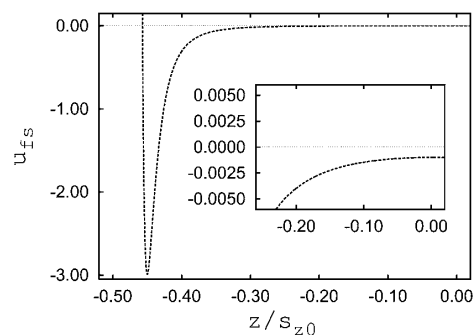


**Fig. 1** Plot of  $u_{fs}(z, \hat{\mathbf{u}}) = u_{fs}^{(1)}(z, \hat{\mathbf{u}}) + u_{fs}^{(2)}(z, \hat{\mathbf{u}})$  as a function of position  $z/s_{z0}$  in the lower half of the system ( $z/s_{z0} \leq -0.5$ ) for  $s_{z0} = 20$ . The plots are symmetric with respect to the line  $z = 0$  and were obtained assuming  $g^{(1)}(\hat{\mathbf{u}}) = g^{(2)}(\hat{\mathbf{u}}) = 1$ . The inset shows an enlargement of the plot.

### B. Properties

To investigate the impact of the various hybrid anchoring scenarios introduced in Sec. II B we introduce in the following some key properties on which we shall base our subsequent discussion. The most important one is the so-called alignment tensor<sup>28</sup>

$$\mathbf{Q} \equiv \frac{1}{2N} \sum_{i=1}^N (3\hat{\mathbf{u}}_i \otimes \hat{\mathbf{u}}_i - \mathbf{1}) \quad (3.1)$$

where “ $\otimes$ ” denotes the direct (*i.e.*, dyadic) product and  $\mathbf{1}$  is the unit tensor. The alignment tensor can be represented by a real, symmetric, traceless,  $3 \times 3$  matrix that can be diagonalized numerically using Jacobi’s method.<sup>29</sup> For a system with biaxial symmetry it can be shown that the diagonalized alignment tensor can be written as

$$\text{diag } \mathbf{Q} \equiv \begin{pmatrix} -\lambda_m/2 - \zeta & 0 & 0 \\ 0 & -\lambda_m/2 + \zeta & 0 \\ 0 & 0 & \lambda_m \end{pmatrix} \quad (3.2)$$

This expression was derived by Low who uses an expansion in terms of Wigner matrices.<sup>30</sup> Following previous workers<sup>7,31,32</sup> we adopt  $S \equiv \langle \lambda_m \rangle$  as a definition of the Maier-Saupe nematic order parameter<sup>33,34</sup> where the angular brackets denote an ensemble average in the specialized isostress ensemble. Once the largest eigenvalue of  $\mathbf{Q}$  is known one may compute  $\zeta$  from eqn (3.2) and with it the biaxial order parameter  $\xi \equiv \langle \zeta \rangle$ .

Other structural quantities that we shall be considering below take notice of the anisotropy and inhomogeneity of liquid crystals in confinement. The simplest one of these is the local density of the confined fluid defined as

$$\rho(z) = \left\langle \sum_{i=1}^N \delta(z - z_i) \right\rangle = \frac{1}{\delta z} \left\langle \frac{N(z)}{A} \right\rangle \quad (3.3)$$

where  $\delta(z - z_i)$  is the Dirac  $\delta$ -function and  $N(z)$  is the number of molecules within a small interval  $\delta z$  centered on  $z$ . In addition, we consider the *local* nematic order parameter  $S(z)$  which we compute from an expression for  $\mathbf{Q}(z)$  analogous to eqn (3.1) replacing, however,  $\hat{\mathbf{u}}_i$  and  $N$  by their local counterparts  $\hat{\mathbf{u}}_i(z)$  and  $N(z)$ , respectively. However, to gain even deeper insight into the nature of nematic phases it turns out to be useful to consider another measure of local nematic order provided by the (local value of the) second Legendre polynomial

$$P_2(z) \equiv \frac{1}{2} \left\langle \frac{1}{N(z)} \sum_{i=1}^{N(z)} [3(\hat{\mathbf{u}}_i(z) \cdot \hat{\mathbf{e}}_z)^2 - 1] \right\rangle \quad (3.4)$$

where  $N(z)$  has the same meaning as in eqn (3.3). Hence,  $P_2(z) = 1$  if all molecules within the interval  $[z - \delta z/2, z + \delta z/2]$  are homeotropically aligned ( $|\hat{\mathbf{u}}_i \cdot \hat{\mathbf{e}}_z| = 1$ ). If, on the other hand, these molecules are aligned in a perfectly parallel fashion  $P_2(z) = -0.5$  ( $|\hat{\mathbf{u}}_i \cdot \hat{\mathbf{e}}_z| = 0$ ). Notice, that in writing eqn (3.4) we *assume*  $\hat{\mathbf{n}}$  to point along the  $z$ -axis  $\hat{\mathbf{e}}_z$  of a space-fixed Cartesian coordinate system whereas the true direction of the *local* director  $\hat{\mathbf{n}}(z)$  computed as an eigenvector of  $\mathbf{Q}(z)$  is unrestricted. Local quantities such as  $\rho(z)$ ,  $P_2(z)$ , and  $\mathbf{Q}(z)$  are computed as histograms where a bin width of  $\delta z = 0.1$  is employed throughout.

In addition to these structural quantities we compute a specialized isostress heat capacity

$$c_\tau = \frac{5}{2} k_B + \frac{\langle \mathcal{H}^2 \rangle - \langle \mathcal{H} \rangle^2}{Nk_B T^2} \quad (3.5)$$

and the isothermal compressibility

$$\kappa_T = \frac{s_{z0}}{k_B T} \frac{\langle A^2 \rangle - \langle A \rangle^2}{\langle A \rangle} \quad (3.6)$$

that we already introduced in our previous study.<sup>7</sup> As we demonstrated there,  $c_\tau$  and  $\kappa_T$  are particularly useful to identify characteristic stresses at which the confined liquid crystal may undergo subtle structural transformations. In eqn (3.5)

$$\mathcal{H}(\mathbf{R}, \hat{\mathbf{U}}) \equiv U(\mathbf{R}, \hat{\mathbf{U}}) - \tau_{\parallel} A s_{z0} \quad (3.7)$$

such that  $\langle \mathcal{H} \rangle$  is a specialized enthalpy.

### C. Heat capacity and global order parameters

We begin our discussion with plots of  $c_\tau$  as a function of applied compressional stress and various homogeneous and hybrid anchoring scenarios in Fig. 2. The isotress heat capacity exhibits pronounced peaks at sufficiently large compressional stress. As we have already demonstrated in our previous work, maxima of  $c_\tau$  are fingerprints of an IN transformation in the confined phase. Therefore, the stresses at which these maxima are located depend on the specific homogeneous anchoring scenario. For example, the plot in Fig. 2(a) shows that the IN transformation occurs at lower compressional stress  $|\tau_{\parallel}| \approx 1.50$  for the homogeneous homeotropic compared with  $|\tau_{\parallel}| \approx 1.60$  for the homogeneous planar anchoring scenario. Moreover, these IN transformations occur at somewhat lower stresses than  $|\tau_{\parallel}| \approx 1.70$  observed in the bulk under identical thermodynamic conditions (see, for example, Fig. 4.3(a) of Ref. 7). This reflects the supportive character of the solid substrate in the formation of nematic phases as far as homogeneous anchoring is concerned. Note that in our previous study<sup>7</sup> we have been unable to observe an IN transition for the (homogeneous) homeotropic anchoring scenario because at the smaller pore width  $s_{z0} = 10$  considered there the impact of the walls is so strong that even at vanishingly small compression almost the entire confined fluid is already in a nematic state. As we also explained earlier the height of peaks in the plots of  $c_\tau$  reflect a loss of rotational entropy at the IN transition which is different for different anchoring scenarios (see Sec. V of Ref. 7).

Comparing results for the two homogeneous anchoring scenarios in Fig. 2(a) with the corresponding hybrid (*hp*) one two main differences can be recognized. First, the dominant peak in  $c_\tau$  is shifted to a compressional stress  $|\tau_{\parallel}| \approx 1.75$  exceeding that characteristic of the two homogeneous anchoring scenarios. Obviously, the heterogeneity of the anchoring at the two substrates inhibits the formation of nematic phases. This seems quite striking at first in view of the fact that the *direct* impact of the solid substrates is restricted to a distance of about  $\Delta z \approx 4$  from either substrate surface as plots in Fig. 1 suggest. However, one has to keep in mind that nematic phases are characterized by *long-range* orientational order. Molecules of the confined soft-matter phase are therefore cooperative in transmitting the

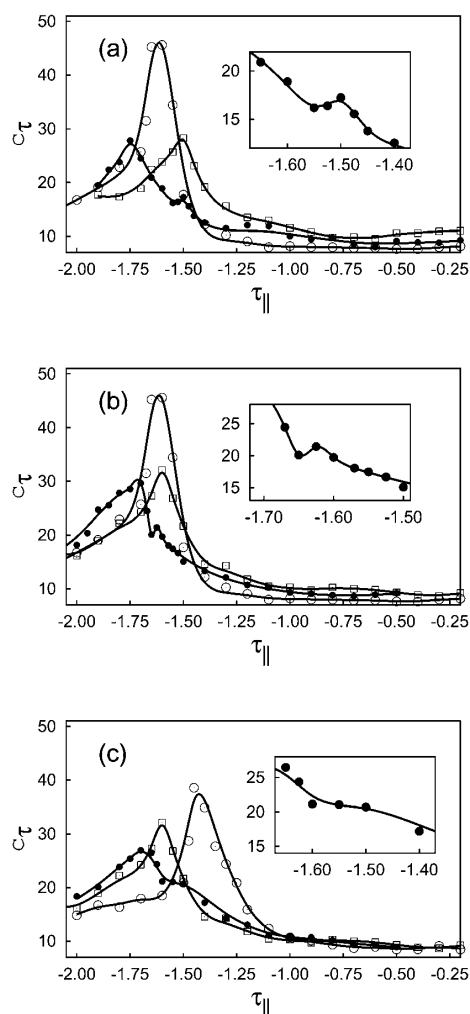


**Fig. 2** Isostress heat capacity  $c_t$  as a function of compressional stress  $\tau_{\parallel}$  for various homogeneous ( $\square$ ,  $\circ$ ) and corresponding hybrid ( $\bullet$ ) anchoring scenarios. (a) Homeotropic ( $\square$ ), planar ( $\circ$ ). (b) Nonspecific ( $\square$ ), planar ( $\circ$ ). (c) Nonspecific ( $\square$ ), directional ( $\circ$ ). Insets are enlargements of plots for hybrid anchoring scenarios. Solid lines are fits intended to guide the eye.

specific orientation *imprinted* by a solid substrate over distances substantially exceeding the range of the fluid-substrate interaction itself. The inhibition of the IN transition in the hybrid anchoring scenario may therefore be interpreted as frustration of the molecules in the confined phase which are trying to adjust their orientation with respect to the two conflicting anchoring conditions simultaneously. The structural frustration is illustrated in Fig. 3 where we show a “snapshot” of a representative molecular configuration taken from the Monte Carlo simulations. Similar structural frustration has been reported by Steurer *et al.* for the twisted nematic cell (see Fig. 11 of Ref. 19) and by Harnau and coworkers<sup>20,22</sup> despite the use of a continuum approach and differences in both the physical nature of their

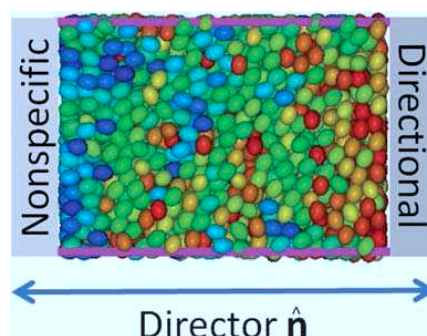


**Fig. 3** “Snapshot” of a representative configuration in the nematic phase. Gray boxes indicate the position of the substrates in the  $x$ - $z$  plane where the specific anchoring scenario is indicated within each box. The purple lines indicate the (virtual) boundaries of the simulation cell at which periodic boundary conditions are applied. The sequence blue  $\rightarrow$  green  $\rightarrow$  red refers to a change in molecular orientation from parallel to perpendicular with  $\hat{n}$  deliberately taken to coincide with  $\hat{e}_z$ .

systems and the hybrid anchoring scenarios considered by these latter authors.

A second interesting feature visible in the plot of  $c_t$  in Fig. 2(a) for the hybrid anchoring is a smaller but significant secondary peak that occurs at lower compressional stress  $|\tau_{\parallel}| \approx 1.50$  compared with the main peak at  $|\tau_{\parallel}| \approx 1.75$ . The existence of this secondary peak has been verified in Monte Carlo runs in which we enlarged the number of cycles up to  $3 \times 10^6$  while carefully monitoring the evolution of  $c_t$  as a function of the number of cycles similar to plots presented in Fig. 4.2 of Ref. 7. Comparing the plots for hybrid and homogeneous homeotropic alignment in Fig. 2(a) reveals that the secondary peak in the plots of  $c_t$  for the hybrid anchoring coincides with that in the corresponding curve for the homogeneous homeotropic alignment. The origin of the secondary peak will become clear in Sec. III D where we discuss local structural features of the confined liquid crystals.

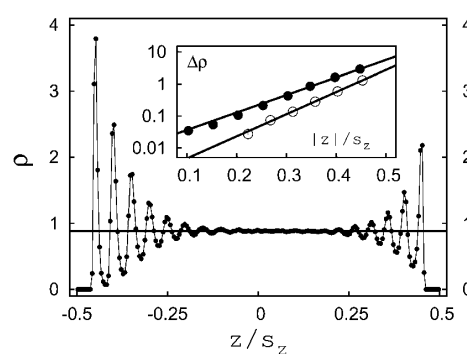


**Fig. 4** Plot of  $\rho(z)$  for the  $hp$  anchoring scenario at  $|\tau_{\parallel}| = 2.00$  where homeotropically and planar anchoring substrate are located at  $z_q/s_z = -0.5$  and  $+0.5$ , respectively. The horizontal thick solid line corresponds to  $\bar{\rho}$  in the bulk-like region of the confined phase. Inset shows a plot of  $\Delta\rho$  where straight lines are fits of the far right side of eqn (3.8) to  $\rho(z_m)$  (see text) near the homeotropically ( $\bullet$ ) and planar ( $\circ$ ) anchoring substrate.

For the *hp* anchoring scenario we also investigated the local density  $\rho(z)$  [see eqn (3.3)] for a state point in the nematic phase. The plot in Fig. 4 shows that in the confined liquid crystal molecules arrange themselves in individual layers in the vicinity of either substrate indicated by the oscillatory character of  $\rho(z)$  in the vicinity of the substrates. As one moves towards the midplane of the slit-pore the fluid becomes almost homogeneous (*i.e.*, bulk-like) such that  $\lim_{z \rightarrow 0} \rho(z) \approx \bar{\rho} \approx 0.88$  where  $\bar{\rho}$  is the mean density of the bulk-like region. However, as we shall demonstrate below in Fig. 5 closer scrutiny reveals weak oscillations of  $\rho(z)$  around  $\bar{\rho}$  that persist as  $|z| \rightarrow 0$ . As long as the confined liquid crystal is fluidic one expects

$$\Delta\rho \equiv \rho(z_m) - \bar{\rho} = a \exp(z_m/\xi_0) \cos(\xi_1 z_m - \theta) \xrightarrow{\xi_1 \rightarrow 0} a \exp(z_m/\xi_0) \quad (3.8)$$

where  $z_m$  is the position of peaks in the plot of  $\rho(z)$ . The correlation lengths  $\xi_0$  and  $\xi_1$  are determined by bulk properties whereas  $a$  and  $\theta$  depend on the specific nature of the fluid-substrate interactions.<sup>35</sup> Note, however, that eqn (3.8) holds strictly only for spherically symmetric molecules but is *assumed* here to be approximately valid because our system is composed of weakly anisometric molecules. A fit of eqn (3.8) to  $\rho(z_m)$  gives  $\xi_1 \approx 0$  and  $\theta \approx \pi/2$  such that the far right side of the equation provides an excellent representation of our data (see inset in Fig. 4). Moreover, the fit yields  $\xi_0^\pm \approx 1.5859$  near the homeotropically anchoring substrate and  $\xi_0^\parallel \approx 1.2544$  near the planar anchoring one. The ratio  $\xi_0^\pm/\xi_0^\parallel \approx 1.26$  is nearly identical with the aspect ratio of the ellipsoidal fluid molecules as one would have anticipated.

As we already explained above the homogeneous nonspecific anchoring scenario favors a homeotropic alignment of the molecules in the nematic phase as well. However, as one can see from the corresponding plots in Fig. 2(b) the maximum in the plot of  $c_\tau$  for this anchoring scenario is shifted to higher compressional stress  $|\tau_{\parallel}| \approx 1.60$  compared with its counterpart for homogeneous homeotropic anchoring in Fig. 2(a). This indicates that the substrates for the nonspecific homogeneous

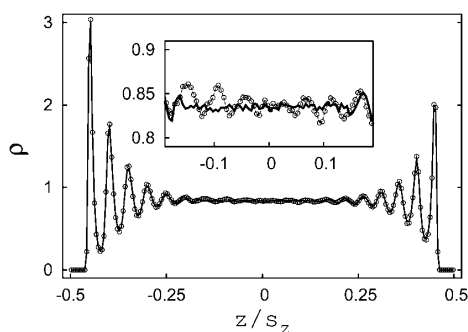


**Fig. 5** As Fig. 4, but for  $\tau_{\parallel} = -1.45$  (—) and  $\tau_{\parallel} = -1.55$  (○) [cf., Fig. 2(a)]. Inset is an enhancement of the plot focusing on the portion of the confined fluid at the center of the slit-pore. The weak oscillatory behavior of  $\rho(z)$  around  $z = 0$  persists for all larger compressional stresses (cf., Fig. 4).

anchoring scenario are somewhat less supportive in the formation of nematic phases. In fact, in the present case maxima of  $c_\tau$  for the two homogeneous (nonspecific and planar) anchoring scenarios are located at about the same compressional stress as the plots in Fig. 2(b) indicate.

The plot of  $c_\tau$  for the *np* anchoring scenario exhibits qualitatively the same features already observed in Fig. 2(a) for the *hp* anchoring scenario. That is  $c_\tau$  exhibits a main maximum at a larger compressional stress  $|\tau_{\parallel}| \approx 1.70$  and a smaller secondary maximum at about  $|\tau_{\parallel}| \approx 1.63$ . The shift of the secondary peak from  $|\tau_{\parallel}| \approx 1.50$  [*hp* anchoring, see Fig. 2(a)] to  $|\tau_{\parallel}| \approx 1.63$  [*np* anchoring, see Fig. 2(b)] is more pronounced than the shift of the associated main peaks in the heat-capacity curves. Notice also that the location of the secondary maximum in the plot of  $c_\tau$  for the two hybrid anchoring scenarios in Fig. 2(a) and 2(b) correlates nicely with the values  $|\tau_{\parallel}| \approx 1.50$  and  $|\tau_{\parallel}| \approx 1.60$  for the homogeneous homeotropic and nonspecific anchoring scenarios, respectively. This suggests that the secondary peak visible in the plots of  $c_\tau$  for the two hybrid anchoring scenarios in Fig. 2(a) and 2(b) reflects an increase in homeotropic orientation of the molecules prior to the IN transformation. This notion is supported by a more detailed analysis of local structural features presented below in Sec. III.D.

However, before turning to that discussion it is instructive to consider *nd* as yet another hybrid anchoring scenario. As plots in Fig. 2(c) show the maximum in  $c_\tau$  for the *homogeneous* directional anchoring occurs at a compressional stress of about  $|\tau_{\parallel}| \approx 1.45$  which is the smallest value of the three homogeneous anchoring scenarios considered in this study. This indicates that directional (planar) anchoring is the most supportive scenario in the formation of nematic phases in confined liquid crystals. Combining directional with nonspecific anchoring causes the small but pronounced secondary peak in the plots of  $c_\tau$  in Fig. 2(a) and 2(b) to give way to a broad shoulder at about  $|\tau_{\parallel}| \approx 1.55$  which is located approximately halfway in between the peaks of  $c_\tau$  at  $|\tau_{\parallel}| \approx 1.45$  and  $1.60$  for the homogeneous directional and for the homogeneous nonspecific anchoring

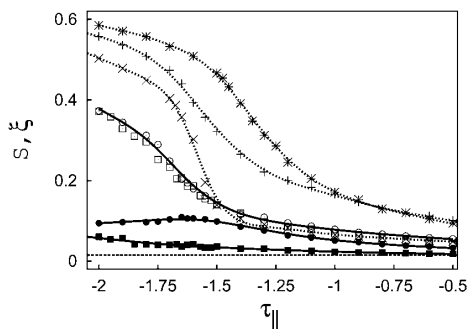


**Fig. 6** The Maier-Saupe nematic order parameter  $S$  as a function of applied compressional stress. Homogeneous anchoring scenarios: (×) planar, (+) nonspecific, ( $\varphi = \frac{\pi}{2} - \theta$ ) directional; hybrid anchoring scenarios: (□) *np*, (○) *nd*. Also shown are plots of the biaxial order parameter  $\xi$  for *np* (■) and *nd* anchoring scenarios (●). Solid and dashed lines represent fits to guide the eye. The vertical dashed line indicates typical values of  $\xi$  obtained for homogeneous anchoring scenarios.

scenarios, respectively. One may therefore speculate that the broad shoulder in the plot of  $c_\tau$  in Fig. 2(c) reflects some other structural transformation than the secondary peaks in the plots of  $c_\tau$  in Fig. 2(a) and 2(b) (see Sec. III D).

The IN transformation may also be located through plots of the (global) Maier-Saupe nematic order parameter  $S$  plotted as a function of applied compressional stress in Fig. 6. In all cases considered  $S(\tau_{\parallel})$  is sigmoidal in shape. Taking the inflection of the sigmoidal curves as an operational definition of the location of the IN transformation<sup>7</sup> very good agreement with the position of maxima in the plots of  $c_\tau$  presented in Fig. 2 is obtained. For the two hybrid anchoring scenarios the curves  $S(\tau_{\parallel})$  are indistinguishable which is consistent with the observation that the main peak of  $c_\tau$  in the parallel plots in Fig. 2(b) and 2(c) appears to be unaffected by the specific combination of anchoring conditions. Moreover, even the plot of  $c_\tau$  for the *hp* anchoring scenario [see Fig. 2(a) is located at about the same  $|\tau_{\parallel}| \approx 1.75$ . Hence, irrespective of the nature of the hybrid anchoring scenario the formation of a nematic structure of the confined fluid occurs at about the same compressional stress. Interestingly, this stress coincides approximately with the one demarcating the onset of nematization in the bulk ( $|\tau_{\parallel}| \approx 1.70$ , see Ref. 7). In general, it turns out that in the nematic phase  $S$  is much smaller for hybrid than for homogeneous anchoring scenarios. However, the specific hybrid anchoring scenario manifests itself in plots of the biaxial order parameter  $\xi$  which turns out to be larger for the *nd* than for the *np* anchoring scenario. Also shown in Fig. 6 are typical values of  $\xi$  for homogeneous anchoring where one expects  $\xi = 0$ . However, in actual simulations one typically obtains  $\xi \lesssim 0.02$  on account of a small system-size effect discussed in the Appendix of the paper by Eppenga and Frenkel.<sup>31</sup>

#### D. Local orientation

To gain deeper insight into structural transformations occurring in the confined liquid crystal with increasing compressional stress we consider the *local* Maier-Saupe nematic order parameter  $S(z)$  and  $P_2(z)$  [see eqn (3.4)]. According to their definition  $P_2(z) = S(z)$  if molecules are aligned homeotropically with the solid substrate. If this alignment is perfect,  $P_2(z) = 1$ . If, on the other hand,  $P_2(z) < S(z)$  and  $S(z) > 0$  a certain degree of nematic order exists but  $|\cos \theta| = |\hat{n} \cdot \hat{e}_z| < 1$ , that is  $\hat{n}$  does not coincide with the substrate normal.

An inspection of Fig. 7 shows that a nearly perfect homeotropic alignment arises in the immediate vicinity of the lower substrate where  $g(\hat{u})$  is given by eqn (2.8b). If, on the other hand, the preferential orientation of molecules is in a direction parallel with the solid substrates,  $P_2(z) = -0.5$  but  $S(z) > 0$  which is the case in the immediate vicinity of the upper substrate characterized by the anchoring function specified in eqn (2.8c). For the plots presented in Fig. 7 we selected state points around the two maxima visible in the plots of  $c_\tau$  in Fig. 2(a) for hybrid anchoring. Both parts of Fig. 7 show that the system undergoes a structural transition during which the local order increases. These transformations are restricted mostly to “inner” parts of the confined fluid (*i.e.*, regions located at  $|z/s_{z0}| \leq 0.25$ ) for which the direct interaction with either solid substrate is negligible according to the plot in Fig. 1. Notice also that in the “nematic” phase

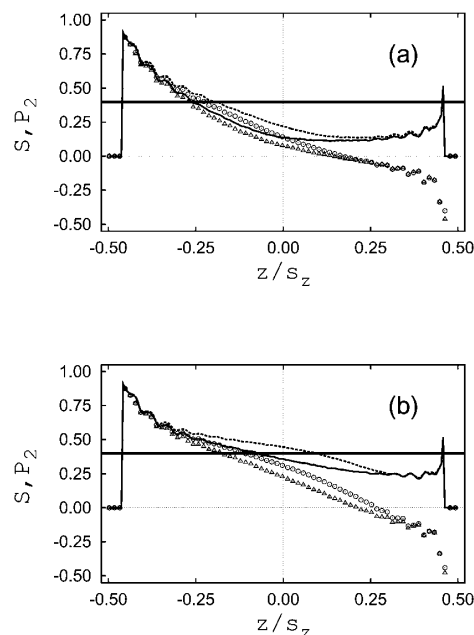


**Fig. 7** Plots of  $S(z)$  (lines) and  $P_2(z)$  (symbols) as functions of position between lower and upper substrates located at  $z_w/s_{z0} = \mp 0.5$  ( $s_{z0} = 20$ ) for the *hp* anchoring scenario. (a) (—,  $\Delta$ ):  $\tau_{\parallel} = -1.45$ ; (---,  $\circ$ ):  $\tau_{\parallel} = -1.55$ . (b) (—,  $\Delta$ ):  $\tau_{\parallel} = -1.70$ ; (---,  $\circ$ ):  $\tau_{\parallel} = -1.80$  [see also Fig. 2(a)]. The full horizontal line demarcates  $S(z) = 0.4$  taken as the nematic threshold.<sup>36</sup>

[see Fig. 7(b)] the local order parameter  $S(z)$  is still smaller than the threshold value of 0.4 suggested by the Maier-Saupe (mean-field) theory for an IN phase transition for  $|z/s_{z0}| \leq 0.1$ . This is the reason why the *global* nematic order parameter  $S$  for the two hybrid anchoring scenarios plotted in Fig. 6 barely reaches the value  $S = 0.4$  even at the highest compressional stresses considered.

To visualize subtle details of these structural transformations more clearly it turns out to be helpful to consider  $\Delta S(z) \equiv S(z; \tau_{\parallel}^{(2)}) - S(z; \tau_{\parallel}^{(1)})$  and, with an analogous definition,  $\Delta P_2(z)$  where  $|\tau_{\parallel}^{(1)}| < |\tau_{\parallel}^{(2)}|$ . Plots of both quantities in Fig. 8(a) show that around the secondary maximum of the heat capacity curve presented in Fig. 2(a) for the hybrid anchoring scenario  $\Delta S(z) = \Delta P_2(z)$  with a maximum shifted a bit towards the homeotropically anchoring substrate. For thermodynamic states around the main maximum of  $c_\tau$  in Fig. 2(a), on the other hand, plots in Fig. 8(b) indicate that the maximum in the curves  $\Delta S(z)$  and  $\Delta P_2(z)$  is slightly shifted towards the parallel anchoring substrate whereas  $\Delta S(z) = \Delta P_2(z)$  still holds. However, in both cases structural transformations are most pronounced near the center of the slit-pore in agreement with the plots shown in Fig. 7.

To interpret the data presented in Fig. 8 it is useful to consider the schematic representation presented in Fig. 9. In the nematic phase the director  $\hat{n}$  describing the preferential orientation of the molecules will generally form a certain angle with the substrate normal (*i.e.*, the  $z$ -direction) and may lie anywhere on the blue

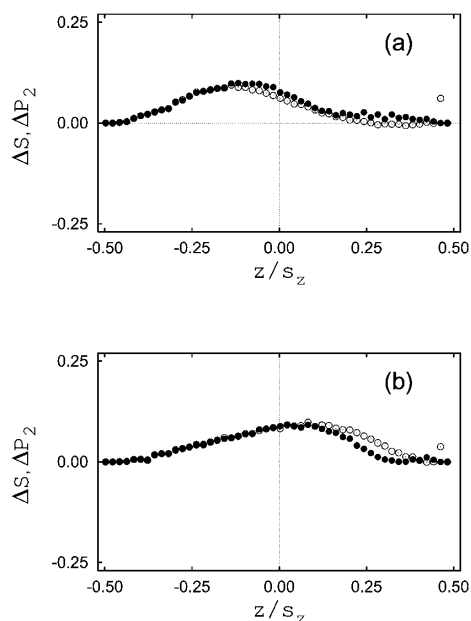


**Fig. 8** Plots of  $\Delta S(z)$  (●) and  $\Delta P_2(z)$  (○) for the hybrid homeotropic-planar anchoring scenario as functions of position between lower and upper substrates. (a)  $\tau_{||}^{(1)} = -1.45$ ,  $\tau_{||}^{(2)} = -1.55$ , (b)  $\tau_{||}^{(1)} = -1.70$ ,  $\tau_{||}^{(2)} = -1.80$ . Notice, that error bars may increase substantially as  $|z|/s_{z0} \rightarrow 0.5$  because of the excluded volume in the immediate vicinity of the solid substrates (see Fig. 6).

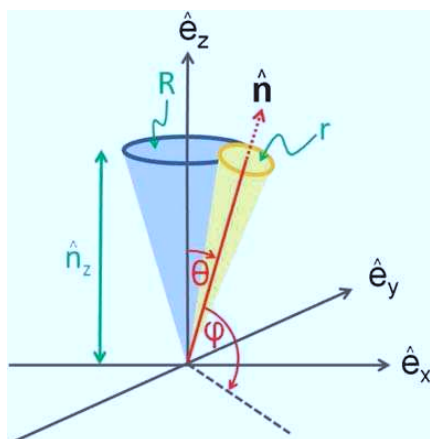


**Fig. 9** In the nematic phase the director  $\hat{n}$ , which ends at the center of the base area of the yellow cone, forms an angle  $\cos \theta = \hat{n} \cdot \hat{e}_z = \hat{n}_z$  with the  $z$ -axis, an angle with the  $x$ - $y$  plane, and may lie anywhere on the surface of the blue cone. Radius  $R$  of the base area of the blue cone is a measure of the degree of homeotropic alignment proportional to  $P_2$  [see eqn (3.4)]; radius  $r$  of the base area of the yellow cone is a measure of  $S$ .

cone drawn in Fig. 9. The projection  $\hat{n}_z$  of  $\hat{n}$  onto the  $z$ -axis is related to the value of  $P_2$  according to the definition given in eqn (3.4). Because  $|\hat{n}| = 1$  by definition, the radius  $R$  of the circular base area of the blue cone becomes smaller and vanishes

eventually if  $\theta \rightarrow 0$ . If, on the other hand,  $\hat{n}$  becomes more aligned with the  $x$ - $y$  plane,  $R$  increases and  $\hat{n}_z$  vanishes as  $\varphi \rightarrow 0$ . Therefore,  $R$  may be viewed as a geometrical representation of the degree of homeotropic alignment. Likewise, the radius  $r$  of the circular base area of the yellow cone is a geometrical representation of the Maier-Saupe nematic order parameter  $S$ : The larger  $r$  the lower is  $S$ . A nonvanishing value of  $r$  reflects a certain width of the distribution of molecular orientations around  $\hat{n}$  on account of thermal fluctuations.

Applying these geometrical concepts to the plots in Fig. 8(a) it is clear that  $R$  and  $r$  of the two cones plotted in Fig. 9 shrink simultaneously as the transverse compressional stress increases. This implies that the nematic order parameter  $S(z)$  increases and that the director becomes more aligned with the  $z$ -axis. In other words, the secondary maximum in the plot of  $c_z$  in Fig. 2(a) at  $|\tau_{||}| \approx 1.50$  reflects an increasing homeotropic (pre)alignment of molecules near the center of the confined fluid [cf., Fig. 7(a), 8(a)]. Similarly, the maximum at  $c_z$  at  $|\tau_{||}| \approx 1.75$  may be interpreted as an increase in nematic order which is mostly caused by an increasing alignment of molecules with the  $z$ -axis.

The homeotropic prealignment at  $|\tau_{||}| \approx 1.50$  takes place in a part of the fluid slightly closer to but still sufficiently far from the homeotropically anchoring substrate such that this prealignment is not a consequence of a direct fluid-substrate interaction. However, prealignment turns out to be coupled to another structural reorganisation of the confined fluid. This is illustrated by plots of  $\rho(z)$  in Fig. 5 for thermodynamic states embracing the small secondary peak in the plot of  $c_z$  at  $|\tau_{||}| \approx 1.50$  presented in Fig. 2(a). As one can see from Fig. 5 there is a sequence of small but significant oscillations developing as the compressional stress increases from  $|\tau_{||}| = 1.45$  to  $1.55$ . These oscillations are fingerprints of weak stratification of the fluid at the center of the slit-pore. Because of this weak change in molecular packing one anticipates an accompanying change in the fluid's isothermal compressibility. Indeed this notion is supported by plots in Fig. 10 showing that  $\kappa_T$  passes through a maximum at  $|\tau_{||}| \approx 1.50$ . Notice that both peaks in the plot of  $\kappa_T$  parallel those observed in the corresponding plot of  $c_z$ . A similar formation of additional layers with increasing compression and away from the substrates has already been reported in Ref. 7 for homogeneous anchoring scenarios. The formation of these additional layers can be attributed to orientation-induced changes in local packing characteristics akin to those illustrated by Fig. 5. Moreover, perceiving the confining solid substrates as an external field a similar field-induced formation of additional layers has been reported recently by Jordanovic and Klapp who investigated confined dipolar fluids in external magnetic fields pointing in different directions relative to the substrate plane.<sup>37,38</sup> Hence, the appearance of additional layers in a confined fluid of anisometric molecules caused by some direction-dependent external field seems to be a generic feature which is qualitatively independent of details of the intermolecular interaction potential or the precise nature of the external field.

Corresponding plots in Fig. 11 for the  $np$  anchoring scenario show that around the secondary peak of  $c_z$  at  $\tau_{||} \approx -1.63$  [see Fig. 2(b)] the structural transformation is very similar to the one illustrated by the plots in Fig. 8: first, molecules prealign

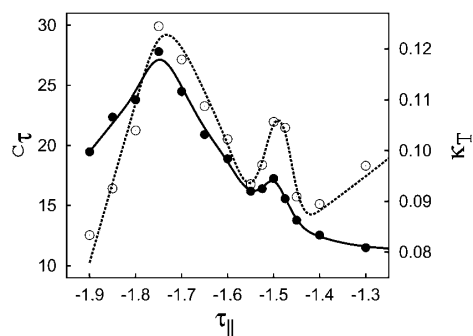


**Fig. 10** Plots of  $c_r$  (●) (left ordinate) and  $\kappa_T$  (○) (right ordinate) as functions of  $\tau_{\parallel}$  for the *hp* hybrid anchoring scenario [cf., Fig. 2(a)]; lines represent fits to the data points intended to guide the eye.

preferentially with the  $z$ -axis in a region of the confined fluid somewhat closer to the nonspecifically anchoring substrate [see Fig. 11(a)]. In the geometrical interpretation of Fig. 9 this may again be described in terms of a simultaneous shrinkage of both  $R$  and  $r$ . However, the plots in Fig. 11(b) illustrate a somewhat different structural transformation. Here,  $\Delta S(z) > \Delta P_2(z)$  indicating that the alignment of molecules with the  $z$ -axis is smaller than the increase in nematic order. This effect is more pronounced closer to the upper (planar anchoring) substrate as one would expect. In the geometrical terms of Fig. 9 this may be described as a decrease of  $R$  and a simultaneous larger decrease of  $r$ . In other words, the alignment of molecules with the local director increases reflecting an enhanced degree of nematic order. However, the local director still forms a nonvanishing angle  $\theta$  with  $\hat{e}_z$ .

A totally different structural transformation is observed for the *nd* anchoring scenario for which we present plots of  $\Delta S(z)$  and  $\Delta P_2(z)$  in Fig. 12. For two thermodynamic states in the vicinity of the weak shoulder in the plot of  $c_r$  at  $|\tau_{\parallel}| \approx 1.55$  [see Fig. 2(c)] the plots in Fig. 12(a) indicate that in the immediate vicinity of the homeotropically anchoring substrate  $\Delta S(z) = \Delta P_2(z)$  referring to an enhanced local alignment of the molecules with  $\hat{e}_z$ . On the contrary, in the upper halfspace of the slit-pore,  $\Delta P_2(z) < 0$  whereas  $\Delta S(z) > 0$ . In the geometric terms introduced in Fig. 9 this can be ascribed to an increase of  $R$  (*i.e.*, a decrease of  $\hat{n}_z$ ) and a simultaneous decrease of  $r$ . In other words, the increase in nematic order is a consequence of a preferential alignment of the molecules with the  $x$ -axis. At higher compressional stresses in the vicinity of the main peak of  $c_r$  at  $|\tau_{\parallel}| \approx 1.70$  [see Fig. 2(c)] this trend is somewhat reversed as the corresponding plots in Fig. 12(b) show. The plot of  $\Delta S(z)$  is symmetric about the midplane of the slit-pore and because  $\Delta S(z) > 0$  the nematic order in the system increases mainly at the center of the confined fluid. There is also some enhanced homeotropic alignment which turns out to be somewhat more pronounced in the vicinity of the homeotropically anchoring wall in accord with one's physical intuition. In other words, plots in Fig. 12(b) reflect a substantial frustration of molecules with respect to the alignment favored by the two competing substrates. This frustration of molecular orientation is also illustrated by the snapshot presented in Fig. 3.

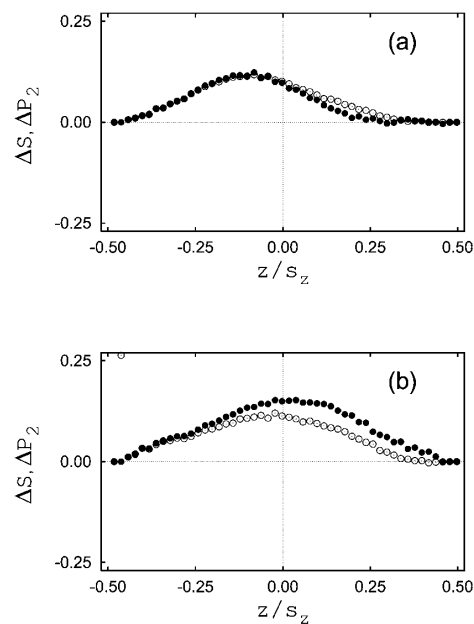


**Fig. 11** As Fig. 8, but for the *np* anchoring scenario. (a)  $\tau_{\parallel}^{(1)} = -1.58$ ,  $\tau_{\parallel}^{(2)} = -1.65$ ; (b)  $\tau_{\parallel}^{(1)} = -1.67$ ,  $\tau_{\parallel}^{(2)} = -1.80$ .

#### IV. Summary and conclusions

In this work we consider a simple model of a liquid crystal confined to a slit-pore with hybrid anchoring at the solid substrates, that is each substrate discriminates molecules on account of their orientation with respect to the substrate plane where we take this energetic discrimination to be different at the two substrates. Employing Monte Carlo simulations in a specialized isostress ensemble we can locate specific compressional stresses, at which the fluid undergoes a significant structural reorganization, through characteristic maxima of the isostress heat capacity.

As in our previous study<sup>7</sup> the location of these maxima coincides with inflection points in plots of the Maier-Saupe nematic  $S$  order parameter as a function of compressional stress. Considering various hybrid anchoring scenarios it turns out that the location of the IN transition is largely independent of the combination of anchoring conditions at the two substrates. This is because in the nematic phase the director is trying to point in a direction compromising between the competing orientations enforced by the two substrates simultaneously. Consequently, plots of  $S$  versus  $\tau_{\parallel}$  are nearly indistinguishable as far as the *np* and *nd* anchoring scenarios are concerned. Our parallel analysis of local order parameter profiles shows that the IN transformation occurs near the center of the confined liquid crystal that is approximately halfway in between the solid substrates.

However, the specific hybrid anchoring scenario does have an impact on a secondary structural reorganization that occurs at lower compressional stresses preceding that of the IN transition. This secondary transformation may cause prealignment with the  $z$ -axis (*i.e.*, in a direction perpendicular to the substrate plane) or

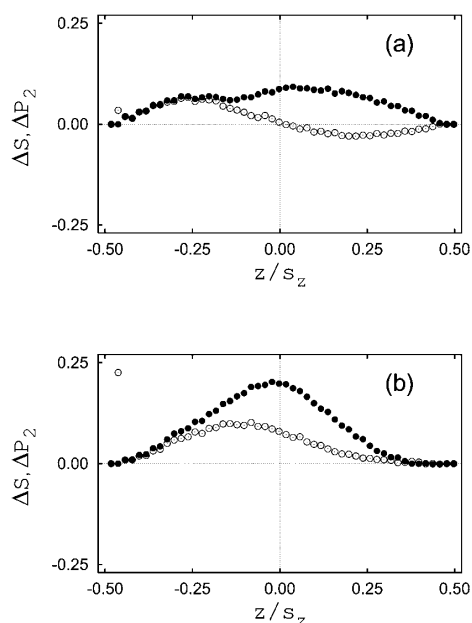


**Fig. 12** As Fig. 8, but for the *nd* anchoring scenario. (a)  $\tau_{\parallel}^{(1)} = -1.50$ ,  $\tau_{\parallel}^{(2)} = -1.60$ ; (b)  $\tau_{\parallel}^{(1)} = -1.63$ ,  $\tau_{\parallel}^{(2)} = -1.75$ .

it may force molecules to prealign to a certain extent with the  $x$ - $y$  plane. Which one of these two cases is realized depends on the stronger anchoring scenario of the hybrid pair. Thus, our results show that homeotropic is stronger than planar anchoring during this prealignment process. The same is true for the nonspecific anchoring which favors a homeotropic alignment of the fluid molecules on account of the symmetry breaking presence of the solid substrates. In the combination with nonspecific anchoring the directionally anchoring substrate “wins” and is thus considered stronger in the above sense. In any event, molecular prealignment occurs preferentially near the midplane ( $z = 0$ ) of the confined fluid.

In slit-pores with hybrid anchoring at the substrates one generally anticipates a certain degree of biaxiality. Our simulations do, however, show that the degree of biaxiality is actually quite small. Only the *nd* anchoring scenario exhibits a significant degree of biaxiality of about 25% of  $S$  in the nematic phase. The apparent lack of a more substantial biaxiality can be understood by realizing that the director field  $\hat{n}(z)$  varies as a function of position w.r.t. the location of the substrate plane. This is inferred from a characteristic “snapshot” of a configuration of molecules in the nematic phase of the *nd* anchoring scenario. In other words, the preferential orientation of molecules in the nematic phase varies with position such that more than just two preferred orientations in the confined liquid crystal are present. The small nonvanishing biaxiality for the *nd* anchoring scenario is caused by those few layers of molecules in the vicinity of each substrate that exhibit either a homeotropic or a planar orientation of the molecules.

Finally, it would be interesting to study in detail the *mechanism* of formation of nematic phases in the present model system. For example, at present it is not really clear whether the formation of

nematic phases constitutes a continuous or weakly discontinuous phase transition. However, as we already pointed out in our previous study<sup>7</sup> there is some evidence suggesting that the IN phase transition is a continuous process both in the bulk and under confinement. This is inferred from the apparent absence of hysteresis in the vicinity of the transition points. However, to be sure about this conclusion a careful finite-size scaling analysis would be required which is computationally quite demanding for the present model system. For the current system size finite-size effects are, however, expected to be already small.

### Acknowledgements

We are grateful for financial support from the International Graduate Research Training Group 1524 “Self-assembled soft-matter nanostructures at interfaces”. We also thank two anonymous referees for their insightful comments.

### References

- 1 V. Freedericksz and V. Zolina, *Trans. Faraday Soc.*, 1933, **29**, 919.
- 2 P. Ziherl, F. K. P. Haddadan, R. Podgornik and S. Zumer, *Acta Phys. USSR*, 1939, **10**, 557.
- 3 O. Guzman, N. L. Abbott and J. J. de Pablo, *J. Chem. Phys.*, 2005, **122**, 184711.
- 4 V. K. Gupta, J. J. Skaife, T. B. Dubrovsky and N. L. Abbott, *Science*, 1998, **279**, 2077.
- 5 J. J. Skaife and N. L. Abbott, *Langmuir*, 2000, **16**, 3529.
- 6 J. J. Skaife and N. L. Abbott, *Langmuir*, 2001, **17**, 5595.
- 7 M. Greschek, M. Melle and M. Schoen, *Soft Matter*, 2010, **6**, 1898.
- 8 K. Binder, D. Landau and A. Ferrenberg, *Phys. Rev. E: Stat. Phys., Plasmas, Fluids, Relat. Interdiscip. Top.*, 1995, **51**, 2823.
- 9 K. Binder, R. Evans, D. Landau and A. Ferrenberg, *Phys. Rev. E: Stat. Phys., Plasmas, Fluids, Relat. Interdiscip. Top.*, 1996, **53**, 5023.
- 10 A. Ferrenberg, D. Landau and K. Binder, *Phys. Rev. E: Stat. Phys., Plasmas, Fluids, Relat. Interdiscip. Top.*, 1998, **58**, 3353.
- 11 Milchev, M. Müller and K. Binder, *Europhys. Lett.*, 2005, **70**, 348.
- 12 R. Memmer and O. Fliegans, *Phys. Chem. Phys.*, 2003, **5**, 558.
- 13 A. Chrzanoswska, P. Teixeira, H. Ehrentraut and D. Cleaver, *J. Phys.: Condens. Matter*, 2001, **13**, 4715.
- 14 F. Schmid and D. Cheung, *Europhys. Lett.*, 2006, **76**, 243.
- 15 D. Marenduzzo, E. Orlandini and J. Yeomans, *Europhys. Lett.*, 2003, **64**, 406.
- 16 M. Krech, *The Casimir effect in critical systems*, World Scientific, Singapore, 1994.
- 17 N. Priezjew, G. Skacej, R. Pelcovits and S. Zumer, *Phys. Rev. E: Stat., Nonlinear, Soft Matter Phys.*, 2003, **68**, 041709.
- 18 I. Rodriguez-Ponce, J. Romero-Enrique and L. Rull, *Phys. Rev. E: Stat., Nonlinear, Soft Matter Phys.*, 2001, **64**, 051704.
- 19 H. Steuer, S. Hess and M. Schoen, *Phys. Rev. E: Stat., Nonlinear, Soft Matter Phys.*, 2004, **69**, 031708.
- 20 L. Harnau, S. Kondrat and A. Poniewierski, *Phys. Rev. E: Stat., Nonlinear, Soft Matter Phys.*, 2005, **72**, 011701.
- 21 L. Harnau, S. Kondrat and A. Poniewierski, *Phys. Rev. E: Stat., Nonlinear, Soft Matter Phys.*, 2007, **76**, 051701.
- 22 L. Harnau and S. Dietrich, *Europhys. Lett.*, 2006, **73**, 28.
- 23 D.-H. Chung, Y. Takahashi, K. Ishikawa, C.-J. Yu, S.-D. Lee and H. Takezoe, *Jpn. J. Appl. Phys.*, 2003, **42**, 1686.
- 24 Zappone, P. Richetti, R. Barberi, R. Bartolino and H. Nguyen, *Phys. Rev. E: Stat., Nonlinear, Soft Matter Phys.*, 2005, **71**, 041703.
- 25 S. Hess and B. Su, *Z. Naturforsch.*, 1999, **54 a**, 559.
- 26 M. Schoen, *Phys. A*, 1999, **270**, 353.
- 27 M. Allen and D. Tildesley, *Computer simulation of liquids*, Oxford Science Publications, Oxford, 1986.
- 28 Pardowitz and S. Hess, *Phys. A*, 1980, **100**, 540.
- 29 W. H. Press, S. A. Teukolsky, W. T. Vetterling, and B. P. Flannery, *Numerical recipes in FORTRAN*, Cambridge University Press, Cambridge, 1989.
- 30 R. Low, *Eur. J. Phys.*, 2002, **23**, 111.
- 31 R. Eppenga and D. Frenkel, *Mol. Phys.*, 1984, **52**, 1303.

- 
- 32 A. Richter and T. Gruhn, *J. Chem. Phys.*, 2006, **125**, 064908.  
33 W. Maier and A. Saupe, *Z. Naturforsch.*, 1959, **14 a**, 882.  
34 W. Maier and A. Saupe, *Z. Naturforsch.*, 1960, **15 a**, 287.  
35 S. Klapp, Y. Zeng, D. Qu and R. v. Klitzing, *Phys. Rev. Lett.*, 2008, **100**, 118303.  
36 P. G. de Gennes and J. Prost, *The Physics of Liquid Crystals*, Clarendon, Oxford, 1995.  
37 J. Jordanovic and S. H. L. Klapp, *Phys. Rev. Lett.*, 2008, **101**, 038302.  
38 J. Jordanovic and S. H. L. Klapp, *Phys. Rev. E: Stat., Nonlinear, Soft Matter Phys.*, 2009, **79**, 021405.

## Conclusions & Outlook

Monte Carlo simulations are used in the isostress-isostrain ensemble to investigate the IN transition for a prolate thermotropic liquid crystal in bulk and in confinement. We fixed the temperature  $T = 1.0$  in all simulations and varied the compressional stress  $\tau$  to study the system along an isotherm. The pairwise molecular interaction has been approximated by the Hess-Su potential. In this model potential the anisotropic shape is modelled by an orientation dependent attraction such that steric effects can largely be neglected.

The IN transition is then signaled by a substantial increase of the nematic order parameter  $S$ . In an atomistic simulation of finite size the profiles of order parameter and response functions are rounded such that one may employ the cumulant intersection method proposed by Binder to determine whether this transition is *first-order* or *continuous*. Here we use the second-order cumulant depending on the eigenvalues  $\lambda_0$  and  $\lambda_+$  of the order tensor  $\mathbf{Q}$ . Although the cumulants intersect in a universal point  $\tau^* = -1.74$  we could show that the correlation length  $\ell$  of orientational correlations does not exceed twice the molecular length and therefore remains finite and small in the immediate vicinity of the transition. The finiteness of  $\ell$  points to a *first-order* transition and suggests that the maximum of the isobaric heat capacity scales as  $c_\tau^m \propto N^y$ . We were able to show that  $y \approx 0.58$  is considerably smaller than 1, as anticipated for a *first-order* transition, but is significantly larger than  $\frac{2}{3\nu} - 1 \approx 0.06$  expected for a *continuous* transition. However, the variation of the nematic order parameter around the transition turned out to be smooth and it was not possible to detect any hysteresis in the vicinity of the transition point.

The Landau potential  $\mathcal{G}$  of the Landau-De Gennes' theory fitted to all order parameter distributions in the direct vicinity of the IN transition. The symmetric bimodal

shape of the order parameter distribution at the transition point reveals that the free-energy barrier  $\beta\Delta\mathcal{G}$  separating the coexisting isotropic and nematic state is larger than  $k_B T$ . In this case, the Ginzburg criterion, which determines the applicability of Landau-De Gennes theory, may be accepted.

Summarising these properties led us to conclude, that the IN transition for this model is weakly *first-order*. Since the heat capacity is related to the entropy change the pronounced peak in plots of  $c_\tau$  indicates a loss in orientational entropy due to preferential alignment parallel with  $\hat{\mathbf{n}}$ . However, the gain in energy due to alignment exceeds the entropy loss and therefore stabilises the nematic state at higher compressional stresses. Experimentally, the IN transition has been shown to be a weak *first-order* transition [69, 98]. Similar conclusions have been reached for atomistic computer simulations of a lyotropic lattice model liquid crystal by Weber *et al.* [89], the 3-dimensional Lebwohl-Lasher model [99], and for the Gay-Berne model by Berardi *et al.* [100].

The influence of a confining slit-pore on the IN transition was also studied with two plane, parallel, and unstructured walls separated by a distance of several molecular diameters to mimic nanoconfinement. The molecular orientation of the particles adjacent to the walls is determined by so-called anchoring functions. They prealign particles close to the walls which is expected to influence the IN transition by facilitating the orientational symmetry breaking. This led us to study the impact of four anchoring scenarios on the IN transition where we have applied the same anchoring functions at both walls. We referred to this slit-pore as homogeneously aligned.

For *planar* anchoring functions we observe the formation of an additional fluid layer preceding the IN transition. This additional layer can form because of the non-vanishing orientation dependent fluid-substrate interaction at the pore centre. When the compressional stress is increased towards  $\tau_{\parallel}^{\text{IN}}$  this orienting influence introduces *planar* prealignment in the isotropic phase such that the particles can be packed more efficiently. This structural reorganisation is monitored by characteristic changes in the isothermal compressibility  $\kappa_T$ .

At the same compressional stress, the total configurational energy in the isotropic bulk phase is nearly the same for directional and planar anchoring. However, the particles are much more prealigned for directional anchoring compared with planar anchoring. This is because of the energetic “pinning” to the  $x$  axis for directional anchoring whereas for planar anchoring the particles are free to orient themselves in

the  $x - y$  plane. Hence, the loss of rotational entropy during the IN transition is much larger for planar anchoring. This is supported by a substantially larger maximum in  $c_\tau$  for the planar anchoring scenario. However, the maximum for directional anchoring is shifted to lower values of  $\tau_{\parallel}^{\text{IN}}$  such that we conclude that orientational prealignment and consequently smaller loss in rotational entropy supports the IN transition.

We show that the order parameter profiles of nonspecific and directional anchoring have the same rounded shape, such that they could be mapped onto each other when properly shifted with respect to  $\tau_{\parallel}$ . From this we expect that the loss of rotational entropy is nearly the same for both anchoring scenarios. However, because the maximum in  $c_\tau$  is shifted to smaller values of  $\tau_{\parallel}$  for directional anchoring, we conclude that energetic discrimination supports the IN transition. This is supported by results for the homeotropic anchoring scenario for which we have been unable to observe an IN transition. The energetically supported homeotropic alignment together with the favourable side-side configuration result in synergetic effects such that the first layers at each wall are already highly aligned even for the lowest compressional stress  $\tau_{\parallel} = -0.1$  studied. This strong prealignment due to energetic discrimination suggests a minimum loss of rotational entropy which shifts the transition to low compressional stresses if the transition is not completely suppressed.

In hybrid aligned slit-pores a different anchoring function is applied at either wall. For the hybrid alignment we chose the wall separation to be twice the value employed for homogeneous alignment, in order to minimise the wall-induced orientational influence near the mid-plane ( $z = 0$ ). The hybrid anchoring does not affect  $\tau_{\parallel}^{\text{IN}}$  of the IN transition because the transition happens near the mid-plane. More important is the observed secondary structural reorganisation preceding the IN transition to the bent state, i.e. continuous variation of the director from one wall to the other. Particles close to  $z = 0$  prealign either with the  $z$ -axis or to a certain extent with the  $x - y$  plane. This is clearly demonstrated by plots of  $\Delta S(z)$  and  $\Delta P_2(z)$  where we utilise their complementary character. The prealignment is dictated by the stronger anchoring scenario of the hybrid pair. In the  $hp$  hybrid slit pore homeotropic anchoring ( $h$ ) is stronger than planar anchoring ( $p$ ) which results in prealignment parallel to the wall normal. In the  $nd$  hybrid scenario directional anchoring ( $d$ ) dominates nonspecific anchoring ( $n$ ). Nonspecific anchoring is weak, because particles align solely on account of the symmetry breaking presence of the substrates.

We show that the biaxiality, which one might have anticipated for the bent state in

the hybrid slit-pores, is small. The amount of biaxiality is mainly determined by the layers in the vicinity of the substrate whereas the local nematic director  $\hat{\mathbf{n}}(z)$  points in direction compromising between competing orientations and therefore varies smoothly as a function of the position with respect to the location of the substrate. Only for the *nd* anchoring scenario could we observe significant degree of biaxiality of about 25% of *S* in the nematic phase.

### *Outlook*

It is shown here that liquid crystals confined by hybrid anchoring slit-pores show interesting structural reorganisations which depend on the strength of the anchoring functions. In future work it would be of interest to study the influence of chemically nano-structured substrates. Chemically structured substrates contain patterns of different anchoring functions and, since the anchoring functions are different as far as their strength is concerned, one anticipates an interplay of surface enforced alignment and liquid crystal elasticity. This could introduce interesting structural features in regions where the orientational distribution is induced solely by elastic forces. It is also of interest over which length scale the preferred molecular orientations could be imprinted onto the bulk fluid. Experimenters have addressed this topic [101, 102], but theoretical work is still lacking in this area.

# Bibliography

- [1] C. Vega and P. A. Monson. *Plastic crystal phases of hard dumbbells and hard spherocylinders*. J. Chem. Phys. **107**: 2696–2697 (1997).
- [2] S. Chandrasekhar. *Liquid Crystals* (Cambridge University Press, New York, 1977).
- [3] S. Singh. *Liquid Crystals: Fundamentals* (World Scientific, Singapore, 2002).
- [4] F. Reinitzer. *Beiträge zur Kenntniss des Cholesterins*. Monatsh. Chem. **9**: 421–441 (1888).
- [5] O. Lehmann. *Über fließende Krystalle*. Z. Phys. Chem. **4**: 462–472 (1889).
- [6] P. D. Gennes and J. Prost. *The Physics of Liquid Crystals* (Oxford University Press, New York, 1995).
- [7] F. D. Saeva (Ed.) *Liquid Crystals* (Marcel Dekker, New York, 1979).
- [8] G. Luckhurst and G. Gray. *The Molecular Physics of Liquid Crystals* (Academic Press, London, 1979).
- [9] G. Vertogen and W. H. de Jeu. *Thermotropic liquid crystals, Fundamentals* (Springer, Berlin/Heidelberg, 1988).
- [10] G. Friedel. *Les états mésomorphes de la matière*. Ann. Phys. (Paris) **19**: 273–474 (1922).
- [11] A. de Vries. *Structure and classification of thermotropic liquid crystals*. In Saeva [7].
- [12] S. E. B. Petrie. *Smectic liquid crystal*. In Saeva [7].
- [13] L. Onsager. *The effects of shape on the interaction of colloidal particles*. Ann. N.Y. Acad. Sci. **51**: 627–659 (1949).
- [14] W. Maier and A. Saupe. *Eine einfache molekulare Theorie des nematischen*

- kristallinflüssigen Zustandes*. Z. Naturforsch. A **13**: 564–566 (1958).
- [15] W. Maier and A. Saupe. *Eine einfache molekular-statistische Theorie der nematischen kristallinflüssigen Phase 1*. Z. Naturforsch. **14a**: 882–889 (1959).
- [16] C. Mauguin. *Orientation des cristaux liquides par les lames de mica.*. C. R. Acad. Sci. Paris **156**: 1246–1247 (1913).
- [17] B. Jérôme. *Surface effects and anchoring in liquid crystals*. Rep. Prog. Phys. **54**: 391–452 (1991).
- [18] I. Dierking. *Textures of liquid crystals* (Wiley-VCH, Weinheim, 2003).
- [19] J. Cognard. *Alignment of nematic liquid crystals and their mixtures*. Mol. Cryst. Liq. Cryst., Suppl. Series **1**: 1–77 (1982).
- [20] A. A. Sonin. *The Surface Physics of Liquid Crystals* (Gordon and Breach Publishers, New York, 1995).
- [21] F. D. Saeva. *Nematic mesophases*. In *Liquid Crystals* [7].
- [22] P. Chatelain. *Étude théorique de la diffusion de la lumière par un fluide présentant un seul axe d'isotropie: Application aux cristaux liquides du type nématique*. Acta Cryst. **4**: 453–457 (1951).
- [23] X. Zhuang, L. Marrucci, and Y. R. Shen. *Surface-monolayer-induced bulk alignment of liquid crystals*. Phys. Rev. Lett. **73**: 1513–1516 (1994).
- [24] V. Freedericksz and V. Zolina. *Forces causing the orientation of an anisotropic liquid*. Trans. Faraday Soc. **29**: 919–930 (1933).
- [25] P. Zihlerl, R. Podgornik, and S. Žumer. *Pseudo-Casimir structural force drives spinodal dewetting in nematic liquid crystals*. Phys. Rev. Lett. **84**: 1228–1231 (2000).
- [26] G. Barbero and R. Barberi. *Critical thickness of a hybrid aligned nematic liquid crystal cell*. J. Physique **44**: 609–616 (1983).
- [27] C. Chiccoli, P. Pasini, A. Šarlah, C. Zannoni, and S. Žumer. *Structures and transitions in thin hybrid nematic films: A Monte Carlo study*. Phys. Rev. E **67**: 050 703 (2003).
- [28] P. Palffy-Muhoray, E. C. Gartland, and J. R. Kelly. *A new configurational transition in inhomogeneous nematics*. Liq. Cryst. **16**: 713–718 (1994).
- [29] H. G. Galabova, N. Kothekar, and D. W. Allender. *Stable configurations in hybrid nematic cells in relation to thickness and surface order*. Liq. Cryst. **23**: 803–811 (1997).
- [30] D. J. Cleaver and P. I. C. Teixeira. *Discontinuous structural transition in a thin*

- hybrid liquid crystal film*. Chem. Phys. Lett. **338**: 1–6 (2001).
- [31] P. I. C. Teixeira, F. Barmes, C. Anquetil-Deck, and D. J. Cleaver. *Simulation and theory of hybrid aligned liquid crystal films*. Phys. Rev. E **79**: 011 709 (2009).
- [32] F. Barmes and D. J. Cleaver. *Computer simulation of a liquid-crystal anchoring transition*. Phys. Rev. E **69**: 061 705 (2004).
- [33] F. J. Carrion, G. Martinez-Nicolas, P. Iglesias, J. Sanes, and M. D. Bermudez. *Liquid crystals in tribology*. Int. J. Mol. Sci. **10**: 4102–4115 (2009).
- [34] K. Nakano. *Scaling law on molecular orientation and effective viscosity of liquid-crystalline boundary films*. Tribol. Lett. **14**: 17–24 (2003).
- [35] I. A. Shanks. *The physics and display applications of liquid crystals*. Contemp. Phys. **23**: 65–91 (1982).
- [36] R. A. M. Hikmet and H. Kemperman. *Electrically switchable mirrors and optical components made from liquid-crystal gels*. Nature **392**: 476–479 (1998).
- [37] S. J. Woltman, G. D. Jay, and G. P. Crawford. *Liquid-crystal materials find a new order in biomedical applications*. Nat. Mater. **6**: 929–938 (2007).
- [38] C. J. Woolverton, E. Gustely, L. Li, and O. D. Lavrentovich. *Liquid crystal effects on bacterial viability*. Liq. Cryst. **32**: 417–423 (2005).
- [39] S. V. Shiyankovskii, T. Schneider, I. I. Smalyukh, T. Ishikawa, G. D. Niehaus, K. J. Doane, C. J. Woolverton, and O. D. Lavrentovich. *Real-time microbe detection based on director distortions around growing immune complexes in lyotropic chromonic liquid crystals*. Phys. Rev. E **71**: 020 702 (2005).
- [40] M. Kleman and O. D. Lavrentovich. *Soft Matter Physics: An Introduction* (Springer, Berlin/Heidelberg, 2003).
- [41] N. L. A. Yan-Yeung Luk, Sean F. Campbell and C. J. Murphy. *Non-toxic thermotropic liquid crystals for use with mammalian cells*. Liq. Cryst. **31**: 611–621 (2004).
- [42] N. Lockwood, J. Mohr, L. Ji, C. Murphy, S. Palecek, J. de Pablo, and N. Abbott. *Thermotropic liquid crystals as substrates for imaging the reorganization of matrigel by human embryonic stem cells*. Adv. Funct. Mater. **16**: 618–624 (2006).
- [43] M. Schoen and S. Klapp. *Nanoconfined fluids. Soft matter between two and three dimensions* (Wiley-VCH, New Jersey, 2007).
- [44] H. B. Callen. *Thermodynamics* (John Wiley & Sons Inc, New York, 1960).
- [45] D. A. McQuarrie. *Statistical Mechanics* (Harper & Row, New York, 1976).

- [46] J. G. Gay and B. J. Berne. *Modification of the overlap potential to mimic a linear site-site potential*. J. Chem. Phys. **74**: 3316–3319 (1981).
- [47] G. R. Luckhurst, R. A. Stephens, and R. W. Phippen. *Computer simulation studies of anisotropic systems. XIX. Mesophases formed by the Gay-Berne model mesogen*. Liq. Cryst. **8**: 451–464 (1990).
- [48] B. J. Berne and P. Pechukas. *Gaussian model potentials for molecular interactions*. J. Chem. Phys. **56**: 4213–4216 (1972).
- [49] P. Monson and M. Rigby. *Hard spherocylinder fluids: A Monte Carlo study*. Chem. Phys. Lett. **58**: 122–126 (1978).
- [50] J. A. C. Veerman and D. Frenkel. *Phase diagram of a system of hard spherocylinders by computer simulation*. Phys. Rev. A **41**: 3237–3244 (1990).
- [51] B. Martinez-Haya, A. Cuetos, S. Lago, and L. F. Rull. *A novel orientation-dependent potential model for prolate mesogens*. J. Chem. Phys. **122**: 024 908 (2005).
- [52] R. Eppenga and D. Frenkel. *Monte Carlo study of the isotropic and nematic phases of infinitely thin hard platelets*. Mol. Phys. **52**: 1303–1334 (1984).
- [53] G. Günther. *Soft Matter between Soft Solids. Sorption Induced Pore Deformation and Fluid Phase Behaviour*. Ph.D. thesis, Technische Universität Berlin (2010).
- [54] C. G. Gray and K. E. Gubbins. *Theory of Molecular Fluids* (Clarendon, Oxford, 1984).
- [55] T. Gruhn and M. Schoen. *Microscopic structure of molecularly thin confined liquid-crystal films*. Phys. Rev. E **55**: 2861–2875 (1997).
- [56] R. Balian. *From Microphysics to Macrophysics* (Springer, Berlin/Heidelberg, 1982).
- [57] M. E. Fisher. *The theory of equilibrium critical phenomena*. Rep. Prog. Phys. **30**: 615 (1967).
- [58] H. E. Stanley. *Introduction to Phase Transitions and Critical Phenomena* (Oxford University Press, New York, 1987).
- [59] E. F. Gramsbergen, L. Longa, and W. H. de Jeu. *Landau theory of the nematic-isotropic phase transition*. Phys. Rep. **135**: 195–257 (1986).
- [60] L. Landau. *Theory of phase transformations I*. Phys. Z Sowjetunion **11**: 26–47 (1937).
- [61] O. G. Mouritsen. *Computer Studies of Phase Transitions and Critical Phenomena* (Springer, Berlin/Heidelberg, 1984).

- [62] K. Binder. *Finite size scaling analysis of Ising model block distribution functions*. Z. Phys. B: Condens. Matter **43**: 119–140 (1981).
- [63] P. D. Gennes. *Phenomenology of short-range-order effects in the isotropic phase of nematic materials*. Phys. Lett. A **30**: 454–455 (1969).
- [64] L. Landau and E. Lifshitz. *Statistical Physics Part 1* (Pergamon Press, Oxford, 1980).
- [65] L. Landau. *Theory of phase transformations II*. Phys. Z Sowjetunion **11**: 545–555 (1937).
- [66] K. Binder. *Theory of first-order phase transitions*. Rep. Prog. Phys. **50**: 783 (1987).
- [67] G. Englert and A. Saupe. *Proton magnetic resonance spectra of oriented molecules: Acetylenic compounds, acetonitrile and methanol*. Mol. Cryst. **1**: 503–514 (1966).
- [68] J. Nehring and A. Saupe. *Orientation studies on fluorobenzenes in nematic liquid crystals by NMR*. Mol. Cryst. **8**: 403–415 (1969).
- [69] A. Saupe. *Recent results in the field of liquid crystals*. Angew. Chem. Int. Ed. **7**: 97–112 (1968).
- [70] V. Privman. *Finite Size Scaling and Numerical Simulation of Statistical Systems* (World Scientific, Singapore, 1990).
- [71] V. Ginzburg. *Some remarks on phase transitions of the second kind and the microscopic theory of ferroelectric materials*. Sov. Phys. Solid State **2**: 1824 (1960).
- [72] C.-P. Fan and M. J. Stephen. *Isotropic-nematic phase transition in liquid crystals*. Phys. Rev. Lett. **25**: 500–503 (1970).
- [73] G. Ciccotti and W. Hoover (Eds.) *Molecular-Dynamics Simulation of Statistical-Mechanical Systems* (North-Holland, Amsterdam, 1986).
- [74] K. E. Gubbins and J. D. Moore. *Molecular modeling of matter: Impact and prospects in engineering*. Ind. Eng. Chem. Res. **49**: 3026–3046 (2010).
- [75] M. P. Allen and D. J. Tildesley. *Computer simulation of liquids* (Clarendon Press, New York, 1989).
- [76] D. Frenkel and B. Smit. *Understanding Molecular Simulation, Second Edition: From Algorithms to Applications* (Academic Press, London, 2001).
- [77] D. P. Landau and K. Binder. *A Guide to Monte Carlo Simulations in Statistical Physics* (Cambridge University Press, New York, 2005).

- [78] W. Wood. *Early history of computer simulations in statistical mechanics*. In Ciccotti and Hoover [73].
- [79] N. Metropolis and S. Ulam. *The Monte Carlo method*. J. Am. Stat. Assoc. **44**: 335–341 (1949).
- [80] N. Metropolis, A. W. Rosenbluth, M. N. Rosenbluth, A. H. Teller, and E. Teller. *Equation of state calculations by fast computing machines*. J. Chem. Phys. **21**: 1087–1092 (1953).
- [81] W. Wood. *Monte Carlo calculations for hard disks in the isothermal isobaric ensemble*. J. Chem. Phys. **48**: 415–435 (1968).
- [82] P. Vorontsov-Vel'yaminov, A. El'yashevich, L. Morgenshtern, and V. Chasovskikh. *Investigation of phase transitions in argon and coulomb gas by the Monte Carlo method using an isothermally isobaric ensemble*. High Temp. (Teplofizika vysokikh temperatur) **8**: 261–268 (1970).
- [83] J. A. Barker and R. O. Watts. *Structure of water: A Monte Carlo calculation*. Chem. Phys. Lett. **3**: 144 – 145 (1969).
- [84] M. Schoen. *The Joule-Thomson effect in confined fluids*. Physica A **270**: 353–379 (1999).
- [85] M. E. Fisher and M. N. Barber. *Scaling theory for finite-size effects in the critical region*. Phys. Rev. Lett. **28**: 1516–1519 (1972).
- [86] Y. Imry and D. Bergman. *Critical points and scaling laws for finite systems*. Phys. Rev. A **3**: 1416–1418 (1971).
- [87] K. Binder. *Some recent progress in phenomenological theory of finite size scaling and application to Monte Carlo studies of critical phenomena*. In Privman [70], chapter IV.
- [88] D. P. Landau. *Monte Carlo studies of finite size effects at first and second order transitions*. In Privman [70], chapter V.
- [89] H. Weber. *Monte-Carlo-Simulationen der Gasdiffusion in Polymermatrizen*. Ph.D. thesis, Johannes-Gutenberg-Universität Mainz (1997).
- [90] Z. Y. Chen, P. C. Albright, and J. V. Sengers. *Crossover from singular critical to regular classical thermodynamic behavior of fluids*. Phys. Rev. A **41**: 3161–3177 (1990).
- [91] D. P. Landau. *Finite-size behavior of the Ising square lattice*. Phys. Rev. B **13**: 2997–3011 (1976).
- [92] D. P. Landau. *Finite-size behavior of the simple-cubic Ising lattice*. Phys. Rev.

- B **14**: 255–262 (1976).
- [93] K. Vollmayr, J. D. Reger, M. Scheucher, and K. Binder. *Finite size effects at thermally-driven first order phase transitions: A phenomenological theory of the order parameter distribution*. Z. Phys. B: Condens. Matter **91**: 113–125 (1993).
- [94] K. Binder and D. W. Heermann. *Monte Carlo Simulation in Statistical Physics* (Springer, Berlin/Heidelberg, 1988).
- [95] H.-P. Deutsch. *Optimized analysis of the critical behavior in polymer mixtures from Monte Carlo simulations*. J. Stat. Phys. **67**: 1039–1082 (1992).
- [96] H. Weber, W. Paul, and K. Binder. *Monte Carlo simulation of a lyotropic first-order isotropic-nematic phase transition in a lattice polymer model*. Phys. Rev. E **59**: 2168–2174 (1999).
- [97] M. S. S. Challa, D. P. Landau, and K. Binder. *Finite-size effects at temperature-driven first-order transitions*. Phys. Rev. B **34**: 1841–1852 (1986).
- [98] K. Merkel, A. Kocot, J. K. Vij, R. Korlacki, G. H. Mehl, and T. Meyer. *Thermotropic biaxial nematic phase in liquid crystalline organo-siloxane tetrapodes*. Phys. Rev. Lett. **93**: 237 801 (2004).
- [99] Z. Zhang, O. G. Mouritsen, and M. J. Zuckermann. *Weak first-order orientational transition in the Lebwohl-Lasher model for liquid crystals*. Phys. Rev. Lett. **69**: 2803–2806 (1992).
- [100] R. Berardi, A. P. J. Emerson, and C. Zannoni. *Monte Carlo investigations of a Gay-Berne liquid crystal*. J. Chem. Soc., Faraday Trans. **89**: 4069–4078 (1993).
- [101] V. K. Gupta and N. L. Abbott. *Design of surfaces for patterned alignment of liquid crystals on planar and curved substrates*. Science **276**: 1533–1536 (1997).
- [102] B.-W. Lee and N. A. Clark. *Alignment of liquid crystals with patterned isotropic surfaces*. Science **291**: 2576–2580 (2001).



## Danksagung

Mein ganz besonderer Dank gilt Prof. Dr. Martin Schoen der mir die Möglichkeit gegeben hat in seinem Arbeitskreis zu promovieren. Die Anfertigung dieser Arbeit wäre ohne die hervorragende Betreuung während der gesamten Zeit undenkbar gewesen. Ich möchte mich herzlich bei dem zweiten Berichtler Prof. Dr. Keith Gubbins für die Anfertigung des Gutachtens und die drei wundervollen Monate, die ich in seiner Arbeitsgruppe verbringen durfte, bedanken. Weiterhin gilt mein Dank dem Vorsitzenden des Prüfungsausschuss Prof. Dr. Martin Oestreich.

Dr. Marco Mazza möchte ich danken für das Korrekturlesen von Teilen des Manuskripts, seine wertvollen Anmerkungen und die fruchtbare Kollaboration. Ich danke den weiteren Mitgliedern der AG Schoen, Jörg Silbermann, Gerrit Günther, Timo Poppmann, Michael Melle, Stefano Giura, Vinothkumar Mohanakrishnan, Tillmann Stieger, Sergej Schlotthauer, Sascha Klawohn, Roman Schmack und Sophia Siefke sowie Heidi Grauel und Nadine Rechenberg für die herzliche Atmosphäre.